

INSTITUTO POLITÉCNICO NACIONAL

**CENTRO DE INVESTIGACIÓN EN CIENCIA APLICADA
Y TECNOLOGÍA AVANZADA**

UNIDAD QUERÉTARO

**Development of a Coaxial Dielectric Barrier Discharge Plasma
Fluidized-Bed Reactor (COAX-DBD PFBR) for surface
modification of granular material with low pressure plasma**

**TESIS PARA OBTENER EL GRADO DE
MAESTRÍA EN TECNOLOGÍA AVANZADA**

PRESENTA

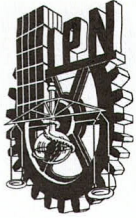
Ing. Enrique Augusto García Guerrero

DIRECTORES DE TESIS:

Dr. Martín de Jesús Nieto Pérez, Dr. Jorge Adalberto Huerta Ruelas



Santiago de Querétaro, Qro. a 5 de mayo del 2022.



INSTITUTO POLITÉCNICO NACIONAL

SECRETARIA DE INVESTIGACIÓN Y POSGRADO

ACTA DE REGISTRO DE TEMA DE TESIS Y DESIGNACIÓN DE DIRECTOR DE TESIS

Ciudad de México, a 16 de mayo del 2022

El Colegio de Profesores de Posgrado de **CICATA Unidad Querétaro** en su Sesión Ordinaria No. 220513 celebrada el día 13 del mes mayo del 2022, conoció la solicitud presentada por el alumno:

Apellido Paterno:	García	Apellido Materno:	Guerrero	Nombre (s):	Enrique Augusto
-------------------	--------	-------------------	----------	-------------	-----------------

Número de registro:

A	1	6	0	9	8	6
---	---	---	---	---	---	---

del Programa Académico de Posgrado:

Maestría en Tecnología Avanzada

Referente al registro de su tema de tesis; acordando lo siguiente:

1.- Se designa al aspirante el tema de tesis titulado:

Development of a Coaxial Dielectric Barrier Discharge Plasma Fluidized Bed Reactor (COAX-DBD PFBR) for surface modification of granular material with low pressure plasma

Objetivo general del trabajo de tesis:

Construcción y puesta a punto de un prototipo escala laboratorio para el tratamiento superficial de material granular con plasma atmosférico.

2.- Se designa como Directores de Tesis a los profesores:

Director:

Dr. Martín de Jesús Nieto Pérez

 2° Director:

Dr. Jorge Adalberto Huerta Ruelas

No aplica:

3.- El Trabajo de investigación base para el desarrollo de la tesis será elaborado por el alumno en:

CICATA IPN-Unidad Queretaro

que cuenta con los recursos e infraestructura necesarios.

4.- El interesado deberá asistir a los seminarios desarrollados en el área de adscripción del trabajo desde la fecha en que se suscribe la presente, hasta la aprobación de la versión completa de la tesis por parte de la Comisión Revisora correspondiente.

Director de Tesis

Dr. Martín de Jesús Nieto Pérez

Aspirante

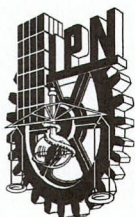
Ing. Enrique Augusto García Guerrero

2° Director de Tesis

Dr. Jorge Adalberto Huerta Ruelas

Presidente del Colegio

Dr. Juan Bautista Hurtado Ramos



INSTITUTO POLITÉCNICO NACIONAL

SECRETARÍA DE INVESTIGACIÓN Y POSGRADO

ACTA DE REVISIÓN DE TESIS

En la Ciudad de siendo las horas del día del mes de del se reunieron los miembros de la Comisión Revisora de la Tesis, designada por el Colegio de Profesores de Posgrado de: para examinar la tesis titulada:

del (la) alumno (a):

Apellido Paterno:	García	Apellido Materno:	Guerrero	Nombre (s):	Enrique Augusto
-------------------	--------	-------------------	----------	-------------	-----------------

Número de registro:

Aspirante del Programa Académico de Posgrado:

Una vez que se realizó un análisis de similitud de texto, utilizando el software antiplagio, se encontró que el trabajo de tesis tiene 15% (25%) de similitud. **Se adjunta reporte de software utilizado.**

Después que esta Comisión revisó exhaustivamente el contenido, estructura, intención y ubicación de los textos de la tesis identificados como coincidentes con otros documentos, concluyó que en el presente trabajo SI NO **SE CONSTITUYE UN POSIBLE PLAGIO.**

JUSTIFICACIÓN DE LA CONCLUSIÓN: Debido a que el estudiante escribió un artículo JCR y la tesis también fue escrita en Ingles, el reporte genera 10% adicional en el reporte incrementándose de 15% a 25% oid:14652:147070186

Finalmente y posterior a la lectura, revisión individual, así como el análisis e intercambio de opiniones, los miembros de la Comisión manifestaron **APROBAR** **SUSPENDER** **NO APROBAR** la tesis por **UNANIMIDAD** o **MAYORÍA** en virtud de los motivos siguientes:

COMISIÓN REVISORA DE TESIS

Dr. Martín de Jesús Nieto Pérez

Dr. Jorge Adalberto Huerta Ruelas

Dra. Ma. Guadalupe del Carmen Méndez Montealvo

Dr. Antonio Hernández Zavala

Dr. José Dolores Oscar Barceinas Sánchez

Dr. Juan Bautista Hurtado Ramos
PRESIDENTE DEL COLEGIO DE PROFESORES
SECRETARÍA DE INVESTIGACIÓN Y POSGRADO
UNIDAD QUERETARO
DIRECCIÓN



INSTITUTO POLITÉCNICO NACIONAL

SECRETARÍA DE INVESTIGACIÓN Y POSGRADO

CARTA DE AUTORIZACIÓN DE USO DE OBRA PARA DIFUSIÓN

En la Ciudad de México el día 5 del mes de **mayo** del año **2022**, el (la) que suscribe Ing. **Enrique Augusto García Guerrero**, alumno(a) del **Centro de Investigación en Ciencia Aplicada y Tecnología Avanzada plantel Querétaro**, con número de registro **A160986**, adscrito(a) Al programa de **Maestría en Tecnología Avanzada**, manifiesta que es autor(a) intelectual del presente trabajo de tesis bajo la dirección del **Dr. Martín de Jesús Nieto Pérez** y del **Dr. Jorge Adalberto Huerta Ruelas**, y cede los derechos del trabajo titulado **Development of a Coaxial Dielectric Barrier Discharge Plasma Fluidized Bed Reactor (COAX-DBD PFBR) for Surface modification of powders with low pressure plasma**, al Instituto Politécnico Nacional, para su difusión con fines académicos y de investigación.

Los usuarios de la información no deben reproducir el contenido textual, gráficas o datos del trabajo sin el permiso expresado del autor y/o director(es). Este puede ser obtenido escribiendo a las siguiente(s) dirección(es) de correo eaggro@gmail.com, m.nieto@ieee.org, jhuertar@ipn.mx. Si el permiso se otorga, al usuario deberá dar agradecimiento correspondiente y citar la fuente de este.



Ing. Enrique Augusto García Guerrero

DEDICATION

Dedicated with love to my family:

My loving wife Mariana Vilches Linares, my mother María Soledad Guerrero Sánchez, my grandmother Berta Sánchez Domínguez, my brother Jorge Arturo García Guerrero, my nephews Arturo and Andrés and my uncle Dr. Enrique Guerrero Sánchez, for their unconditional love and support during all these years. In loving memory of my grandfather Dr. Arturo Guerrero Ortiz and my niece Ana.

ACKNOWLEDGEMENTS

I will mention everyone that deserves acknowledgement for helping me in the completion of this work.

I want to thank the National Council for Science and Technology, Mexico (CONACYT) for the support given during my graduate work at IPN-CICATA Querétaro and the National Polytechnic Institute, México (IPN) and the IPN-CICATA Querétaro, for the support given for my research project.

I want to thank you both, Drs. Martín de Jesús Nieto Pérez and Jorge Adalberto Huerta Ruelas, for accepting my research proposal and sharing their vast knowledge with me and guide me towards the completion of my research and graduate work.

Thanks to my friends, whose invaluable and unconditional support allowed me to accomplish this goal in my career: D.A. Coronado Balderas, R. Malagón Mata, K. Axel Castillo, G. Cavazos Enríquez, E. Morales Rivera, J. A. Guerrero Pérez, A. Corro, F. Mosterín Cantón, D. Rivas Guerrero, K. A. Ortega, R. Noguera, D. Jaramillo Santoscoy, N. Hernández, R. Noriega, R. Mosqueda Morales, J. C. Cueto Hernández, E. Rebolledo Lozano, J. M. Hernández Nieto and J.C. Manzano.

I want to thank you both, Drs. Adrián Luis García García and Iván Domínguez López for sharing with me your knowledge and skills during my research stay in the IPN-CICATA Querétaro. I want to thank my former professors during my High-school and University studies. Who shared their time, skills, and knowledge with me. Edgardo López Mañón (ITESM-Qro), Drs: Alfonso Lastras Martínez, Andrei Gortvatchev, Michourny Viatcheslav, Manuel Flores Camacho, Luis Felipe Lastras Martínez, Raúl Balderas Navarro and Gustavo Ramírez Flores (IICO-UASLP). And also I want to thank the ITESM Campus Querétaro, the UASLP, the Science Faculty of the UASLP (FC-UASLP) and the research center IICO-UASLP for all the knowledge and experience I acquired during my high school and University studies.

RESUMEN

El presente proyecto de investigación consiste en la construcción y puesta a punto de un reactor de plasma por lecho fluidizado para el tratamiento superficial de material granular con plasma atmosférico. La puesta a punto del reactor se basa en: la construcción de una columna de fluidización y la obtención del estado de fluidización en los polvos y el efecto que tuvo el tratamiento en los polvos con el plasma generado. El tratamiento se estudió realizando las siguientes técnicas: granulometría, reometría, calorimetría y un diagnóstico preliminar en la dispersión de los polvos mediante señales de luz esparcida del reactor, con y sin la presencia de una descarga dieléctrica coaxial para denotar el comportamiento del material granular al momento de fluidizar. Para propósitos de este trabajo, se utilizaron dos tipos de gránulos; uno orgánico, almidón de papa y otro inorgánico, dióxido de Titanio (TiO_2). Para este trabajo, el material granular fue tratado con plasma de argón y de acuerdo al arreglo utilizado se pudieron agregar monómeros para poder modificar la superficie, como por ejemplo, se utilizaron: hexametildisiloxano, metanol, isopropanol y acetona.

El arreglo de fluidización o columna de fluidización, consiste en un cilindro de cristal de cuarzo, adaptado con una entrada para gas en su base inferior y en el interior, los distribuidores para la obtención del estado de fluidización. En la parte superior se ubica el redistribuidor de partículas al sistema y el electrodo positivo para la generación del plasma. La generación de plasma es por la técnica de Descarga de Barrera Dieléctrica (DBD) en configuración coaxial. El cual consiste, en una fuente de alimentación eléctrica con las siguientes características: cuenta con un rango de radio frecuencia para manejar una frecuencia variable entre 10 y 100kHz, produce una onda sinusoidal de amplitud entre 0 y 10KVpp con una potencia de hasta 3KW, capacidad de corriente de entrada máxima de hasta 15.

El sistema optoelectrónico está compuesto de 16 LEDs fungiendo como emisores, ensamblados sobre una placa en línea recta y en serie. Frente a la placa emisora se encuentra una placa con 16 fotodiodos, fungiendo como receptor y de igual manera ensamblados en línea recta sobre una placa y en serie. Son 2 placas paralelas a una distancia de 7cm; quedando en pares 1 LED y enfrente 1 fotodiodo (receptor-emisor). La placa receptora estará conectada a una tarjeta NI My Rio de National Instruments y enviando los datos a un instrumento virtual de Labview a la computadora para la obtención y análisis de datos.

Como parte del desarrollo de este trabajo de investigación, se publicó un artículo de investigación en la revista internacional: IEEE-Transactions on Plasma Sciences, Special Issue LAWPP 2017, mismo que se agrega en la sección de anexos (anexo 6) e incluida en las referencias bibliográficas y parte de los resultados presentados en el mismo fueron utilizados en este trabajo.

ABSTRACT

The research Project presented in this work, consists of the construction and assessment of a fluidized-bed plasma reactor for the atmospheric plasma surface treatment of granular material, with a coaxial dielectric barrier discharge configuration. Referred in this work as: Coaxial Dielectric Barrier Discharge Plasma Fluidized-Bed Reactor, (COAX-DBD PFBR). The assessment of the reactor is based on the construction of a fluidization column and achieve the fluidization state of the powders and the effect that the treatment had over the granules with the interaction with the generated plasma. This was studied submitting the treated granules to the following techniques: granulometry, rheometry, calorimetry and a preliminary test, for the analysis of the dispersion of the powders inside the reactor by light scattering signals in the presence of a dielectric discharge and without it. For purposes of this work, two types of powders were used: an organic type, potato starch, and an inorganic type, Titanium Dioxide (TiO_2). The granular material was treated with Argon (Ar) Plasma and because of the arrangement used, four different monomers were added, these were: hexamethyldisiloxane, methyl, isopropyl and acetone.

The fluidizing arrangement consists of a cylinder of quartz glass, at its lower base is adapted for the gas inlet and the distributors for the fluidization process. At the upper section of the cylinder, the redistributor particle system and the electrode to induce voltage for plasma generation is located. The plasma generation technique is the Dielectric Barrier Discharge (DBD) in a coaxial configuration.

The system of plasma generation is a power supply with the following characteristics: it has a radio frequency range to handle a variable frequency between 10 and 100 kHz, produces a sine wave amplitude between 0 and 10KVpp with a power up 3KW, current capacity maximum input up to 15. This source can provide a high voltage and high frequency.

The optoelectronic prototype consists of 16 LEDs serving as emitters, assembled on a plate in a straight line and in series. Facing the emitter plate is another one with 16 photodiodes, serving as receivers and similarly assembled straight onto a plate and serially. Both plates are parallel at a distance of 7cm; 1 LED running in pairs and opposite one photodiode (receiver - transmitter). The receiver plate is connected to a MyRio-NI National Instruments and sending the data to a virtual instrument of Labview to the computer for data collection and analysis.

As part of the development and progress of this research work, a research paper was published in the IEEE-Transactions on Plasma Sciences, Special Issue LAWPP 2017, which is presented in the appendix 6, included in the references of this work. And also, part of the results presented in the research paper were used in this work.

Palabras clave - Keywords

Fluidización, luz esparcida, tecnología de plasmas, tecnología de polvos

Fluidization, light scattering, plasma technology, powder technology

TABLE OF CONTENT

DEDICATION	2
ACKNOWLEDGEMENTS	3
RESUMEN	4
ABSTRACT	5
PALABRAS CLAVE - KEYWORDS.....	6
TABLE OF CONTENT	7
LIST OF FIGURES.....	10
LIST OF TABLES.....	13
NOMENCLATURE	14
LIST OF APPENDICES	16
THESIS STRUCTURE	17
CHAPTER I.....	18
PROBLEM STATEMENT AND MOTIVATION	18
OBJECTIVE	20
1.1.1 <i>Specific objectives:</i>	20
CHAPTER II STATE OF THE ART	21
PARTICLE CHARACTERISTICS	21
2.1.1 <i>Particle Size</i>	22
2.1.2 <i>Diameter</i>	23
2.1.3 <i>Shape</i>	25
2.1.4 <i>Particle Density</i>	25
2.1.5 <i>Bulk Density</i>	26
2.1.6 <i>Particle Classification</i>	27
BRIEF OVERVIEW OF STARCHES AND TiO ₂	29
2.1.7 <i>Starches</i>	30
2.1.7.1 Characteristics of starch granules: morphology, size, composition and crystallinity	32

2.1.7.2	Potato Starch	37
2.1.8	<i>Titanium Dioxide</i>	38
PLASMAS:	38
2.1.9	<i>Plasma theory</i>	42
2.1.10	<i>Methods of Plasma Generation</i>	44
2.1.10.1	Electric Breakdown.....	47
2.1.10.2	Radio-Frequency Discharge	48
2.1.11	<i>Plasma Parameters</i>	50
2.1.12	<i>Atmospheric plasmas</i>	54
2.1.12.1	The Dielectric Barrier Discharge.....	55
FLUIDIZATION	56
2.1.13	<i>Fluidization Theory</i>	57
2.1.14	<i>Fluidization columns and reactors</i>	60
CHAPTER III CONCEPTUAL FRAMEWORK	64
3.1.1	<i>Fluidization of cohesive particles</i>	64
3.1.2	<i>Atmospheric plasma for surface modification</i>	65
3.1.3	<i>Fluidized-beds for surface modification of granular material with atmospheric plasma</i>	66
3.1.3.1	Surface Modification of Starches	67
3.1.3.2	Modified starches in industry.....	68
3.1.3.3	Surface Modification of TiO ₂	70
CHAPTER IV MATERIALS & METHODS	71
DESIGN AND CONSTRUCTION OF THE REACTOR	71
4.1.1	<i>Testing Bench</i>	74
MATERIALS	77
4.1.2	<i>Plasma Generation System Components</i>	77
4.1.2.1	Inner Electrode.....	77
4.1.2.2	Inner electrode internal holder	78
4.1.2.3	Top Lid	80
4.1.2.4	Dielectric Surface	81
4.1.2.5	External Electrode	82
4.1.2.6	Radio Frequency Power Supply System	82
4.1.3	<i>Fluidization System Components</i>	85
4.1.3.1	Rotameters	86

4.1.3.2	Input gas component.....	87
4.1.3.3	Plenum	87
4.1.3.4	Distributor: Hollow Hexagonal-prisms.....	88
4.1.3.5	Powder Container Component.....	89
	SELECTED POWDERS.....	89
	PLASMA SURFACE MODIFICATION WITH THE COAX-DBD PFBR.....	90
	PRELIMINARY OPTICAL SYSTEM	94
	PARTICLE CHARACTERIZATION TECHNIQUES.....	97
4.1.4	<i>Granulometry</i>	97
4.1.5	<i>Calorimetry</i>	98
4.1.6	<i>Rheometry</i>	98
	CHAPTER V RESULTS & DISCUSSION.....	100
	FINAL REACTOR DESIGN AND PROCESS DESCRIPTION.....	100
	FLUIDIZATION PROPERTIES OF THE POWDERS	101
	PRELIMINARY RESULTS OF THE LIGHT SCATTERING SIGNALS OF THE FLUIDIZATION PROCESS FOR TiO ₂	103
	PRELIMINARY RESULTS FOR THE SEDIMENTATION PROPERTIES OF THE MODIFIED TiO ₂	108
	GRANULOMETRY RESULTS OF THE POWDERS	109
	RHEOMETRY AND CALORIMETRY RESULTS OF THE POWDERS	110
	CONCLUSION	112
	FUTURE WORK	113
	REFERENCES.....	116
	APPENDICES.....	122
	APPENDIX 1 : SURFACE MODIFICATION OPERATION DIAGRAM	122
	APPENDIX 2: COMPONENTS OF THE REACTOR.....	123
	APPENDIX 3: ASSEMBLE OF THE REACTOR MANUAL	125
	APPENDIX 4: CLEANING MANUAL.....	128
	APPENDIX 5: OPERATION MANUAL	129
	APPENDIX 6: RESEARCH PRODUCTS.....	130

LIST OF FIGURES

Figure 1. Common example of the four states of matter	39
Figure 2. Plasma applications at different currents and gas pressures [8].	41
Figure 3. Essential components for a generic plasma reactor, adapted from [39]......	46
Figure 4. Simple schematic for the simplest configuration to produce an electrical discharge through a gas [32].	48
Figure 5. Schematic diagram of power supply components needed for plasma sources that require (a) AC line voltage only; (b) DC electrical power; and (c) RF power. Adapted from [38].	54
Figure 6. Schematic for the Dielectric Barrier Discharge, [40].	55
Figure 7. In a two-phase fluidization, gas moves through the particle bed, (a), and as an emulsion or dense phase, (b). The picture was adapted from [11].	56
Figure 8. Representation of the types of fluidization as the gas velocity through the bed increases. Adapted from [11].	58
Figure 9. Fluidization behavior of particles, adapted from [11].	58
Figure 10. Fluidization column, (a) Fluid bed sections and (b) Freeboard and bed height schematic. Adapted from [45].	61
Figure 11. Powder flowability considerations for achieving the fluidized state. The flow movility of the powder (a), and the angle of the connical hopper for a proper mass flow (b). Picture adapted from [9].	63
Figure 12. The Fluidized-bed Plasma Reactor built in the laboratory; in (a) the components are presented, in (b) a diagram for the assembled reactor.	72
Figure 13. Photographs of the milling machine (a) and lathe machine (b), been used while the fabrication of the fluidization column in the Prototype Workshop of the Research Center.	72
Figure 14. Complete diagram of the assembly and disassembly of the reactor	73
Figure 15. The standard Aluminum Parker-profiles of 40x40mm (a), the measures of the profile (b) and (c).	74
Figure 16. Photographs of the constructed testing bench (a), and the complete assemble of the COAX-FBPR and the Jet-type Coaxial reactor to the testing bench.	75
Figure 17. The test bench diagram.	76
Figure 18. Components for the COAX-DBD FBPR on the test bench.	76
Figure 19. Diagram of the constructed fluidization column and its components.....	77
Figure 20. Inner electrode used for the reactor.....	78
Figure 21. Measures of the inner electrode.....	78
Figure 22. The inner holder design, both (a) and (b) were designed and built.	79

Figure 23. Measures of the inner electrode holder, first version Figure 20a.	79
Figure 24. Measures of the inner electrode holder, second version Figure 20b.	79
Figure 25. Photograph of the top lid component of the reactor.	80
Figure 26. Design of the lower component of the top lid.....	80
Figure 27. Assembly of the upper components of the reactor.....	81
Figure 28. Photograph of the cylindrical Quartz crystal glass used as the dielectric surface of the reactor.	81
Figure 29. Photograph of the external electrode of the reactor, a stainless-steel wired mesh.	82
Figure 30. The Radio Frequency used for this project. (a) The source with the labels numbered 1 – 6 presenting the components. (b) Block diagram of operation.	83
Figure 31. Electric circuit diagram of the power supply for the COAX-DBD FBPR, adapted from [41].	84
Figure 32. Fluidization system components, (a) powder container 1), distributor 2), 3) plenum, gas input 4), mechanical vibration 5), rotameters 6). (b) Conexion diagram of the fluidization and plasma generation systems, 7) gas container, 8) , 9) RF-source.....	85
Figure 33. Photographs of the rotameters used for this project. a) 2-20 SCFH, B) 0-10 SCFH.....	86
Figure 34. Diagram and measures of the component that joints the upper part of the reactor with the crystal quartz cylinder.	87
Figure 35. Photograph of the plenum of the reactor.....	88
Figure 36. Design and measures of the Component that holds the plenum (a) and the fist distributor	88
Figure 37. Design and measures of the powder container component (a), and the diagram explaining the operation and advantages of the component (b).	89
Figure 38. Operation and diagram of conectors of the COAX-DBD Plasma reatctor.	91
Figure 39. Diagram of the coaxial dielectric barrier discharge configuration.	92
Figure 40. Light scattering for particle charaterization prototype. (a) Design, showing 16 photodetectors and 16 emmisors. (b) Distance between the reactor and the plates. (c) The prototype operating in the presence of a discharge.	95
Figure 41. Arrangement used in the research work, for the light scattering prototype.	96
Figure 42. (a) Diagram of the measures of the space between the radius of the Quartz glass cylinder (dielectric surface) and the inner electrode. (b) The arrangement of the emissor and detector plates are presented.	96
Figure 43. Components of the constructed COAX-DBD FBPR	100

Figure 44. Components diagram of the preliminary prototype for monitoring light scattering signals from the COAX-DBD PFBR. The longitude measurements of the sensors arrays are presented in (a), the distance between the plates and the COAX-DBD PFBR is presented in (b). 104

Figure 45. Average and Standard Deviation values for the Groups 2 through 4. Reference: (REF_0) signal, with flux without powder and plasma Signal, Powder with flux without plasma (PFsP) Reference signal (REF_00), flux with powder and plasma Signal, powder with flux and plasma (PcP) 105

Figure 46. Graph for the behavior of the emissor-receptor plate for sensor 12 for the signal processing of the light scattering during the test. For this figure: Reference: (REF_0) signal, with flux without powder and plasma Signal, Powder with flux without plasma (PFsP) Reference signal (REF_00), flux with powder and plasma Signal, powder with flux and plasma (PcP) 106

Figure 47. Graph for the preliminary results for the light scattering signal acquisition from the granules during the operation of the COAXDBD PFBR. For this figure: Reference: (REF_0) signal, with flux without powder and plasma Signal, Powder with flux without plasma (PFsP) Reference signal (REF_00), flux with powder and plasma Signal, powder with flux and plasma (PcP) 107

Figure 48. Sedimentation test for the treated TiO₂. Untreated TiO₂ in water, left, and treated TiO₂ in water, right. 108

Figure 49. Granulometry results for the Potato Starch (a) , and the Titanium Dioxide (b)..... 109

Figure 50. Rheometry results for the potato starch..... 110

Figure 51: Alternative lids for the DBD reactor. The Superior (a) and inferior (b) lids. The material for these parts can be also nylomaq or nylamid, with ½ ” wholes for input and output gases. These designs were taken from [20]. 114

Figure 52. Diagram of the optical prototype with two photodetectors plates..... 115

Figure 53. The design model of the joint between the optical prototype and the COAX-DBD Fluidized Plasma reactor 115

Figure 54. Schematic of the reactor, armed and with all the components labeled..... 125

Figure 55. Schematic of the order of the lower components when assembled..... 126

Figure 56. Schematic of the order of the upper components when assembled. 126

Figure 57. Schematic of the order of the upper components when disassembled. 127

Figure 58. Schematic of the order of the lower components when disassembled..... 127

LIST OF TABLES

Table 1. List of definitions of equivalent sphere diameters [2].	24
Table 2. List of Definitions of equivalent circle diameters [2].	24
Table 3. Geldart’s classification powders according to the fluidization behavior of powders	29
Table 5. List of major starch sources with their respectively percentage of starch content [22].	31
Table 6. Temperature and pressure ranges of hot and cold plasmas [8].	40
Table 8. Description of the four most elementary processes due to collisions between electron and the atom or ion inside the plasma [32], [33], [36].....	44
Table 9. List of different ways for plasma generation.....	45
Table 10. Plenum measure requiremnts according to the gas entry configuration [47].....	61
Table 11. RF Source used in this work, for its operation.....	84
Table 12. Operation values used for the treatments and the solvent species used in each powder.....	94
Table 13. Physical properties of the powders.....	102
Table 14. Fluidization parameters during the experiments	103

NOMENCLATURE

A	Area	Q	Charge
A	Ampere	V	Volume
°C	Celsius Degree	ω	Angular frequency
D	Diameter	m	Meter
gr	Grams	P,p	Pressure
I	Current	T	Temperature
J	Joule	V	Volts
K	Kelvin degrees	W	Watts
Ω	Ohm	μ	micro
Ev	Electron Volt	e^-	Electron
M	Mol	η	Efficiency
η_e	Electronic density	K	Kilo
Γ_e	Electron Flux	Hz	Hertz
Γ_i	Ion Flux	C	Capacitance
\bar{E}	Electric field	f	Frecuency
C	Coulomb	μ_e	Electronic Movility

S_i	Electron source	μ_i	Ion movility
N	Density	s	Second
min	Minute	F	Farad
k_B	Boltzmann Constant	ϵ_0	Vacuum permittivity

LIST OF APPENDICES

APPENDIX 1 : SURFACE MODIFICATION OPERATION DIAGRAM	122
APPENDIX 2: COMPONENTS OF THE REACTOR	123
APPENDIX 3: ASSEMBLE OF THE REACTOR MANUAL	125
APPENDIX 4: CLEANING MANUAL.....	128
APPENDIX 5: OPERATION MANUAL	129
APPENDIX 6: RESEARCH PRODUCTS.....	130

THESIS STRUCTURE

The organization of this work is in consideration for the reader, the first chapter is an introduction into the subject developed through the thesis. This chapter includes an abstract, the problem statement and the objectives. This chapter helps the reader to understand the content of the work.

On the second chapter, the state of the art is presented, where the main topics of the work are discussed, these are: particle characteristics and their classification, plasma theory and surface modification with atmospheric plasma, fluidization theory, and particle fluidization.

After the main topics were introduced to the reader, the specific concepts for each topic that were used for the developed research work are presented on the third chapter, the conceptual framework. These concepts are the following, for the topic of the fluidization theory: particle types A & C according to the Geldart Scale and fluidization of cohesive powders. For the topic of plasma theory, DBD reactors with coaxial geometry and surface modification of granular material with atmospheric plasmas.

On the fourth chapter, the methodology is presented. Where the Coaxial-DBD Fluidized-Bed Reactor, the plasma generation system, fluidization system, the preliminary optical system and the two powders are described. Also, the three particle characterization techniques used, such as: granulometry, calorimetry and rheometry.

On the fifth chapter, the results are presented and discussed on the sixth chapter.

The conclusions of this thesis are presented on the seventh chapter. Which includes the fluidization results, reactor design, granular material modification and the future work for this research project.

The last part of this work, the references and appendices are presented. Where the reactor design, research products, and the operation, cleaning and assemble manuals can be find. This thesis was written for the reader, so he could rely on it as an aid for his research project.

CHAPTER I

Problem Statement and Motivation

The present thesis relies on the advantages and increasing interest for the surface modification of powders (organic and inorganic) with plasmas, especially with atmospheric plasmas (for this work), and the need of the gas-solid fluidized bed reactors for this method. Both technologies have applications in industry and research.

The actual need the Research Center has, and especially in the Laboratory of Industrial Applications of Plasma, for an instrument for plasma surface modification of granular material. And taking in consideration, the industrial growth the city of Querétaro (Querétaro, México) is having; it is an opportunity for this Research Center to offer a service to the industry the city has and for the different industry fields that are coming. With this instrument, the Laboratory will have three different types of reactors in a Lab-scale for research purposes and industry diagnostic services of surface modification with atmospheric plasma.

The importance of having this type of reactor in the laboratory rely on the actual needs in several areas of industry, for plasma treated powders, mainly in food, pharmacological and materials industry. In which the plasma treatment is based on a dielectric barrier discharge (DBD) reactor; the proposed configuration of the reactor combines the gas-solid fluidized bed reactor features with a coaxial-DBD configuration. The main advantage of this type of reactor is the good solid mixing. This type of reactor is called: Coaxial-DBD Fluidized-Bed Reactor (Coax-DBD FBR) and is a relatively new technology for the plasma surface modification of powders. For purposes of this work, the interested field is in natural polymers surface modification by atmospheric plasma, covering the actual necessity of substituting the artificial polymers for similar materials, which is in high demand. Natural polymers, such as starches, are a solution because of their abundance in nature and because of the obtained products will be biodegradable.

For this work, two powders, one type A (of the Geldart's Scale), organic (potato starch) and one type C inorganic (titanium dioxide) were subjected to plasma treatments using different solvents (Table 10), and the behavior of properties closely associated to the surface modification was tested. For the starch, gelatinization and rheological properties were assessed, while for the titanium dioxide the behavior of the powder in water suspension was evaluated. In both cases, the modification of powder surface due to plasma exposure was evident given the results of the experimental tests performed on the powders after plasma treatment.

Objective

- Construction and assessment of a laboratory scale prototype for surface treatment with atmospheric plasma of granular material.

1.1.1 Specific objectives:

- 1) Designed and construction of a fluidized-bed reactor and with a coaxial-DBD configuration for the plasma generation.
- 2) Assessment of the method for the surface treatment of granular material; fluidization condition and plasma generation condition.
- 3) Determination of the surface treatment of the powders, by submitting the treated granules to a granulometry test and the organic granules into a calorimetry and rheometry tests. The inorganic granules were submitted into a preliminary test of sedimentation in water.

CHAPTER II STATE OF THE ART

Particle characteristics

In nature, matter is divided into solid, liquid, gas and plasma states. Powder is defined as a finely divided solid. Powders present some characteristics so distinctive that make them practically different, with other state of matter. Intrinsically, molecules forming a solid piece are joined by chemical bonds and interactions stronger than those forming liquid or gases. Externally, there are no interactions of the chemical bond type keeping together small particles forming a powder batch. It has been suggested that the individual entities within masses of particulate solids are so kept only by geometrical accommodation. Some of the distinctive characteristics of powders, that have made them subject of research efforts to understand their behavior are powders are not solids but may deform under compression. Powders are not liquids, but they may flow under certain circumstances. Powders are not gases, but they may be compressed up to a degree [1]–[3].

It has been observed for quite a while that dry powder possesses many properties common to fluids, such as exerting pressure on container vessels and flowing through channels or orifices. There are, nonetheless, important differences such as a powder does not exert uniform pressure on all directions in confinement. The exerted pressure is minimal at the perpendicular direction of the applied pressure. An applied shear force on the surface of a mass of powder is transmitted through all the static mass unless a fracture occurs. The density of a mass of powder varies depending on its degree of packaging; it increases if the powder is compacted by vibration, shaking, taping, and so on [1]–[3].

Powder or particle technology, is the branch of engineering that studies particulate material, either in dry form or suspended within some fluid. The interest of this field are numerous and involves operations of characterization, storage, conveying, mixing, fluidization, classification, agglomeration, along with others, of powders and particulate systems [1]–[4]. This branch of engineering has been developed alongside other related branches and the discoveries brought by the study of particulate systems focusing on the particle

technology principles has resulted in benefits for different industrial processes, including manufacturing of chemicals, pharmaceuticals, food, ceramics, among others [1]–[7].

A material is considered a powder if it is composed of dry, discrete particles with a maximum dimension of less than 1000 μm ; while a particle is defined as any relatively small subdivision of matter, ranging in diameter from a few angstroms to a few millimeters. In any case both groups of individual entities represent bulk materials. Which are of relevance in many industrial processes. Also, efficient, and reliable methods for characterizing them are needed in research, academia, and industry. The properties of powder and particulate materials have been divided into primary and secondary. The first ones, are those inherent to the intimate composition of the material and the second ones are those relevant when considering the systems as assemblies of discrete particles whose internal surfaces interact with a gas, generally air [1]–[3], [8], [9].

Primary particle properties such as particle shape and particle density, together with the primary properties of a fluid such as viscosity and density, and with the concentration and state of dispersion, govern the secondary properties such as settling velocity of particles, rehydration rate of powders, resistance of filter cakes, and so on. It is simpler, and more reliable, to measure the secondary properties directly without reference to the primary ones. Direct measurement of secondary properties can be done in practice, but the aim is to predict them from the primary ones, as when determining pipe resistance to flow from known relationships, feeding in data from primary properties of a given liquid (viscosity and density), as well as properties of a pipeline (roughness) [1]–[3].

2.1.1 Particle Size

The term size of a powder or particulate material is relative; it is often used to classify, categorize, or characterize a powder. The common convention considers that for a particulate material to be considered powder, its approximate median size (50% of the material is smaller than the median size and 50% is larger) should be less than 1 mm and it is also common practice to talk about fine and coarse powders. Also, by convention,

particle sizes may be expressed in different units depending on the size range involved. Coarse particles may be measured in centimeters or millimeters, fine particles in terms of screen size, and very fine particles in micrometers or nanometers. However, particle size may be expressed in meters when doing engineering calculations, or in micrometers by the small range normally covered or when doing graphs [1]–[3].

2.1.2 Diameter

The particles forming a powder will rarely have a spherical shape. Many industrial powders are of mineral (metallic or nonmetallic) origin and have been derived from hard materials by any sort of size reduction process. The particles may be compact, with length, breadth, and thickness nearly equal, but, sometimes, they may be plate-like or needle-like. As particles get smaller, and by the influence of attrition due to handling, their edges may become smoother and, thus, they can be spherical. The term diameter is, often used to refer to the characteristic linear dimension. All these geometrical features of an important number of industrial powders, are related to the intimate structure of their forming elements, whose arrangements are normally symmetrical with definite shapes such as cubes, octahedrons, and so on. Therefore, expressing a single particle size is not simple when its shape is irregular. This case would be quite frequent in many applications, mostly when dealing with powders of truly organic origin. Irregular particles can be described by several sizes. The group of definitions, for the equivalent sphere diameters in granules are presented in Table 1 and Table 2; which present the, equivalent circle diameters, respectively [1]–[3].

Symbol	Name	Equivalent Property of a sphere
--------	------	---------------------------------

x_v	Volume Diameter	Volume
x_s	Surface Diameter	Surface
x_{sv}	Surface Volume Diameter	Surface to volume ratio
x_d	Drag Diameter	Resistance to motion in the same fluid at the same velocity
x_f	Free Falling Diameter	Free-falling speed in the same liquid at the same particle density

Table 1. List of definitions of equivalent sphere diameters [2].

Symbol	Name	Equivalent Property of a sphere
x_a	Projected area diameter	Projected area if the particle is resting in a stable position
x_p	Projected area diameter	Projected area if the particle is randomly orientated
x_c	Perimeter diameter	Perimeter of the outline

Table 2. List of Definitions of equivalent circle diameters [2].

In practice, most of the equivalent diameters will be measured indirectly to a given number of particles taken from a representative sample and, therefore, it would be most practical to use a quick, less accurate measure on a large number of particles than a very accurate measure on very few particles. The measurement of particle size results dependent on the conventions involved in the particle size definition and also the physical principles employed in the determination process. It is recommended to select a characteristic particle size to be measured accordingly to the property or the process which is under

study. For this presented work, the process of study is fluidized bed, then it is the surface to volume diameter, that is, the diameter of a sphere having the same surface to volume ratio as the particle, which is more relevant to the aerodynamic process [1]–[3].

2.1.3 Shape

In particle behavior, shape is very important and just looking at the particle shapes, with no attempts at quantification, can be beneficial. Shape can be used as a filter before size classification is performed [1]–[3], [9]. The earliest methods of describing the shape of particle outlines used length L, breadth B, and thickness T in the elongation ratio (L/B) and the flakiness ratio (B/T). With one number shape measurements, the same single number may be obtained from more than one shape. Nevertheless, a measurement of this type which has been successfully employed for many years is the sphericity Φ_s [1], [2], [8], and defined by the relation:

$$\Phi_s = \frac{6V_p}{x_p s_p} \quad (1)$$

Where x_p is the equivalent diameter of particle, s_p is the surface area of one particle and V_p is the volume of one particle. For spherical particles, $\Phi_s = 1$, while for many materials, non-spherical, its value lies between 0.6 and 0.7, [1], [2]

2.1.4 Particle Density

The density of a particle is defined as its total mass divided by its total volume. It is considered quite relevant for determining other particle properties such as bulk powder structure and particle size, and so it requires careful definition. The true particle density represents the mass of the particle divided by its volume excluding open and closed pores and is the density of the solid material of which the particle is made. Depending on how the total volume is measured, different definitions of particle density can be given the true

particle density, the apparent particle density, and the effective particle density. Since particles usually contain cracks, flaws, hollows, and closed pores, it follows that all these definitions may be clearly different. Since most inorganic materials consist of rigid particles, while most organic substances are normally soft, porous particles, true density of many biological powdered materials would be considerably low than those of mineral and metallic powders. The apparent particle density is defined as the mass of a particle divided by its volume excluding only the open pores and is measured by gas or liquid displacement methods such as liquid or air pycnometry. The effective particle density is referred as the mass of a particle divided by its volume including both open and closed pores [1], [2], [9], [10].

2.1.5 Bulk Density

The bulk density of a powder is its mass divided by the bulk volume it occupies. The measurement of the bulk density of powders is fundamental to their storage, processing, and distribution. The volume includes the spaces between particles and the envelope volume of the particles themselves. The spaces between particles are denoted as porosity or voidage and can be defined as the volume of the voids within the bulk volume divided by the total bulk volume [1]–[3], [11]. Bulk density and porosity are related by:

$$\rho_b = \rho_s(1 - \varepsilon) + \rho_g\varepsilon \quad (2)$$

where ρ_b is the powder bulk density, ρ_s is the particle density, ε is the porosity, and ρ_g is the gas density. The value of the bulk density depends on the state of the powder, particularly on its state of compaction. The bulk is a mixture of air (or other gas) and the solid particles, so that the bulk density can be anywhere between the density of the two phases involved in the order of increasing bulk density, the following different definitions of this type of density that have been identified over the years are aerated bulk density, poured bulk density, tap density, and compacted bulk density. Each of these depends on the treatment to which the sample was subjected [1]–[3], [11].

In the literature there is still variety of how these terms are interpreted. Some authors consider the poured bulk density as loose bulk density, while others refer to it as apparent density. The actual meaning of aerated density can also be considered quite a confusing term. It should mean that the particles are separated from each other by a film of air and that they are, not in direct contact with each other. Some authors interpret the term as it would mean the bulk density after the powder has been aerated. Such an interpretation yields, in fact, the most loosely packed bulk density when, for cohesive materials, the strong inter-particle forces prevent the particles from rolling over each other. Considering this, aerated and bulk densities could both be simply regarded as loose bulk density, and this approach is implied in many investigations when dealing with cohesive powders [1]–[3].

For many fine and ultrafine powders, which are more likely cohesive in behavior, the terms more commonly used to express bulk density are loose bulk density, as poured and tapped bulk density, after vibration. Another way to express bulk density is in the form of a fraction of its particles' solid density, which is sometimes referred as the theoretical density. This expression, as well as the use of porosity instead of density, enables and facilitates the unified treatment and meaningful comparisons of powders having considerably different particle densities [1], [2], [12], [13].

2.1.6 Particle Classification

The different ways of classifying powders are closely related to the applications in which bulk properties play an important role. Since most applications in powder technology are relevant when considering powders as dispersion systems, they can be classified into different categories according to their behavior in dynamic situations. For this reason, powders or dry particulate materials can be categorized according to their handling properties. The classification depends on the type of handling in question, with the cases of deaerated state and aerated state being most important. The classification of powders in the deaerated state is known as Jenike's classification, while the classification of

powders in the aerated state is called Geldart's classification [1], [3], [14], [15]. For purposes of this work, the Geldart's Classification is going to be discussed.

A suitable manner of making a powder behave as a fluid is to suspend its individual particles within a stream of gas. When any stable suspension of solid particles of a powder in a gas stream is achieved, it is said that the powder has been fluidized. A powder that can be fluidized would be most properly defined as: disperse diphasic system in which the disperse phase consists on particles of a finely divided solid and the continuous phase consists of a gas. The solid particles conform to a sort of mechanical network due to certain interparticle forces. The net can be expanded under some conditions but will reassume its packed state under the influence of gravity. The packed, stationary state of a mass of powder presents mechanical resistance and some degree of elasticity. The interaction particle–gas is fundamental, and determines primarily the flowing capacity of the powder [1]–[3], [8], [9], [11], [14].

Regarding to the aerated state, a widely accepted classification of powders is the one proposed by Geldart in 1973, [15], which takes the two most important particle properties into account: particle size and particle density. Geldart's classification is basically derived from the behavior of powders when fluidizing by air at ambient conditions. In the fluidizing state, a bed of powder starts expanding when the fluidizing air reaches a critical velocity known as minimum fluidizing velocity. Considering the different ways of powders in expansion, Geldart suggested four types of powders. Powders can be termed as A, B, C, and D type [1], [14]–[16]. These concepts are summarized in Table 3.

Powder Type Name	Description
A	Collapse at a constant rate
B	Powders are known as sand like and present bubbling at the minimum fluidization velocity with a small bed expansion
C	Called cohesive and are difficult to fluidize at all. When the minimum expansion velocity is surpassed, these powders do not expand or form bubbles
D	Simply known as large and can form stable spouted beds if the air is admitted only through a centrally positioned hole.

Table 3. Geldart's classification powders according to the fluidization behavior of powders

Brief overview of starches and TiO₂

For this work, two powders were chosen. One organic and one inorganic, potato-starch, and Titanium Dioxide (TiO₂) respectively. On this section the relevance for surface modification of these two powders will be discussed. For the case of the potato-starch, starches will be discussed and then the specific type of the potato.

On their natural form, starches are unsuitable for many modern applications and require physical and/or chemical modification to enhance their positive attributes and/or to minimize their defects. Some of its properties during the processing of starch are highly dependent on the way granules are arranged and configured. The gelatinization process, which involves heating the starch granules in the presence of water generates molecular disorganization which is highly sensitive to starch composition. The gelatinization process causes irreversible changes in starch properties such as swelling, granular disruption, crystal melting, loss of birefringence and amylose leaching. For the development and production of starch-based materials, the plasma treatment for surface modification is a promising route for creating specific purpose starches [5]–[7], [17], [18].

Titanium dioxide is a non-toxic and environmentally satisfactory granular material, great commercial utility and with vast industrial applications, ranging from pigments to environmental purposes. The most common use of titanium dioxide is as the white pigment

in many formulations; it is difficult to find any white-colored object which does not contain TiO_2 . In addition, TiO_2 is employed in many plastic, paper and other materials to control the hue of colored products. Several new non-traditional pigment applications of TiO_2 have been developed for example, in the environmental sciences area, from the discovery, in 1972, that TiO_2 rutile single crystal electrodes can be employed to photochemically split water into hydrogen and oxygen. This observation has led to extensive interdisciplinary research activities of photocatalytic properties of TiO_2 . For example, photocatalytic activity of TiO_2 has been utilized for the purification of wastewater by decomposing non-biodegradable organic and ionic contaminants. Another example is fabrication of TiO_2 containing photoelectrochemical cells having photovoltaic conversion efficiency in excess of 10 %. These cells consist of an organic dye TiO_2 nanoparticle layer approximately 10 μm on indium-tin oxide or fluorine doped tin oxide glass optically transparent electrodes. There is a growing interest in treating this powder due to its important applications: is used primarily as a component of paints and plastics, paper, leather, the treatment of ceramics, as an additive in food or as an ingredient in cosmetics and pharmaceuticals conversion of toxic wastes to benign materials via photocatalytic oxidation or reduction reactions. There is a lack of information regarding the effect of atmospheric plasma treatment on the properties of this powder [19], [20].

2.1.7 Starches

Starch is a polysaccharide stored in plants and other biological sources in different forms; the most abundant carbohydrate reserve in plants and is found in leaves, flowers, fruits, seeds and different types of stems and roots. Like any other organic material, starch has a high biodegradability potential. Only cellulose is more abundant as a plant derived natural polymer. The biochemical chain responsible for starch synthesis involves glucose molecules produced in plant cells by photosynthesis. Starch is formed in the chloroplasts of green leaves and amyloplasts, organelles responsible for the starch reserve synthesis of cereals and tubers. Starch reserves produced by amyloplasts are deposited over several days, or even weeks and stored and cyclically mobilized during seed germination, fruit

maturation and the sprouting of tubers. Major starch sources are shown in Table 4 , for the immature fruits, for example bananas or mangos, the percentage is taking in consideration the starch by dry weight [21]–[26].

Starch Source Type	Percentage
Cereals	40% to 90%
Roots	30% to 70%
Tubers	65% to 85%
Legumes	25% to 50%
Some Immature fruits	70%

Table 4. List of major starch sources with their respectively percentage of starch content [21].

The accumulation pattern of starch granules in each plant tissue, shape, size, structure, and composition is unique to each botanical species. Starch consists of two polymers of different structure: amylose and amylopectin. The relative amount of each polymer and the physical organization in the granule structure give specific physicochemical and functional properties to the starch. Amylopectin consists of linear chains of glucose units linked by α -1,4 glycosidic bonds and is highly branched at the α -1,6 positions by small glucose chains at intervals of 10 nm along the molecule’s axis; it constitutes between 70 to 85% of common starch. By the other hand, Amylose is essentially a linear chain of α -1,4 glucans with limited branching points at the α -1,6 positions and constitutes between 15-30% of common starch. Amylose and amylopectin can be arranged in a semi-crystalline structure forming a matrix of starch granules with alternating amorphous (amylose) and crystalline (amylopectin) material, which is known as the growth rings in superior plant starch [18], [21]–[25].

Cereal starches contain lipid molecules in their structures in the form of phospholipids and free fatty acids; they are associated with the amylose fraction and contains approximately 0.6% of protein associated with the molecule. The origins of protein and lipids on starch

are situated on the granule surface. Lipids and proteins in starch granules can raise its functionality. Starch also contains a relatively small quantity (<0.4%) of minerals, such as: calcium, magnesium, phosphorus, potassium, and sodium. Phosphorus is of primary importance and is present in starch in three main forms: monophosphate esters, phospholipids and inorganic phosphate. The length of the α -glucan chains, amylose-amylopectin ratio and branching degree of amylopectin define the size, structure, and utility of starch granules in each plant species. Other characteristics associated with the granule such as form, surface type and phosphate groups influence the starch's properties and use. Like any other organic material, starch has a high biodegradability potential. As such, it has found a very important commodity in industry, particularly in food. Amylose is anhydrous and can form excellent films, which are important characteristics for industrial applications [18], [21], [22], [24], [25].

Starch is rarely consumed in its intact form and frequently used by industry in its native form. Most native starches are limited in their direct application because they are unstable with respect to changes in temperature, pH and shear forces. Native starches show a strong tendency for decomposition and retrogradation. Additionally, some starch granules are inert, insoluble in water at room temperature, highly resistant to enzymatic hydrolysis and consequently lacking in functional properties. Native starches are often modified to develop specific properties such as solubility, texture, adhesion and tolerance to the heating temperatures used in industrial processes [18], [21], [25], [27], [28].

2.1.7.1 Characteristics of starch granules: morphology, size, composition and crystallinity

Starch granules have microscopic sizes with diameters ranging from 0.1 to 200 μm , and its morphology varies between different shapes, such as: oval, ellipsoidal, spherical, smooth, angular and lenticular, depending on the botanical source. Common cereals such as wheat, barley and rye contain two types of starch granules: A-type, lenticular shape and large size

and B-type, spherical shape and small size. The amount of amylose present in the granule significantly affects the physicochemical and functional properties of starch and its content can vary within the same botanical variety because of differences in geographic origin and culture conditions. The role of amylose in the initial resistance of granules to swelling and solubility, as swelling proceeds rapidly after leaching of amylose molecules. The capacity of amylose molecules of forming lipid complexes prevents their leaching and consequently the swelling capacity. Phosphorus, presented as monoester phosphates or phospholipids in various types of starches, is one of the non-carbohydrate components present in the starch granule and significantly affects its functional characteristics. Associated with the amylopectin fraction by covalent bonds, increasing the clarity and viscosity of the paste, whereas the presence of phospholipids results in opaque and low viscosity pastes. The phospholipid content in starch granules is proportionally related to amylose and tend to form complexes with amylose and long branches of amylopectin, resulting in starch granules with limited solubility. The nature of the phosphorus in starch granules has an important influence on the transmittance of the paste; starches such as wheat and rice with high phospholipid contents produce pastes with low transmittance power compared to potato or corn starch pastes because the latter starches contain less phospholipids. Potato starch demonstrates high transmittance due to its phosphate monoester content [21], [24], [25], [27], [28].

Amylose associated with large branches of amylopectin molecules comprise the amorphous region of granules, and amylopectin molecules with short branches comprise the crystalline region; therefore, a higher proportion of amylopectin in starch granules results in greater crystallinity. There are three types of crystalline structures: A-type characteristics from cereal starches, B-type found in tubers and C-type present in legumes. Crystalline structures are based on the double helix formed by the amylopectin molecule. In A-type structures, the amylopectin branches are short and linked by α -1,6 bonds. A-type is characteristic of amylopectin ramifications. In B-type, the glucose chains are more polymerized and can act as bases where the branches are A-type or form branched amylopectin molecules. One of the most important structural characteristics of starch is that

it passes through several different stages from water absorption to granule disintegration. Water absorption and consequent swelling of the starch granule contribute to amylopectin-amylose phase separation and crystallinity loss, which in turn promotes the leaching of amylose to the intergranular space. When starch molecules are heated in water excess, the semi-crystalline structure is broken, and water molecules associate by hydrogen bonding to hydroxyl groups exposed on the amylose and amylopectin molecules [18], [21], [24], [25].

This association causes swelling and increases granule size and solubility; the swelling capacity and solubility of starch illustrate the interactions of the polymeric chains comprising the amorphous and crystalline granule fractions. The extent of this interaction is influenced by the amylose-amylopectin proportion and is characteristic of each molecule depending on the polymerization degree, length and grade of chain branching, molecular weight and molecular conformation. The swelling capacity of starch is directly associated with the amylopectin content because the amylose acts as a diluent and inhibitor of swelling. Some species of starch that contain amylose-lipid complexes exhibit swelling capacity and solubility restrictions. Water absorption and heating of the starch dispersion breaks the hydrogen bonds responsible for granule cohesion, partially solubilizing the starch. Water penetrates the interior of the starch granule, hydrating the linear fragments of amylopectin. This process leads to irreversible swelling, increasing the granule size several folds and the paste viscosity. Paste viscosity is essentially the principal measure of the potential application of starch in industry [18], [21], [24], [25], [27], [28].

Starch, when heated in the presence of excess water, undergoes a transition phase known as gelatinization, and there is a temperature interval for gelatinization corresponding to each starch species. Gelatinization occurs when water diffuses into the granule, which then swells substantially due to hydration of the amorphous phase causing loss of crystallinity and molecular order. Gelatinization occurs initially in the amorphous region, favored by the weak hydrogen bonds present in this area. The process then extends to the crystalline region. Amylose presence reduces the fusion point in the crystalline region and the amount

of energy necessary to initiate gelatinization. The gelatinization process is represented by transition temperatures and gelatinization enthalpies in the paste, and these measures are characteristic for each species. High transition temperatures correspond to a high degree of crystallinity, high stability and resistance of the granule structure to gelatinization. Gelatinization of starch granules is associated with a loss of birefringence and crystalline order due to the breaking of the double helix in the crystalline region and the leaching of amylose. Similar to water, other solvents are also used to promote gelatinization. The principal consideration with solvents is their capacity to form hydrogen bonds with the molecules in the starch granules. The gelatinization process is affected by solvent type and starch/solvent proportions [18], [21], [24], [25], [27], [28].

Gelatinization affects the rheological properties and viscosity of the paste, making the starch granule more accessible to enzymatic action. When starch granules swell, and its components are in solution, the medium properties change from a simple starch granules suspension to a starch paste. Amylose and amylopectin form separate phases because of thermodynamic immiscibility. The molecular interaction produced after gelatinization and cooling of the paste is known as retrogradation. During retrogradation, amylose molecules associate with other glucose units to form a double helix, while amylopectin molecules recrystallize through association of its small chains. After retrogradation, starch exhibits lower gelatinization and enthalpy compared to native starch because its crystalline structure has been weakened. Starch paste forms immediately after gelatinization, and starch granules are increasingly susceptible to disintegration by shearing because they are swollen. The paste obtained is a viscous mass consisting of one continuous phase of solubilized amylose and/or amylopectin and one discontinuous phase of the remaining starch granules. The characteristics of the native starch, the effects of the physical or chemical modifications of the granules, the process parameters and the botanical sources of the starch are all critical factors governing the behavior and characteristics of the starch paste [18], [21], [24], [25], [27], [28].

Starch granules are insoluble in cold water due to the hydrogen bonds and crystallinity of the molecule. When starch is dispersed in hot water below its Transition Temperature (T_g), the starch granules swell and increase several times in size, breaking the molecules and consequently leaching amylose to form a three-dimensional network and increase the paste's viscosity. T_g is an important parameter affecting the physical properties of polymers. Glass transition occurs similar to a thermodynamic second order transition, where the specific volume and enthalpy are functions of temperature. T_g describes the induction temperature of the progressive transition from an amorphous state to a rubbery state as the material is heated, generally in the presence of a solvent or plasticizer when referring to polysaccharides [18], [21], [24], [25], [27], [28].

Rheological properties describe the behavior of materials subjected to shearing forces and deformation, which are considered viscoelastic complexes. The basic feature of starch rheology is its viscosity. Other rheological characteristics involve texture, transparency or clarity, shear strength and the tendency for retrogradation. Rheological starch properties are studied through the behavior of viscosity curves, which are influenced by temperature, concentration and shear stress. Paste properties is the term used to describe the changes that occur in starch after gelatinization in excess water. Suspensions typically exhibit a peak in viscosity that starts after gelatinization and increases as the granules swell, followed by a decrease in viscosity due to granule disintegration and polymer realignment. A breakdown is defined by a difference between the viscosity peak and the minimum viscosity at the maximum analysis temperature. During the cooling period, amylose leaching forms a gel. Gel formation further increases the viscosity, called the cold paste viscosity. The difference between the paste viscosity at the end of the cooling period and the minimum viscosity at 95 °C is termed the setback. Starch gels are composed of amylose chains and intermediate materials dispersed in a starch suspension after granule disintegration in a three-dimensional network structure [21], [25], [27], [28].

Several parameters describe the viscoelastic behavior of pastes: the measure of recovered energy in each deformation cycle and an indicator of the elastic behavior of the paste (G');

the dissipated energy (G''), the loss of energy in each deformation cycle that describes the viscosity behavior of the material; and the modulus (G''/G'), describing the material's behavior, high values (>1) indicate liquid-like behavior, and low values indicate solid-like (<1) behavior. The rheological properties of starch determine its potential application as a thickener or gelling agent [21]. Determining the thermal properties of starch involves terms such as: the onset temperature (T_o), peak temperature (T_p), conclusion temperature (T_c), difference between T_c and T_o , and enthalpy of fusion, all of which can be measured using equipment like a differential scanning calorimeter (DSC) and depends on the starch concentration. During heating, T_o , is the temperature at which the paste viscosity starts to increase; T_p is the maximum viscosity temperature; and T_c is the final temperature of the viscosity increment. (T_c-T_o) is a comparative measure, and an increase in this value indicates a high amount of granule modification in the amorphous and crystalline regions. This paste property typically begins 20 °C lower than its gelatinization temperature (T_{gel}), and retrogradation is proportional to the presence of amylopectin. Variations in a starch's thermal properties after gelatinization and throughout refrigerated storage can be attributed to variations in the amylose/amylopectin ratio, the size and shape of the granule, and the presence or absence of lipids and proteins [21], [24], [25], [27], [28].

2.1.7.2 Potato Starch

The overall starch market is continually expanding, and the current demand is covered by four conventional sources: wheat, corn, potato and cassava [21], [24], [25], [29]. And other such as: rice and tapioca [5], [7], [25], [30]. There are significant differences in the starch properties of these conventional groups in addition to the differences in their amylose-amylopectin ratios and the characteristics of these molecules. Non-amylose components such proteins, lipids and phosphate groups are also important differences in the characteristics of conventional and unconventional starches [18], [24], [25].

2.1.8 Titanium Dioxide

Titanium dioxide (TiO_2) is an inorganic, nontoxic and environmentally satisfactory granular material that might crystallize to different modifications. It is widely used in industry for its vast applications. Primarily is used as a component of paints and plastics, paper, leather, the treatment of ceramics and also as an additive in food or as an ingredient in cosmetics and pharmaceuticals, used as pigment in the coloring industry. TiO_2 adds matt shine to the fibers, in the paper mill TiO_2 is added to white papers and to thin papers that are supposed to be non-transparent. Also is added to enamel, pottery, cement and white rubber [19], [20].

Plasmas:

In the simplest term, plasma is the fourth state of matter. At room temperature, there is matter that exists in the solid state, some in the liquid state and some in the gaseous state. Each kind of matter can also exist in all the three states if it is heated to temperature above room temperature and cooled to below room temperature. For example, when a solid is heated it becomes a liquid; heating a liquid turns it into a gas, upon further heating, the gas is ionized into a plasma. Since a plasma is made of: molecules, atoms, positive ions, species and electrons, which are charged, electric fields are rampant everywhere, and particles “collide” not just when they bump into one another, but even at a distance where they can feel their electric fields [31]–[34], as seen in Figure 1 as an illustration of the common example of a plasma.

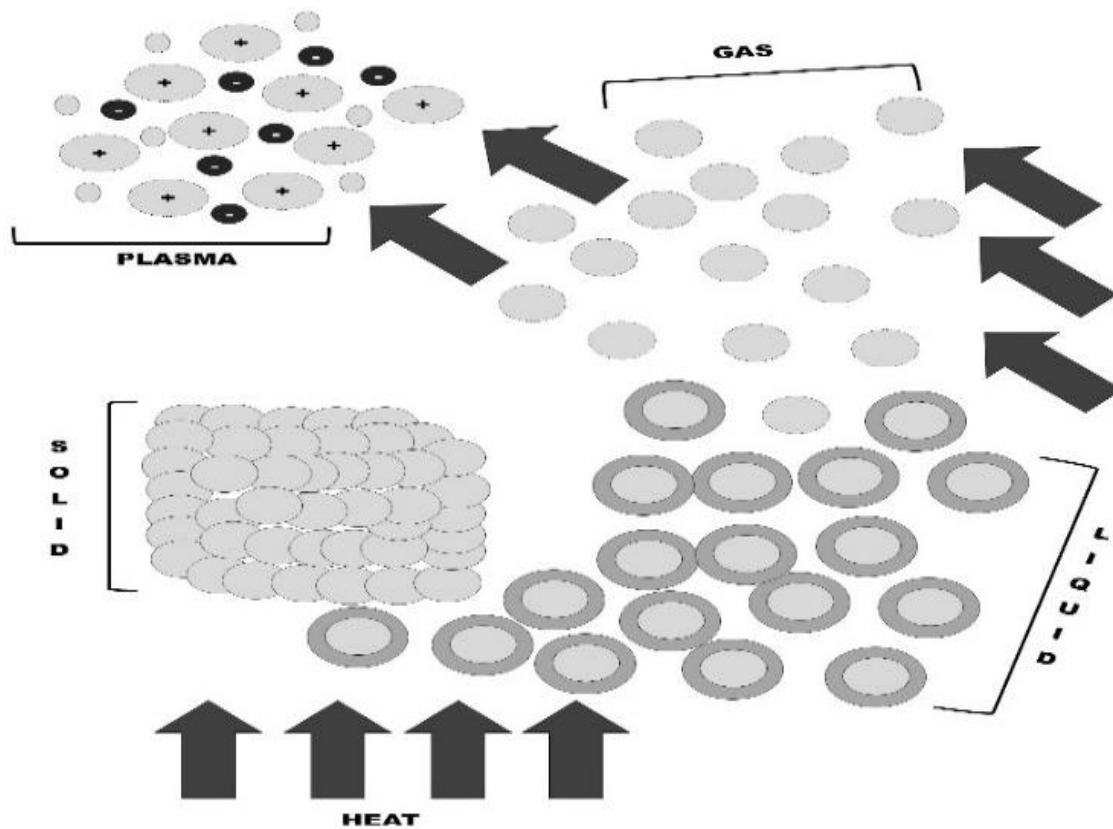


Figure 1. Common example of the four states of matter

The plasma is an ionized gas. Inside the plasma, as mentioned, there are, species, electrons, ions of various charge states, neutral atoms, and molecules. These particles move around inside the plasma with kinetic energy; the particles may exchange energy when they collide with each other, the collisions can be either elastic or inelastic. During an elastic collision, the particles only exchange kinetic energy. The magnitudes and directions of the velocities of both colliding particles may be changed after the collision. During an inelastic collision, the internal energy of the colliding particles may be changed, leading to the occurrence of various types of processes such as excitation and ionization. In particular, ionization gives rise to the production of new charged particles and hence causing the number of charged particles to increase [31]–[36].

The term plasma was first used by Langmuir in 1927 and derives its name from the Greek to shape or to mold and the analogy with biological plasma, which is an electrolyte, and describes the self-regulating behavior of plasma in contrast to the apparently random behavior of fluids [31], [32], [34], [36]. The science of plasma encompasses: space plasmas, kinetic plasmas and technological plasmas and ranges over enormous variations of parameters such as pressure, distance and energy [31], [32], [36]. Technological plasmas were used for this work and will be discussed in Section 2.1.9 Plasma theory. One method of distinguishing different areas of plasma technology that is often used is as hot or cold plasmas, as presented on Table 5, depending on the relative value of the ion temperature T_i to the electron temperature T_e [31], [32], [36]. Other common descriptions used are glow, corona, arc and beams. The subject of plasma is better described as a continuum in terms primarily of the potential energy of electrons T_e and ions T_i and the electron number density n_e [31], [32], [36].

Low-temperature thermal cold plasmas	Low-temperature non-thermal cold plasmas	High-temperature hot plasmas
$T_e \approx T_i < 2 \times 10^4 K$	$T_e \approx T \approx 300 K$ $T_e \ll T_e \leq 10^5 K$	$T_e \approx T_e > 10^6 K$
Arcs at 100 kPa	Low pressure ~ 100 Pa glow and arc	Kinetic plasmas, fusion plasmas

Table 5. Temperature and pressure ranges of hot and cold plasmas [8].

The reason for plasmas' unique characteristics and relevance to high-energy processes is apparent from Figure 2, where the electron temperature T_e is shown for different plasma processes as a function of electron number density of the electrons [33], [34], [36], [37]. Energy and temperature are related by the Boltzmann constant, k_B , as shown on equation (3):

$$\frac{1}{2}mu^2 = k_B T \quad (3)$$

where $k_B = 1.38 \times 10^{-23} \text{ J K}^{-1}$ [36]. In a cold plasma such as a neon lamp, the kinetic energy equates almost entirely to the electron energy and, although the mean electron temperature may be several times room temperature, the number of hot electrons is only a tiny fraction of the total and their thermal mass is small compared with an atom or molecule, so that the average temperature increase is small. The potential and energy of most plasma processes are several orders of magnitude greater than those of most other processes [33], [34], [36], [37].

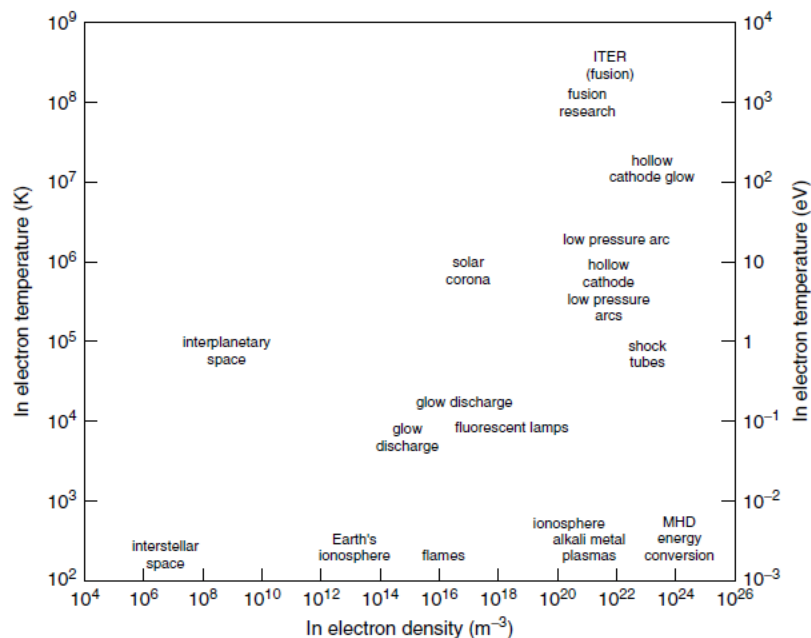


Figure 2. Plasma applications at different currents and gas pressures [8].

It is usually necessary to consider plasma parameters on an atomic level, including particle sizes, length and time scales, particle number densities, forces between particles and many other parameters, with respect to each other. Atomic particles resonate and the difference in resonant frequencies between electrons and ions due to their different masses adds a

further layer of complication, together with the fluid nature of a plasma and the ability to affect it with static and fluctuating magnetic fields. To this we may also add the ranges of conditions encountered, such as current and gas pressure [33], [34], [36], [37].

2.1.9 Plasma theory

Plasma in physics, is an ionized gas in which at least one of the electrons in an atom has been stripped free, leaving a positively charged nucleus, called an ion. Any ionized gas cannot be called a plasma, of course; there is always some small degree of ionization in any gas, a useful definition is as follows: quasineutral gas of charged and neutral particles which exhibits collective behavior. The meaning of quasineutrality can be explained by the Debye Length, (λ_D), which is a measure of the shielding distance or thickness of the sheath [31]–[34], [36].

$$\lambda_D \equiv \left(\frac{\epsilon_0 K T_e}{\eta e^2} \right)^{1/2} \quad (4)$$

A fundamental characteristic of the behavior of plasma is its ability to shield out electric potentials that are applied to it. The meaning of quasineutrality. If the dimensions L of a system are much larger than λ_D , then whenever local concentrations of charge arise or external potentials are introduced into the system, these are shielded out in a distance short compared with L , leaving the bulk of the plasma free of large electric potentials or fields. Outside of the sheath on the wall or on an obstacle, $\nabla^2 \phi$ is very small, and n_i is equal to n_e , typically to better than one part in 10^6 . It takes only a small charge imbalance to give rise to potentials of the order of KT/e . The plasma is “quasineutral”; that is, neutral enough so that one can take $n_i \approx n_e \approx n$, where n is a common density called the plasma density, but not so neutral that all the interesting electromagnetic forces vanish. A criterion for an ionized gas to be a plasma is that it be dense enough that λ_D is much smaller than L [31]–[34], [36]. Debye shielding can be foiled if electrons are so fast that they do not collide with one another enough to maintain a thermal distribution. The meaning of Collective behavior

is as follows. Consider the forces acting on a molecule of, say, ordinary air. Since the molecule is neutral, there is no net electromagnetic force on it, and the force of gravity is negligible. The molecule moves undisturbed until it makes a collision with another molecule, and these collisions control the particle's motion. A macroscopic force applied to a neutral gas, such as from a loudspeaker generating sound waves, is transmitted to the individual atoms by collisions. The situation is totally different in a plasma, which has charged particles. As these charges move around, they can generate local concentrations of positive or negative charge, which give rise to electric fields. Motion of charges also generates currents, and hence magnetic fields. These fields affect the motion of other charged particles far away. [31]–[34], [36], [37]

Technological plasmas are normally supplied with energy from electric power sources, although excitation from shock waves and chemical plasmas is possible and operate in the region from atmospheric pressure down to about 10Pa (75.2×10^{-3} Torr). Gas pressures as low as 10^{-11} Pa (7.52×10^{-14} Torr) are obtainable in the laboratory, but the use of plasmas is limited by the energy density at low pressures to about 100×10^{-3} Pa (0.752×10^{-3} Torr), at which the mean free path is of the order of 100mm [33], [34], [36], [37].

Technological plasmas are often referred to as cold plasmas since the neutral particle and ion temperatures are often much lower than the electron temperature [31]–[34], [36], [37]. If the length and time scales of changes of the electric field are long compared with the mean free path and collision frequency, the effects of collisions in a plasma result in a statistical distribution of velocities and energy. At gas pressures above about 0.133Pa (10^{-3} Torr), corresponding to particle densities of 10^{19}m^{-3} , plasmas can be considered statistically as a quasi-continuous fluid; below this there is a substantial separation between particles and the behavior is more accurately described by the behavior of individual particles (free electrons or ions), such as those in electron and ion beams. Because of collisions between electron and the atom or ion inside the plasma, various processes may occur. Four of the most elementary processes are presented on Table 6, [31]–[34], [36], [37].

<p>Scattering</p> $e + A \rightarrow A + e$	<p>This is caused by elastic collision where the colliding electron will transferred a small fraction of its kinetic energy to the atom or ion. However, its direction of motion will be changed.</p>
<p>Excitation</p> $e + A \rightarrow A^* + e$	<p>This occurs when electron of sufficient energy collides at an atom or ion inelastically. Part of its kinetic energy is absorbed by an inner shell electron of the atom or ion so that this inner shell electron is raised to a higher energy level and the atom or ion thus becomes excited. Most of the excited states have short life time and they will decay back to their original levels by emitting a photon equivalent to the energy difference. This process is called de-excitation or relaxation by spontaneous emission.</p>
<p>Ionization</p> $e + A \rightarrow A^+ + 2e$	<p>With sufficiently high energy, the colliding electron may transfer enough energy into the internal energy of the atom or ion to release one of the bound electrons. The atom or ion thus becomes one charge state higher and it is said to be ionized. It is through the ionization process that new charged particles (electrons) are produced in the plasma.</p>
<p>Recombination</p> $e + A \rightarrow A + (h\nu)$	<p>In this case the electron colliding with the ion may be captured and it occupies the vacancy inside the ion to change its charge state to one level lower than previously. A photon may be emitted when the electron releases its excess energy.</p>

Table 6. Description of the four most elementary processes due to collisions between electron and the atom or ion inside the plasma [31], [32], [36].

2.1.10 Methods of Plasma Generation

There are several ways for generating a plasma, as shown on Table 7. The plasma state is obtained by the application of energy into a gas for the electronic structure reorganization of the species (atoms and molecules) and for the excited ions and species production; this energy can be thermal or provided by an electric current or electromagnetic radiation [33], [34], [38].

Electric discharges are the more used method for plasma generation. These are classified as: corona or dark discharge, arc discharge, glow discharge and dielectric barrier discharge. To obtain the discharge it is necessary to excite the gas with one or several sources of voltage which can be direct current (DC), alternate current (AC), or by radio frequency (RF). These applications include DC and AC line frequencies, as well as assigned frequency bands across the entire electromagnetic spectrum from 1 kHz to 10 GHz [32]–[34], [38].

Plasma generation		
Electromagnetic Radiation	Electric Discharge	Electron Beam
Excited by microwaves (915 MHz, 2.54 GHz)	High voltage power source	Electron accelerator tubes
Ignition structure required	Obtained by pulses: DC, AC Frequency: (Hz - MHz)	Requires extensive facilities
Usually hot plasmas	Electric breakdown ruled by Paschen's Law	Recommended for high fluxes of gas

Table 7. List of different ways for plasma generation.

The essential components of a generic plasma reactor are shown in Figure 3. The DC and AC plasma reactors have a power supply connected directly to the reactor. Thus, all additional components required for RF operation between the DC power supply (which usually operates at kilovolt voltages in both cases) and the reactor represent an additional expense and additional sources of operational and reliability problems, compared to DC and AC plasma reactors [33], [34], [38].

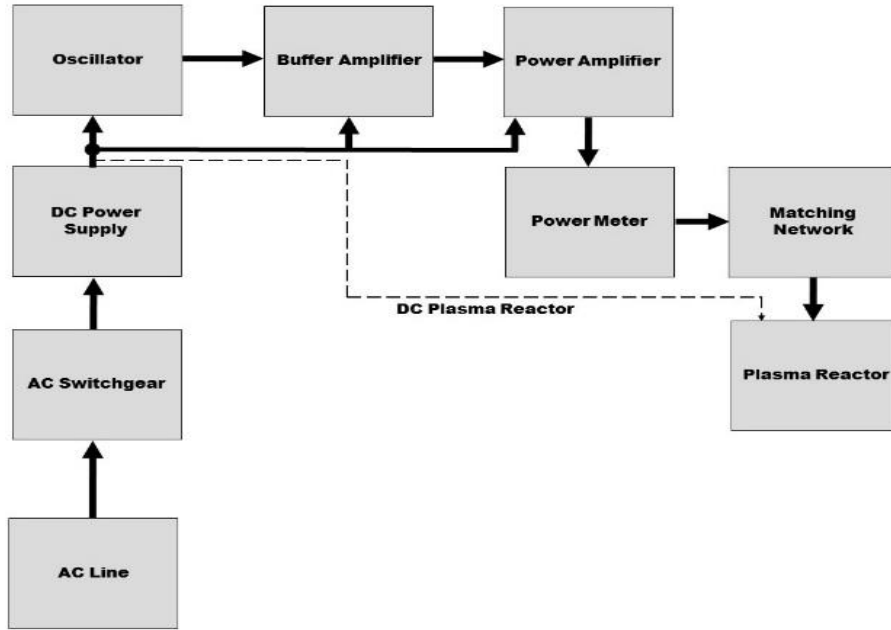


Figure 3. Essential components for a generic plasma reactor, adapted from [39].

The additional cost and complexity of RF power supplies and plasma reactors must be justified in terms of their operational advantages [33], [34], [39]. Such advantages have been identified for many industrial applications, and include the following:

- The RF power deposited in the plasma is transferred by displacement, not real currents [39]. This implies less electron and ion bombardment of the electrodes; easier coupling of power through the vacuum wall; less electrode heating; no, or much weaker, electrode jets of a kind discussed since there is one less mechanism for losing electrons and ions from the plasma containment volume [39].
- In general, it has been found that RF-generated plasmas offer greater stability of operation than an equivalent DC or AC plasma, particularly with respect to electrode effects, and the ability to function without mode transitions of the kind present in some DC or AC discharges [39].
- RF plasmas provide a higher electron kinetic temperature than an equivalent DC or AC plasma source of the same electron number density, and this can be beneficial

in applications where it is desired to increase the number of free radicals, plasma-chemical reactions, or dissociation and ionization reactions [39].

- RF generated plasmas often tend to have higher electrical efficiency than equivalent DC or AC plasma sources of the same volume and number density, partly because they have much lower electrode losses [39].

2.1.10.1 Electric Breakdown

In its neutral form, a gas is an insulator and will not conduct electrical current when an electric field is applied across it, no matter how high is that electric field. However, some number of stray charges are always present in the neutral gas. One such source of stray charges is the ionization of the gas particles by cosmic ray or any other background radiation from the environment. If the electric field is applied to the gas using electrodes, another source of stray charges (electrons) may come from the photoelectric effect at the cathode surface due to the absorption of UV photons. The presence of stray electrons is crucial in electrical discharge since they can be accelerated to high energy to produce ionizing collision and hence new charged particles. Without the presence of stray electrons, electrical discharge may not occur. The simplest configuration to produce an electrical discharge through a gas is to apply a potential difference across a pair of parallel electrodes placed inside a chamber filled with the gas at a suitable pressure as shown in Figure 4, [31], [32], [40].

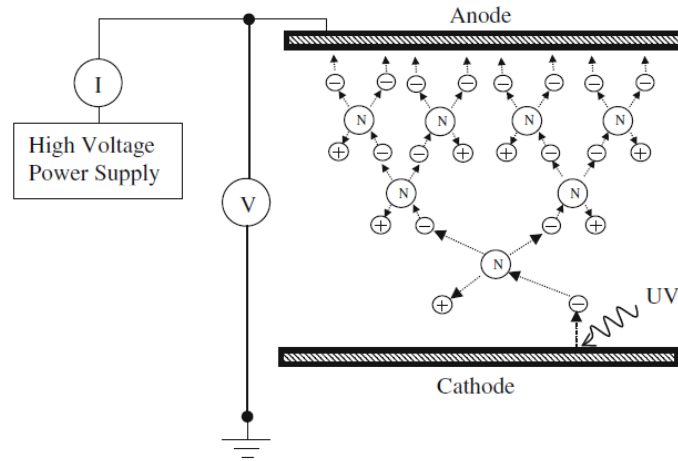


Figure 4. Simple schematic for the simplest configuration to produce an electrical discharge through a gas [32].

Consider an electron originated from the cathode due to the absorption of UV photons. With the presence of electric field, the electron will be accelerated to high enough energy for excitation or ionization when it collides with an atom. When an ionizing collision occurs, the colliding electron together with the new electron will be further accelerated by the electric field and they may produce further ionizing collisions [31], [32], [40].

2.1.10.2 Radio-Frequency Discharge

Gas discharge powered by an AC source can be considered not different from that maintained by a DC source if the frequency is low. Low frequency is the characteristic time of the voltage variation should be much larger than the transit time of the ions from anode to cathode. This is normally in the region of below 1 kHz. For high frequency, the discharge behavior becomes different from the DC case [31]–[34], [40], [41].

First, the breakdown voltage will be lower. In a self-sustained glow discharge, new charged particles are produced by the ionization of the gas by electron collisions and the secondary emission at the cathode surface by ion bombardment and this is balanced by the loss of electrons at the anode. For sufficiently high frequency (probably above 1 MHz) source, the

loss of electrons at the anode will be reduced (or even becomes zero loss) since the alternating field may reverse some or all of the electrons before they reach the electrodes. Although there will also be a reduction of electron production by ion bombardment at the cathode surface, this will be compensated by the reduction of loss of electrons at the anode and the increase in ionization in the gas since the electrons now remain in the plasma for longer time as they are moving back and forth following the electric field. In this case the main electron loss mechanism is radial diffusion [31]–[34], [40], [41].

One favorable condition for AC powered gas discharge is to employ sufficiently high frequency to ensure that the oscillation time of the electrons caused by the alternating electric field is shorter than their transit time between the electrodes, or $\omega\tau < 1$ where ω is the angular frequency of the field and τ is the electron transit time between electrodes. This is also dependent on the pressure of the gas as at lower pressure the electron transit time is expected to decrease. For pressure of a few torr and discharge distance of several cm, the use of frequency in the radiofrequency range is appropriate. A commonly used frequency is 13.56 MHz as agreed by international communication authorities. Under this condition we expect $\omega < \nu$ where ν is the electron collision frequency. This means that an electron collides many times within one oscillation of the electric field, so it may be able to transfer the energy it absorbs from the field to other particles [31]–[34], [40], [41].

For lower pressure, say in the region of mtorr, there may not be sufficient collision for the electrons to achieve equilibrium with other particles so that it is more effective to heat the electrons collectively. This requires frequency, electron plasma frequency ω_{pe} which is at the microwave region (>GHz). In an RF discharge, the plasma will not be off between cycles of the electric field variation, which is normally sinusoidal, although the electrons are expected to travel back and forth between the electrodes as the field changes direction. As a result, a steady plasma is formed between the electrodes. The condition of the plasma is expected to be like that of the DC discharge except that the potential distribution between the electrodes may vary during each cycle. An RF discharge can be produced by using 2 types of configurations: capacitively coupled or inductively coupled. The capacitive

coupling can be implemented with a set of parallel plates such as those used for the conventional DC glow discharge. For an RF power source, an electrode less discharge can be obtained by placing the electrodes outside the plasma chamber. This can eliminate the contamination of the plasma by the electrode materials. [31]–[34], [40], [41]

2.1.11 Plasma Parameters

As mention on the beginning of this section, plasmas are ionized gases. To understand the interaction of the plasma state with other objects and inside of it; it must be explained the important parameters of plasmas. Pressure, electron temperature and electron density are important parameters that define the plasma behavior. In general, the particles of a certain species located at a given point do not have the same velocity; they present, on the contrary, a distribution that in thermal equilibrium is described by the Maxwell-Boltzmann distribution. The higher the temperature, the greater the speed variation. [33], [34], [37]. The temperature T is proportional to the average kinetic energy $\langle E \rangle$ of a set of particles in thermal equilibrium with the ratio given by:

$$\langle E \rangle = \frac{3}{2} k_B T \quad (5)$$

Where k_B is the Boltzmann constant, with value 1.38×10^{-23} J/K, or 8.6173×10^{-5} eV/K. It is commonly used electron-volts for expressing the temperature of the species. For species where, relativistic effects are not presented, it can be defined the average thermal velocity of the particles, v_{th} :

$$v_{th} = \sqrt{\frac{2\langle E \rangle}{m}} = \sqrt{\frac{3k_B T}{m}} \quad (6)$$

Where, m is the particles mass. The density n and the temperature T are related by the equation of the ideal gas:

$$P = nk_B T \quad (7)$$

If $k_B T$ is given in Joules [J] and the pressure P in Pascals [Pa], the density n is going to be given in particles by m^3 , a unit commonly express as m^{-3} . The density n can be expressed in function of the pressure, as shown:

$$n = \frac{P}{k_B T} \quad (8)$$

Another important parameter in the plasma state is the mean free path λ_{mfp} , which is the average distance traveled before interacting with another particle particle in the system, and is given by:

$$\lambda_{mfp} = \frac{1}{\sigma n} = \frac{k_B T}{\sqrt{2} \pi d^2 P} \quad (9)$$

Where, σ is the effective section of interaction and is approximated with the square of the particle's diameter d^2 . Defining the mean free path and the average thermal velocity, the collision frequency ν_{col} can be defined as the inverse of the time it takes for a particle to travel a distance equivalent to the mean free path, and is given by:

$$\nu_{col} = \frac{v_{th}}{\lambda_{mfp}} = \frac{\sqrt{2} \pi d^2 P \sqrt{3k_B T}}{k_B T \sqrt{m}} = \sqrt{\frac{6}{mk_B T}} \pi d^2 P \quad (10)$$

In addition to the neutral gas, which has the behavior that can be described by the kinetic theory of gases, a plasma also contains species with charge, product of the partial ionization of the gas. The densities of ions and electrons in a system are denoted by η_i and η_e , respectively [33], [34], [37]. In most cases, the plasma contains the same number of positive and negative charges, which cancels the total load of the system, although local variations are allowed. In this case it is spoken of a neutral or quasi-neutral plasma.

The possibility of spatial variation of the charges leads to the concept of shielding distance, also known as the Debye length, which is the scale through which more mobile charge carriers, for example electrons, can generate a shielding of electric fields in plasmas and other conductors; that is, it is the distance over which a significant load separation can occur and provides a measure of the typical lengths in a plasma. In a plasma, the length of Debye, considering both negative ions and electrons is given by the following equation:

$$\lambda_D = \sqrt{\frac{\epsilon_0 k_B}{e^2 \left(\frac{n_e}{T_e} + \sum \frac{Z_j^2 n_j}{T_j} \right)}} \quad (11)$$

Where, λ_D is the Debye Length, ϵ_0 is the vacuum permittivity, e is the electron charge, T_e and T_i are the temperatures of the electrons and negative ions, respectively, n_e is the electron density and n_j is the density of the ions j with negative charge Z_j [33], [34], [37]. If the negative ions are not considered, equation 11 can be simplified, (as presented in equation 4) as:

$$\lambda_D = \sqrt{\frac{\epsilon_0 k_B T_e}{n_e e^2}} \quad (12)$$

For practical purposes, it can be taken the following expression that groups the constants:

$$\lambda_D = 7430 \sqrt{\frac{k_B T_e}{n_e}} \quad (13)$$

Where, n_e is given in particles/m³, $K_B T_e$ is given in eV and λ_D in meters. The number of charges within a sphere with a radius measuring the Debye length, its known as the parameter of the plasma, Γ . According to the plasma definition in which the electromagnetic interaction of a single particle with all the distant particles dominates over the interaction with the lesser neighboring nearby, can be written in terms of the parameter of the plasma as: $\Gamma \gg 1$. Physically this condition implies that there is a great number of particles

contained in a Debye sphere; some authors used an inverse definition of the parameter of the plasma ($g = 1/\Gamma$), in which the condition of the plasma results as $g \ll 1$ [33], [34], [37].

It can also be defined a characteristic time scale parameter for the plasma; the frequency of the plasma ω_p describes the characteristic natural time of oscillation of the plasma when is submitted to a perturbation. Suppose that a small displacement of all the electrons in one direction is introduced into a plasma in equilibrium and without charge densities. These will feel the attraction of the ions in the opposite direction, move towards it and begin to oscillate around the original equilibrium position. The frequency of such oscillation is called plasma frequency, which for the electrons $\omega_{p,e}$ is obtained by:

$$\omega_{p,e} = \sqrt{\frac{4\pi\eta_e e^2}{m_e}} \quad (14)$$

Where m_e is the mass of the electrons and η_e is the density of the electrons. The product of the Debye length and the frequency of the plasma is related to the average thermal speed of the electrons, by means of the following expression:

$$\lambda_D \omega_{p,e} = \sqrt{\frac{4\pi\epsilon_0 k_B T_e}{m_e}} = v_{th,e} \sqrt{\frac{4\pi\epsilon_0}{3}} \quad (15)$$

Another important parameter in the study of plasmas is the ionization level that plasmas can achieve. This means, the relationship between the amount of charge particles against the total amount of present particles, allowing to specify the behavior of the plasma. It depends mainly on the temperature and it is possible to deduce it in a first approximation from the Saha equation, valid for a plasma in thermal equilibrium that contains ions that have been ionized only once and where U_i is the first average ionization potential and h is the constant of Planck [33], [34], [37].

$$\frac{\eta_e^2}{\eta - \eta_e} = 2 \left(\frac{2\pi m_e k_B T_e}{\hbar^2} \right)^{3/2} \exp\left(-\frac{U_i}{k_B T_e}\right) \quad (16)$$

2.1.12 Atmospheric plasmas

Most plasmas are created in vacuum systems, but it is also possible to produce plasmas at atmospheric pressure. For instance, a jet of argon and helium can be ionized with radiofrequency power. Industrial substrates can be processed by sweeping such a jet to cover a large area. Large atmospheric-pressure plasmas can also be produced for roll-to-roll processing [31], [35], [38], [42].

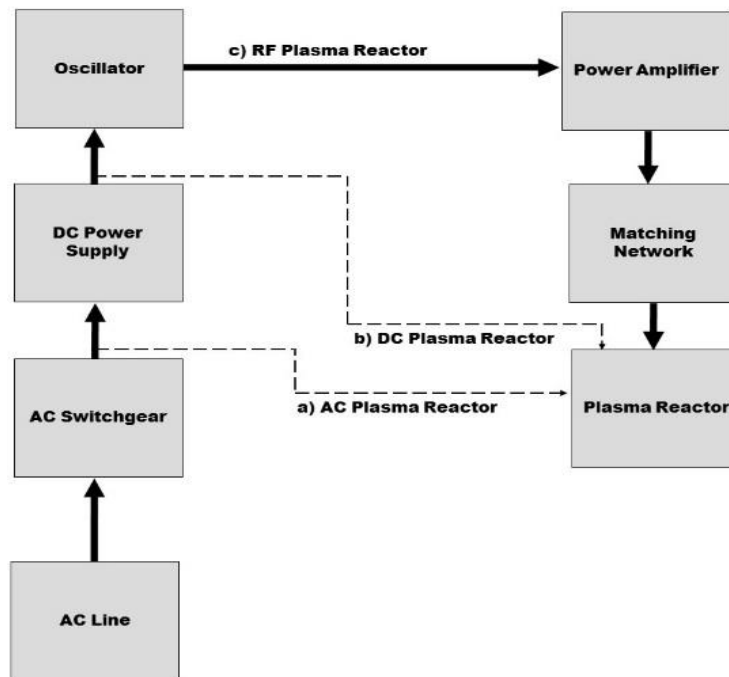


Figure 5. Schematic diagram of power supply components needed for plasma sources that require (a) AC line voltage only; (b) DC electrical power; and (c) RF power. Adapted from [38].

2.1.12.1 The Dielectric Barrier Discharge

For the surface modification by plasma treatment, different types of reactors exist, according to the discharge configuration used, Figure 6. The most common method is the Dielectric Barrier Discharge (DBD), first reported by Siemens in 1857, concentrating on the generation of ozone. The Dielectric Barrier Discharge (DBD) is an artificial method for obtaining plasma. This method is increasing in popularity as a source of non-thermal plasmas at atmospheric pressure. Atmospheric plasmas are a rich source of radicals, excited and ionized species under affable conditions. However, unlike vacuum operation which easily leads to a stable, uniform nonthermal plasma, it is difficult to obtain a plasma with these attributes at near atmospheric pressure. There are essentially two methods for producing nonthermal plasmas: corona discharge (CD) and DBD. The DBD systems have several advantages, such as lower voltage consumption, current limitation to avoid transition to arc, a high-energy coupling of the DBD discharge, and low level of UV radiation emission. For this method there must be one dielectric barrier, usually silica glass, and the discharges need an alternating voltage for the proper operation. The dielectric constant and the thickness combined with the time derivative of the applied voltage determine the amount of displacement. For there to be a current transportation in the discharge gap, the electric field has to be high enough to cause breakdown in the gas. And the plasma state is achieved [33], [34], [40], [41], [43].

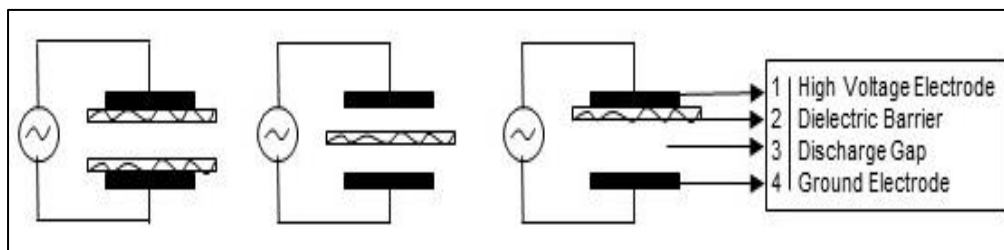


Figure 6. Schematic for the Dielectric Barrier Discharge, [40].

Fluidization

Fluidization occurs when the solid powder particles or granule particles, are suspended in a container using a continuously upward flowing fluid (gas in the case of this work). The powder particles are suspended through the fluid with a high enough drag force to overcome the downward force of gravity. The drag force is the frictional force imposed by the gas on the powder particle; also the powder particle imposes an equal and opposite drag force on the gas. The movement of a gas through a fluidized-bed can be described using the two-phase theory: gas moves through the bed in two ways, as bubbles and as part of an emulsion or dense phase, Figure 7. Up to the minimum fluidization point, all gas moves through the bed via the emulsion phase. Beyond the minimum fluidization point, any additional gas introduced should travel through the bed as bubbles. Larger bubbles travel faster than smaller bubbles, so managing bubble size is an important design criterion [1], [11], [44], [45].

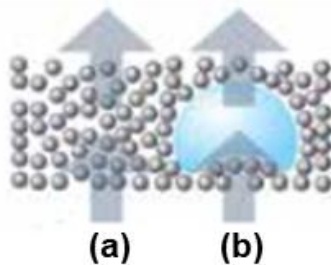


Figure 7. In a two-phase fluidization, gas moves through the particle bed, (a), and as an emulsion or dense phase, (b). The picture was adapted from [11].

As a particle becomes more fluidized, it affects the local gas velocity around it due to the drag forces. This effect is minimal for spherical particles, but the influence of the drag force is more significant for irregularly shaped particles. When the gas velocity is high enough, that the drag force on the particles equals the weight of the particles, the bed becomes fluidized. This point is commonly referred to as minimum fluidization velocity, u_{mf} . When the gas velocities increase beyond the u_{mf} , bubbles can form. The point at which this occurs

depends on the particle size and density. Smaller or lighter particles tend to experience smooth fluidization before bubbles appear. Larger or denser particles tend to start bubbling at the point of minimum fluidization. The attainment of the fluidization conditions is closely related to the intrinsic properties of the particles being fluidized including density, shape, size distribution, and surface characteristics [1], [10], [11], [45], [46]. Depending on these properties and the density difference between the particles and the fluid, the powders will fluidize differently, and the behavior falls into one of the four groups on the Geldart Classification: A, B, C, or D [11], [15], [46], [47]. For this work, two types of powders were selected: one type-A organic (potato starch, PS) and one type-C inorganic (titanium dioxide TiO_2).

2.1.13 Fluidization Theory

The type of fluidization changes as the gas velocity through the bed continues to increase, as shown in Figure 8. The bed transitions from a bubbling fluidized bed to a turbulent fluidized bed in which the gas voids are no longer regularly shaped bubbles, but elongated shapes. The top of the bed becomes less well defined due to the increase in entrained particles. At even higher gas velocities, all of the particles are entrained out of the bed. Further increases in the superficial gas velocity result in complete conveying of all of the particles [1], [11], [44], [45].

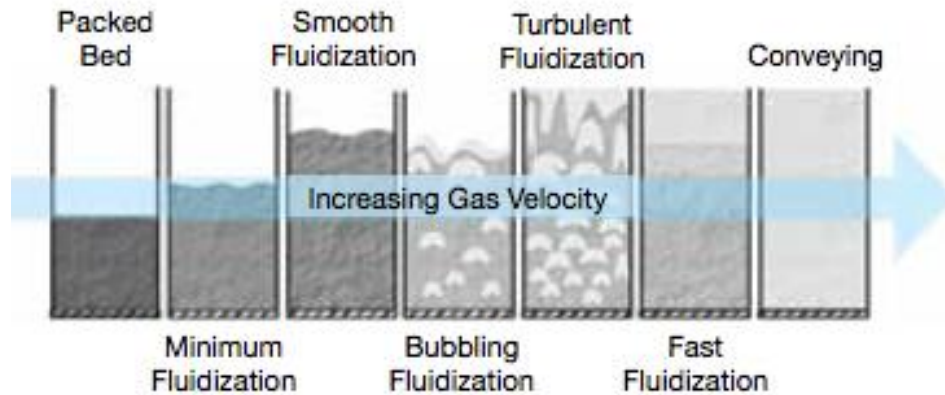


Figure 8. Representation of the types of fluidization as the gas velocity through the bed increases. Adapted from [11].

There are many variations in bed hydrodynamics based on particle properties, so the prediction of the behavior of the fluidized bed is complicated. However, the works of Geldart and Abrahamsen, [14]–[16], provides criteria for predicting the fluidization behavior, and Geldart, [15], classified this behavior into four groups, presented in Figure 9, named as: Geldart Groups A, B, C and D. Gas pressure can cause a particle’s classification to change, which is not captured in the Geldart’s chart, (Figure 9), [1], [11], [15].

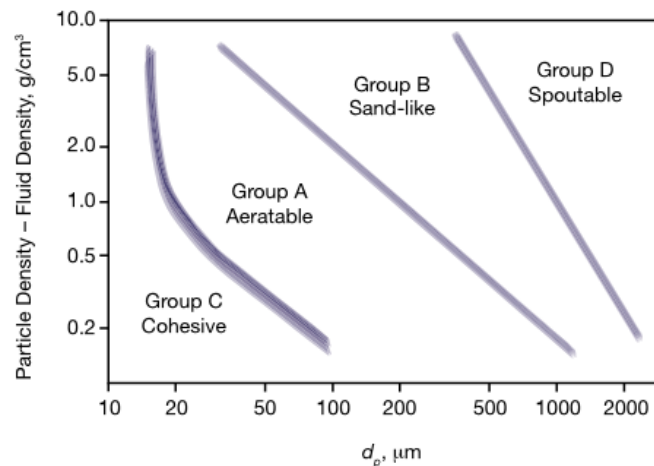


Figure 9. Fluidization behavior of particles, adapted from [11].

Geldart Group A particles or Type-A powders, tend to be aeratable, have particles ranging 10 to 125 μm and particle densities of about 1,500 kg/m^3 ; particles in this group tend to fluidize easily. Group A powders do not promote maximum bubble sizes larger than 20 cm, at low gas velocities, exhibit bed expansion without the formation of bubbles. Geldart Group B particles or Type-B powders, have particle sizes ranging from 150 to 1000 μm and tend not to undergo smooth fluidization, and bubbles form at the onset of fluidization. The minimum fluidization and minimum bubbling velocities are similar, this type of powders fluidize easily and are used in a wide range of fluidized unit operations with few difficulties [1], [11], [15]. Because of their ease of fluidization of Geldart Groups A and B, there is a lot of research and application for these two types of powders, [1], [2], [11].

Geldart Group C particles or Type-C powders are also known as fine powders or cohesive powders and are typically less than 30 μm . The particles that compose these powders are small and show noticeable cohesion and adhesion among themselves and with any surrounding surface, also the presence of static forces between the granules and the contact wall. Because of these characteristics, these types of powders are difficult to fluidize. Particles this small tend to behave more as particle clusters than single, independent particles. To properly achieve a fluidized state, Group C powders are usually fluidized with the aid of baffles, microjets, pulsing and/or mechanical vibration. In some cases, larger particles are added to the bed to promote smoother fluidization [11], [14]–[16], [46], [47].

Geldart Group D particles or Type-D powders, includes those containing large and very dense particles; the gas flow requirement for fluidization of these powders is very large, and solid mixing is relatively poor. During fluidization of this group, the bubbles formed are enormous and slugging can be observed [1], [11], [15].

2.1.14 Fluidization columns and reactors

Fluidized-bed processes have operated commercially since the 1920s, beginning with the advent of the Winkler coal gasifier in Germany [11]. A typical fluidized-bed reactor contains a plenum, a gas distributor, the particle bed region, a freeboard region above the particle bed, heating and cooling if needed, and cyclones. The grid plate and sparger are subject to pressure drop and spacing limits, the primary purpose is to provide good gas distribution. So, the design needs to consider pressure drop and spacing considerations, particle attrition, erosion of the vessel and internal components and mechanical constraints, like the external mechanical vibration used in this work [1], [8], [11], [44], [45].

Fluidized beds typically are more complex to design, build and operate than other types of reactors. Fluidized-beds are prone to erosion and particle attrition caused by the moving particles. Fluidized beds offer three distinct advantages over other process technologies: superior heat transfer, the ability to easily move solids like a fluid and the ability to process materials with a wide particle size distribution, and are also used as dryers and heat treaters [1], [11], [44].

The parts of a fluidized column are presented in Figure 10a. The parts can be described as the direction of the gas flux into the column. At the beginning, gas is passed through a gas distributor, or grid, which provides stable and even fluidization across the reactor's cross-section by creating a pressure drop. A plenum chamber is usually placed under the grid in order to distribute to pre-distribute the gas uniformly before it flows through the distributor. The solids placed above the grid constitute the bed whose level, also known as the bed height may vary based on the operating conditions of the reactor; such as gas velocity, gas properties and solid properties. The vertical space above the bed height is referred to by the freeboard and has the main task of preventing large amounts of bed material from being carried out of the reactor by the gas stream, which are represented in Figure 10a and b. [1], [8], [11], [45]

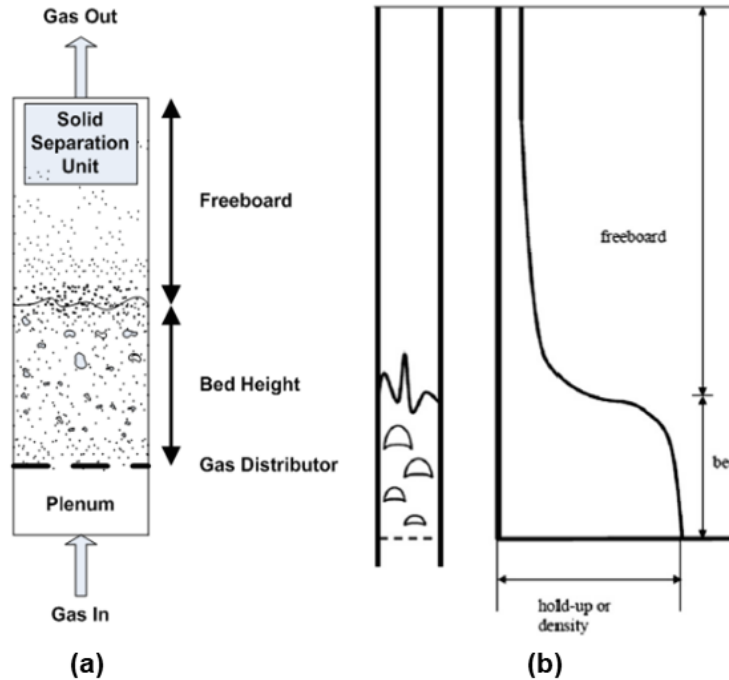


Figure 10. Fluidization column, (a) Fluid bed sections and (b) Freeboard and bed height schematic. Adapted from [45].

The plenum measures that are needed for a proper fluidization state, are summarized on Table 8, according to the gas entry of the reactor's configuration, which are vertically or horizontally [45]. For purposes of this work, a vertical gas entry configuration was selected.

Gas Entry	Conditions	Equation
Horizontal	$D_{\text{entry}} > D_{\text{plenum}}/100$	$H_{\text{plenum}} = 0.2 D_{\text{plenum}} + 0.5 D_{\text{entry}}$
	$D_{\text{entry}} < D_{\text{plenum}}/100$	$H_{\text{plenum}} = 18 D_{\text{entry}}$
Vertical	$D_{\text{entry}} > D_{\text{plenum}}/36$	$H_{\text{plenum}} = 3 (D_{\text{plenum}} - D_{\text{entry}})$
	$D_{\text{entry}} < D_{\text{plenum}}/36$	$H_{\text{plenum}} = 100 D_{\text{entry}}$

Table 8. Plenum measure requirements according to the gas entry configuration [45].

The pressure drop of the bed, equation (17), and the pressure drop of the orifice of the gas inlet component of the reactor, equation (18), can be determined by the equations above [11].

$$\Delta P = H_{Bed} \frac{g}{g_c} \rho_{bulk} \quad (17)$$

$$\Delta P_{orifice} \geq \frac{1}{3} H_{Bed} \frac{g}{g_c} \rho_{bulk} \quad (18)$$

Where H_{bed} is the height of the fluidized bed, ρ_{bulk} is the bulk density of the powder. For a fluidized state in the reactor, the ability of the powder to flow through it must be achieved. The container of the powder in the reactor, specially the one of this work, must consider the flowability of the powder through the reactor. The powder container must consider a conical hopper, for an appropriate flowability of the powder, funnel flow. As presented on Figure 11, the design of the powder component must consider an appropriate flow of mass, with a conical design, Figure 11a, and considering the hopper angle, Figure 11b, the proper flowability of the powder through the fluidized state in the reactor can be achieved [1], [9], [11].

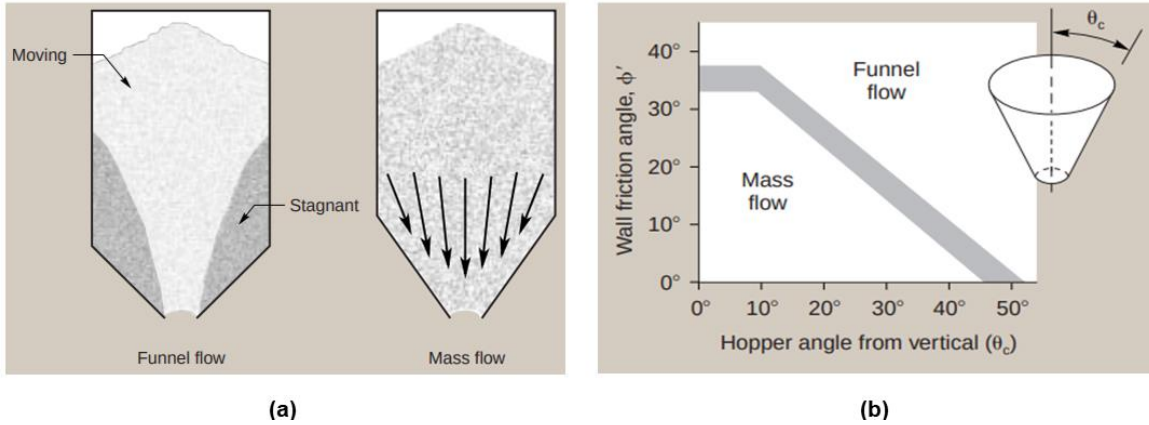


Figure 11. Powder flowability considerations for achieving the fluidized state. The flow movility of the powder (a), and the angle of the connical hopper for a proper mass flow (b). Picture adapted from [9].

Considering the movement of the gas through the powder and then the column, wall and internal friction must be considered. And for cohesive powders, static forces may appear, making the powder particles be attracted into the internal wall of the column. To avoid this problem, mechanical vibration into the external wall of the fluidized column can be consider, to prevent particles stay in the walls and fall down into the gas flux and powder container [1], [3], [9], [11], [48].

CHAPTER III CONCEPTUAL FRAMEWORK

3.1.1 Fluidization of cohesive particles

The particle size in type C powders is typically lower than 30 μm and they are very difficult to fluidize [15], [47], [48]. To achieve the fluidization state in this type of powders, the use of distributors, baffles, microjets, mechanical vibration, etc. is required [11], [15], [46], [49]. There are two methods for improving the fluidization of type C powders; one is by application of an external force, such as vibration, magnetic field and acoustic field; the other involves modification of intrinsic properties of the particles [10], [47], [50] or mixing with other particles with different size or shape [10], [47], [51].

According to the fluidization theory developed by Geldart and Abrahamsen [15], [16], [52], the relevant powder physical properties for this work are: the mean particle size d_p , the particle density ρ_p , powder bed voidage ϵ , the minimum fluidization velocity U_{mf} , the minimum bubbling velocity U_{mb} and the maximum non-bubbling bed expansion ratio H_{mb}/H_{mf} , the surface volume diameter, d_{sv} and volume diameter d_v . These physical properties are calculated as shown in equations (19) through (25), as presented in the work by Geldart and Abrahamsen [52]. To determine an average value for d , a CILAS 1064 particle size analyzer was used. To approximate ρ_p , the mass of compacted powder contained on a 10-mL volumetric flask was measured using an Ohaus Model Voyager Analytical Balance. To account for nonspherical particle shape, the values of the surface volume diameter, d_{sv} and volume diameter, d_v were calculated with the following equations:

$$d_{sv} = 0.871d_p \quad (19)$$

$$d_v = 1.127d_p \quad (20)$$

The sphericity of the powders was calculated with the equation (21).

$$\psi = \frac{d_{sv}}{d_v} \quad (21)$$

The bed voidage was calculated with the equation (22).

$$\epsilon = 1 - \frac{W}{\rho_p V} \quad (22)$$

where W is the total powder bed mass and V is the powder bed volume of the powder. The minimum bubbling velocity is given by the equation (23).

$$U_{mb} = 2.07 \exp(0.716F) \frac{d_p \rho_g^{0.06}}{\mu^{0.347}} \quad (23)$$

F represents the powder fraction with a size much lower than d_p , and it is obtained from the size distribution measurements in the particle size analyzer. Equation (24) is very useful for obtaining values of U_{mb} when using carrier gases other than air.

$$\frac{H_{mb}}{H_{mf}} = \frac{5.50 \exp(0.158F) \rho_g^{0.028} \mu^{0.115}}{d_p^{0.176} g^{0.205} (\rho_p - \rho_g)^{0.205}} \quad (24)$$

The minimum fluidization velocity was calculated using the equation (25), for particles with $d_p < 100 \mu\text{m}$.

$$U_{mf} = \frac{(\rho_p - \rho_g)^{0.934} g^{0.934} d_p^{1.8}}{1100 \mu^{0.87} \rho_g^{0.066}} \quad (25)$$

where ρ_g is the carrier gas density evaluated at the operating conditions, g is the gravity acceleration and μ is the gas viscosity.

3.1.2 Atmospheric plasma for surface modification

Plasmas have been used as an efficient tool for surface modification in a wide range of materials for many years. For the specific case of the atmospheric plasmas, many of these

surface modifications are performed on float objects [42], [53], [54] or even volumetric, macroscopic objects [35], [37], [55]. As mentioned before in this work, page 55, one of the most common methods for obtaining atmospheric pressure plasmas is the dielectric barrier discharge (DBD). In the nonequilibrium plasma processing, this method is accepted in the industry for handling large gas volumes. However, unlike vacuum operation which easily leads to a stable, uniform nonthermal plasma, it is difficult to obtain a plasma with these attributes at near atmospheric pressure [33], [34], [37], [40], [43]. There are essentially two methods of producing nonthermal plasmas: corona discharge (CD) and DBD. Even though, numerous applications rely on CD, this method is no convenient for volume gas-phase plasma processing. The DBD systems have several advantages, such as lower voltage consumption, current limitation to avoid transition to arc, a high-energy coupling of the DBD discharge and low level of UV radiation emission [40], [43], [56]

3.1.3 Fluidized-beds for surface modification of granular material with atmospheric plasma

Atmospheric plasmas can be used to treat macroscopic surfaces, by depositing thin films and/or altering the chemical composition of the surface. Micrometric surfaces in powders can also be modified using atmospheric plasmas. Reports in the literature have been focused on the treatment of granular material using a combination of plasma discharge and some type of powder fluidization. A circulating fluidized bed, which belongs to a fast fluidization regime, has been reported as a plasma reactor both for low-pressure [22], [26] and atmospheric plasmas [49], [57], [58].

Fluidized-beds provide low-temperature and low-pressure gradients at high gas velocity, and therefore cohesive powders can be dispersed favorably [49], [57], [58]. Plasma treatment of powder surfaces could change the macroscopic behavior in products that utilize these treated powders as ingredient or raw material, such as paints, food products,

pharmaceutical products, cement, concrete structures, tires and many other finished products [19], [22], [26], [49], [54], [57]–[59].

3.1.3.1 Surface Modification of Starches

There is a growing interest in developing and studying modified starches for many industrial applications as they could be used as a biodegradable alternative to synthetic polymers [22], [23], [26]. Several methods have been developed to produce modified starches with a variety of characteristics and applications. All of these techniques alter the starch polymer, making it highly flexible and changing its physicochemical properties and structural attributes to increase its value for food and non-food industries. The starch modification industry is constantly evolving. Modifications of starch include physical, chemical and enzymatic methods. Physical methods involve the use of heat and moisture, and chemical modifications introduce functional groups into the starch molecule using derivatization reactions. For purposes of this work, the chemical methods will not be presented, only one physical method: non-thermal physical modification [5], [21], [24], [59].

Physical modifications of starch can improve its water solubility and reduce the size of the starch granules. Physical methods to treat the native granules include different combinations of temperature, moisture, pressure, shear and irradiation. Physical modification of starch granules is cheap and safe. These techniques do not require chemical or biological agents, and are therefore preferred when the product is intended for human consumption. Some processes in food production are applied to extend the life of a product using thermic treatments at boiling temperatures (or even higher) for seconds or minutes. Traditional treatments cause a loss of some vitamins and nutrients and alter their organoleptic properties. Non-thermal modification is an alternative to traditional processes that also eliminates pathogenic microorganisms and spores. Non-thermal techniques involve the use of high pressure, ultrasound, microwaves and electric pulses. The high pressure technology in industry uses pressure from 400 to 900 MPa. High pressure

generally restricts the swelling capacity and consequently decreases paste viscosity. Other technologies use pressure several times below atmospheric pressure (vacuum pressures); this technology uses gas in a plasma state and is the most recent technology used for starch granule modification. For this treatment, the gases used include ethylene, hydrogen, oxygen, ammonia, air, methane or argon in a plasma state. This treatment modifies the starch in different ways, including its hygroscopicity, degree of polymerization and oxidation [5], [21], [24], [59].

3.1.3.2 Modified starches in industry

Starch is used in the food industry mainly as a modifier of texture, viscosity, adhesion, moisture retention, gel formation and films [21], [23], [53]. In the food industry, edible films are barriers that prevent moisture transfer, gas exchange, oxidation and the movement of solutes, while maintaining their organoleptic properties. During manufacturing, films are incorporated as plasticizers, flavors, colors, sweeteners, antioxidants and antimicrobials. Edible films have received much attention due to their advantages over synthetic films. Edible films are produced from renewable materials; they can be consumed together with coated food and otherwise do not contribute to pollution because their degradation is faster than synthetic films. Their main disadvantage lies in their mechanical and permeable properties. The basic materials used to produce edible films are cellulose, starch, gums and chitosan; the linear configuration of polymers can produce films with flexible, transparent and oil resistant properties. For these reasons, amylose is the most important fraction in starch granules. The starch used in edible film preparation is incorporated to partially or completely replace the plastic polymers. Native starch does not produce films with adequate mechanical properties and requires pretreatment. Plastics obtained from oil are being replaced by natural polymers; starch is known for its ability to form films in food packaging applications. The production of biodegradable plastics is still young when compared to the petrochemical plastic industry. Starch will play an important role in its growth in container production and in the form of biodegradable materials that conform to

suitable matrices because it is a relatively inexpensive material compared to other polymers. In the pharmaceutical industry, starch is used as an excipient, a type of bonding agent to active drugs. Because of its content of amylose, starch can form an inclusion complex with many food ingredients, such as essential oils, fatty acids and flavoring ingredients. It therefore acts as an encapsulant and increases the shelf life of products. In the textile industry, starch films are also used during textile production as fiber coatings. Native starch forms rigid and brittle films due to its cyclic structure. Brittle films are not advantageous because they reduce protection, increase friction, and thus damage the thread. The polarity of native starch minimizes the adhesion of synthetic fibers, affecting the tensile strength and abrasion. Starch is commonly modified to improve the physical properties, emulsifying ability and film formation. Several studies have concluded that is possible to produce a new generation of detergents in which the surfactants and bleaching components are derived entirely from starch. An estimated 50 to 60% of chemical products in formulations for powder detergents and 65 to 75% of liquid detergent formulations could be substituted with products derived from starch [5], [18], [21], [59], [60].

High viscosity is important in the adhesive field. Most native starches do not maintain a stable viscosity when transformed to pastes and or subjected to high shear velocity or longer heating periods. However, chemically modified starch behaves properly under these conditions. In recent years, starch has been studied to produce nanoelements as nanocrystals that result from the breakdown of the amorphous region in semi-crystalline starch granules by acid hydrolysis or to produce nanoparticles from gelatinized starch. These nano compounds have unique properties due to their nano size compared to conventional size materials. Nanoparticles can be used as fill material in filtration and form effective barriers in flexible packaging [17], [21], [25], [27], [59].

3.1.3.3 Surface Modification of TiO₂

The interest to modify the surface of the TiO₂ relies on the process behavior of the powder during the transport and discharge from bulk bags. And removing air significantly affects features of bulk solids and always impairs the flowability, this includes aeration, compressibility, angle of internal friction and permeability. Mechanical-physical features that impact on the behavior of the powder during the industrial processes, storage, transport or as a side effect in process manufacturing because of vibrations. There is a lack of information regarding the effect of atmospheric plasma surface modification in this powder. The growing interest in treating this powder by atmospheric plasma is due to its important applications such as conversion of toxic wastes to benign materials via photocatalytic oxidation or reduction reactions [9], [19], [20].

CHAPTER IV MATERIALS & METHODS

Design and Construction of the Reactor

For the construction of the reactor, some components were developed; and others were implemented from previous research projects such as the inner electrode and the RF source, as mentioned before, from the works of: Soto-Ruvalcaba [34], Figueroa-Hernández [33], Ruiz-Rico [37] and Arévalo-Torres [41].

The developed components were designed in SolidWorks and printed with a Cura 3D printer, in PLA and MLA material such as the inner electrode holders. As presented in Figure 12a, the components of the reactor, in the order in which are assembled, and in Figure 12b a diagram of the assembled reactor is presented. Other components were built from a nylon bar with the aid of a milling machine and lathe from the Prototype Laboratory, Figure 13, such as the input gas component, distributor base, powder container and the union component. The complete assembly and disassembly of the reactor is presented in Figure 14.

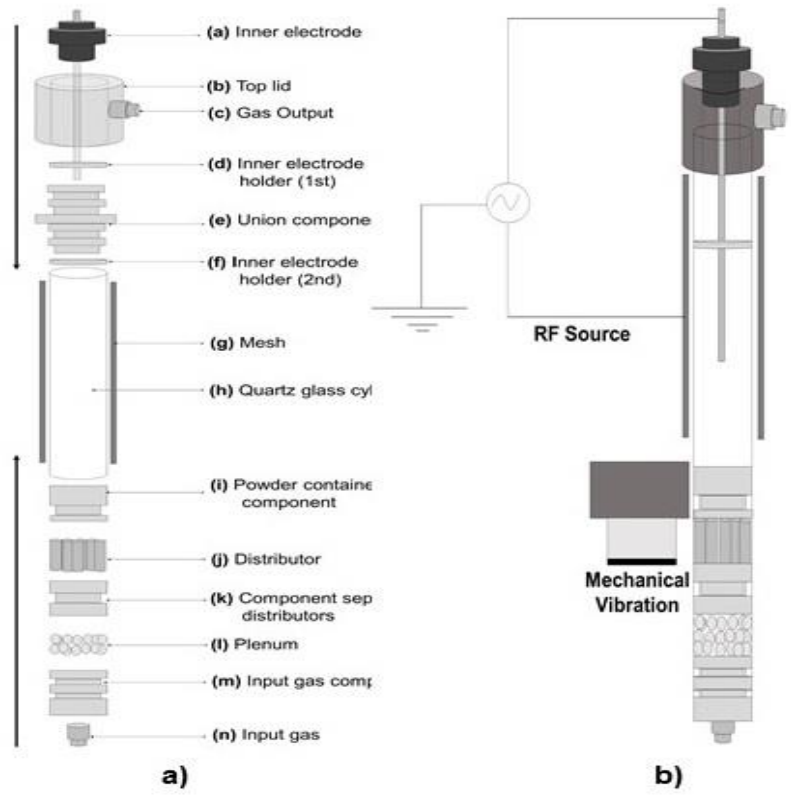


Figure 12. The Fluidized-bed Plasma Reactor built in the laboratory; in (a) the components are presented, in (b) a diagram for the assembled reactor.

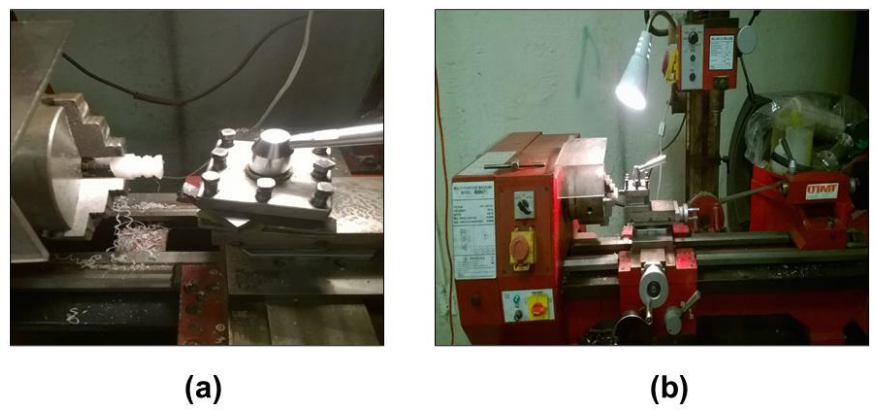


Figure 13. Photographs of the milling machine (a) and lathe machine (b), been used while the fabrication of the fluidization column in the Prototype Workshop of the Research Center.

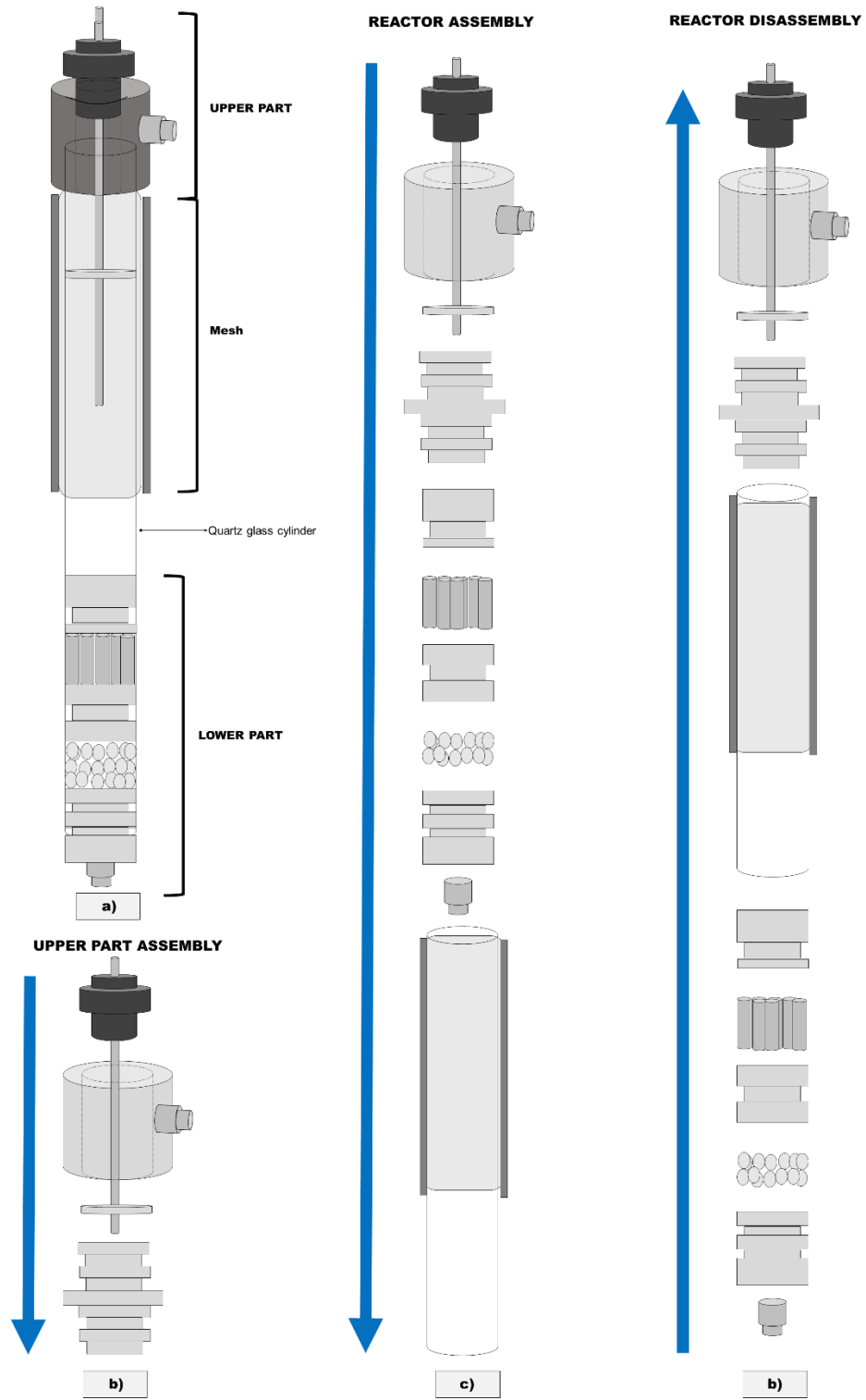


Figure 14. Complete diagram of the assembly and disassembly of the reactor

4.1.1 Testing Bench

For a proper operation procedure for the surface treatments in the laboratory, a test bench was built. Using Aluminum profiles (Standard Parker-profiles 40x40mm) as shown on Figure 15a. The measures of the profile are presented in Figure 15b and Figure 15c, [61].

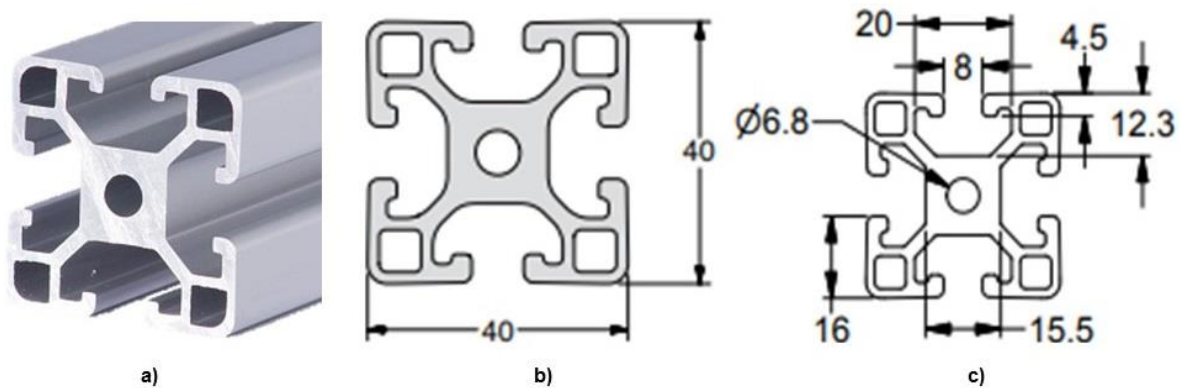


Figure 15. The standard Aluminum Parker-profiles of 40x40mm (a), the measures of the profile (b) and (c).

The canals of the profile structures, a and b on Figure 15, allows to set the reactor and its components in an orderly and well distributed position. With the aid of T-slot nuts the components are set to the bench. The rotameters used, were first fixed on an acrylic base, later this base was fixed on the test bench. Figure 16a presents the constructed testing bench and Figure 16b, presents the completed assemble of the DBD-Coaxial Reactors of the Research Center. In which the left side of Figure 16b, presents the COAX-FBPR and in the right, is the Jet-type Coaxial plasma reactor. The testing bench allows to keep both reactors for plasma surface modification in the research center.

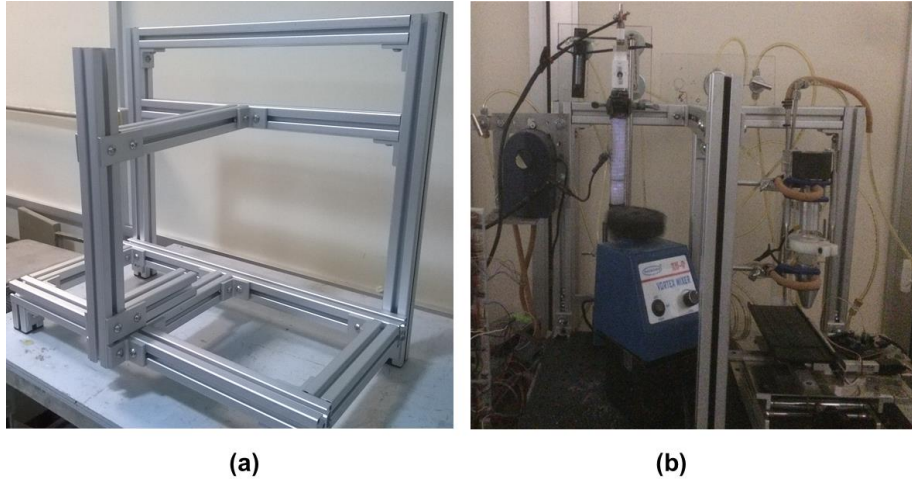


Figure 16. Photographs of the constructed testing bench (a), and the complete assembly of the COAX-FBPR and the Jet-type Coaxial reactor to the testing bench.

In Figure 17 the blueprints of the test bench are presented and in Figure 18 the arrangement of the components of the reactor are shown in a blueprint style. The final set-up of the test bench includes the COAX-DBD Jet type reactor and a CNC-type base, these for another type of configuration for surface treatment; nevertheless, it is only presented for the function of the bench, the Jet type reactor is used in the laboratory and will not be discussed in this work. The test bench offers a better operation of the treatments, due to the location of the valves and rotameters; an air pump was also installed to be used as for fluidization tests for powders before using the Argon gas for the treatments, Figure 18.

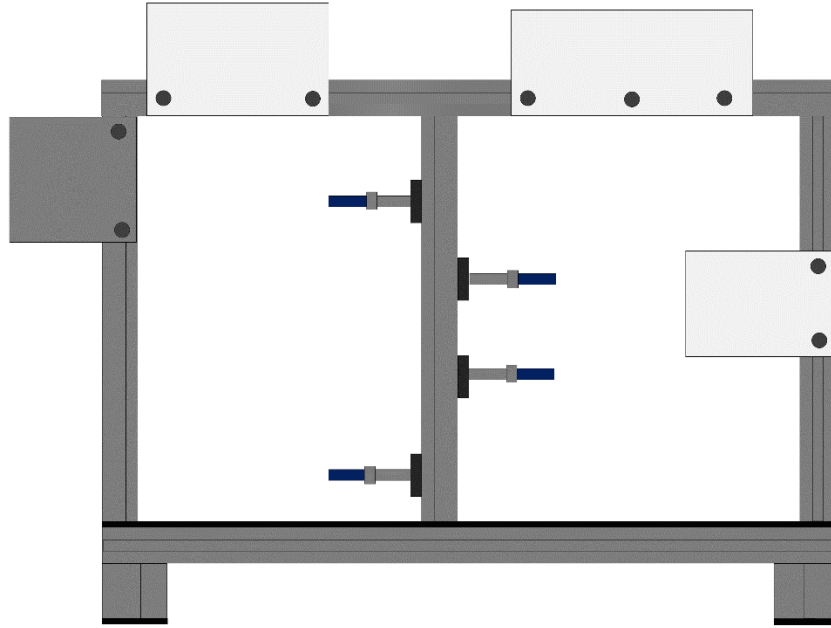


Figure 17. The test bench diagram.

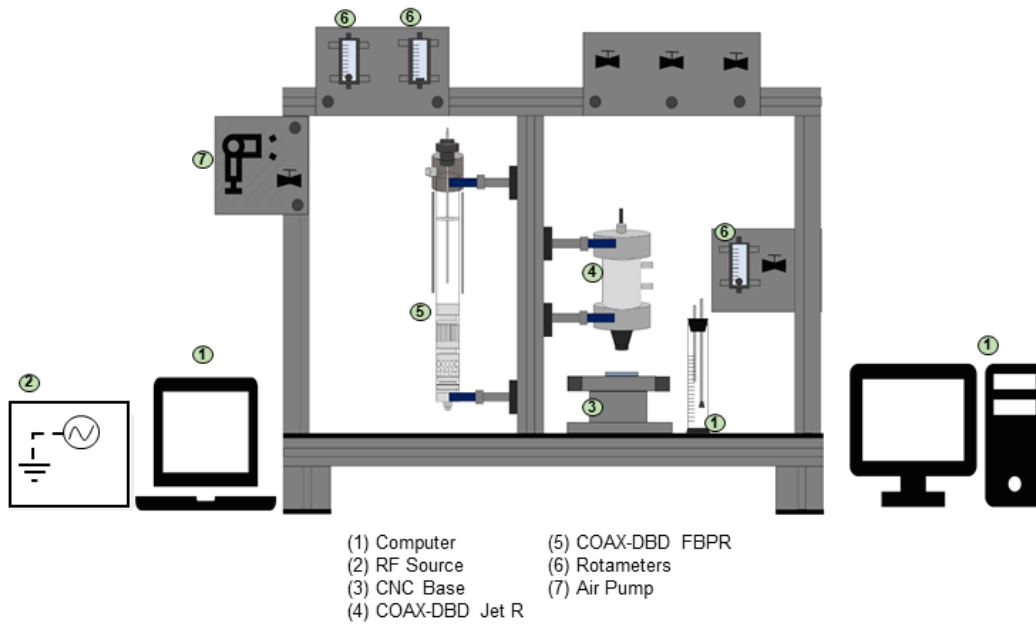


Figure 18. Components for the COAX-DBD FBPR on the test bench.

Materials

These elements are presented in this work and divided by two parts, that will be described in this section: Fluidization System Components and the and Generation Plasma System components, Figure 19.

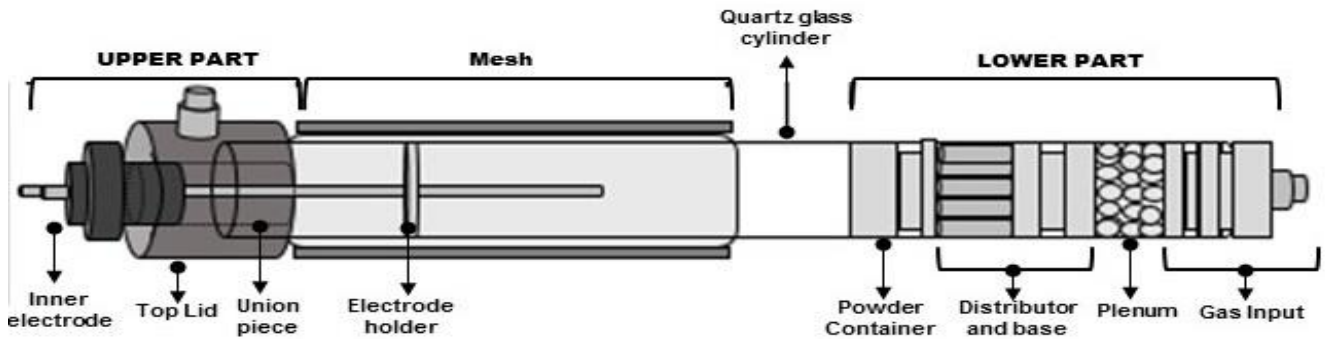


Figure 19. Diagram of the constructed fluidization column and its components.

4.1.2 Plasma Generation System Components

As mentioned on the previous section, for the plasma generation in the reactor, there were some elements needed. The central electrode, the dielectric shield or surface, the external electrode (been the mesh), the top lid and the radio frequency power supply system. The other inner pieces are related to the fluidization system, discuss in Section 4.1.3.

4.1.2.1 Inner Electrode

Isolated stainless-steel electrode of $\frac{1}{4}$ ", modified for aluminum electrodes and 6mm of diameter. Has a threaded NPT $\frac{1}{2}$ " connector, Figure 20. The use of this type of electrodes allows the risk reduction for the electrical arcs formation outside the gas ionization chamber.



Figure 20. Inner electrode used for the reactor.

This electrode had a previous treatment, to achieve the formation of a second dielectric layer in the plasma reactor; an electrolytic anodization cell was built for the anodization of the internal aluminum electrode, just as explained in the work of Figueroa Hernández A. M., 2010, [33]. The measurements of the inner electrode are presented in Figure 21.

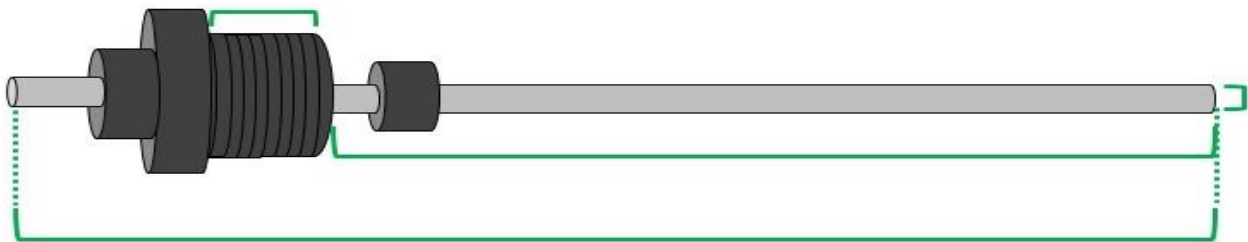


Figure 21. Measures of the inner electrode.

4.1.2.2 Inner electrode internal holder

The inner electrode is positioned in the center of the reactor. To assure the center position of the inner electrode, a component was designed in SolidWorks Figure 22, and printed in polymeric material. The function of this piece is to hold the inner electrode in the center of the reactor and with a space for the proper flux of gas through the reactor for the process.

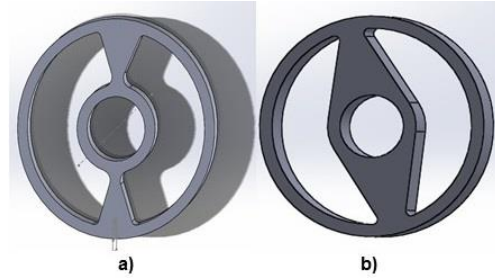


Figure 22. The inner holder design, both (a) and (b) were designed and built.

As seen in Figure 22, there are two versions of the component. The difference is the shape of the holder, but both models were used with no difference in the results. The measurements of the first model are presented in Figure 23.

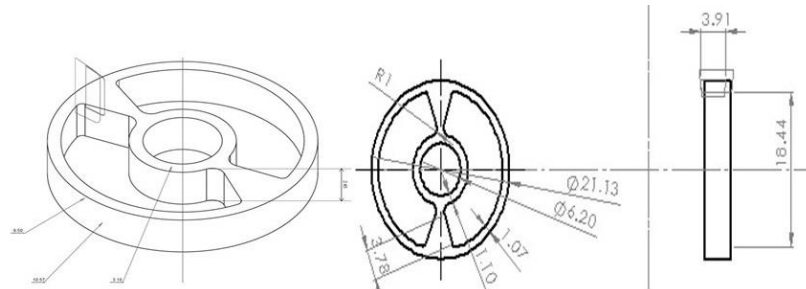


Figure 23. Measures of the inner electrode holder, first version Figure 22a.

The measurements of the second model are presented in Figure 24.

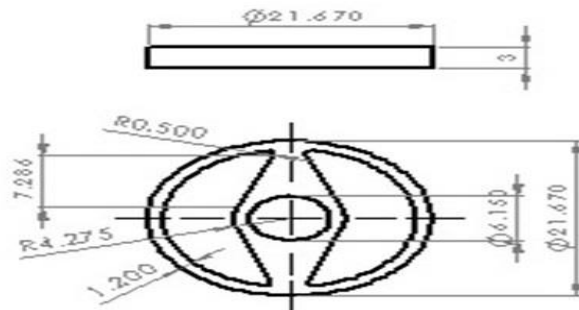


Figure 24. Measures of the inner electrode holder, second version Figure 22b.

4.1.2.3 Top Lid

As shown before, the inner electrode is positioned in the upper part of the reactor, Figure 12, where is located the output of the gas. The top lid of the reactor consists of a PVC coupling with an internal $\frac{1}{2}$ " thread connector, where the inner electrode is coiled, and in the exterior face of the piece, it was adapted for the output of the gas, Figure 25.



Figure 25. Photograph of the top lid component of the reactor.

The lower part of the top lid is attached to the reactor by another component, designed in SolidWorks. The material of the component is nylon and uses four o-rings Figure 26.

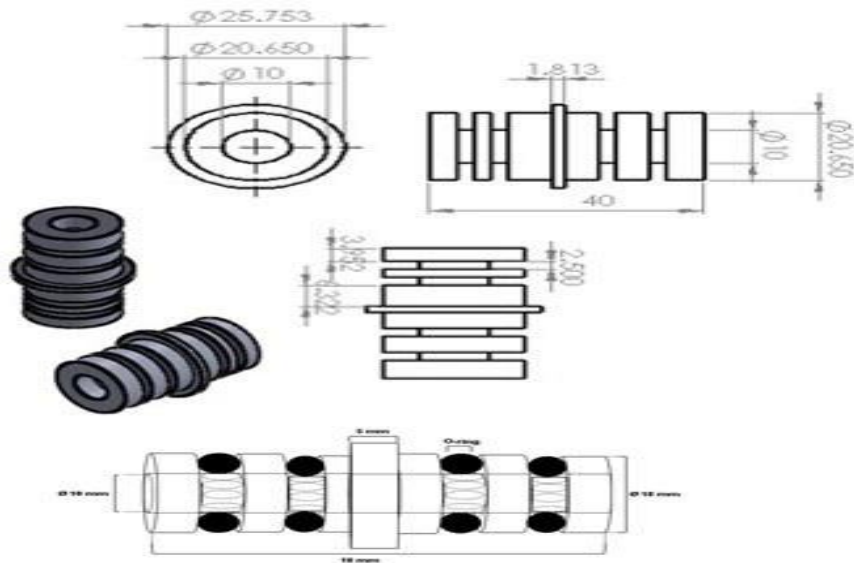


Figure 26. Design of the lower component of the top lid.

The final assembly of the upper part of the reactor consisting in the: inner electrode, the center piece for the electrode (2 components), the pvc top lid, and the nylomaq component that attaches the reactor with the upper part is shown in Figure 27. The blue arrow represents the direction of assembly.

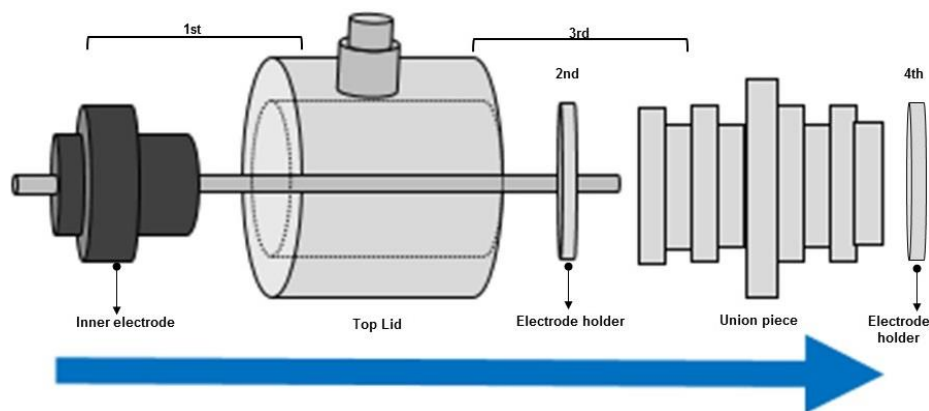


Figure 27. Assembly of the upper components of the reactor

4.1.2.4 Dielectric Surface

The dielectric surface is the main container, a cylindrical Quartz crystal of 27 cm of height and 22 mm of internal and 25 mm of external diameter, with a 1.5 mm wall, Figure 28. Quartz has a higher strength to withstand electric shock during several work cycles.



Figure 28. Photograph of the cylindrical Quartz crystal glass used as the dielectric surface of the reactor.

4.1.2.5 External Electrode

The external electrode is a fine stainless-steel wire mesh, Figure 29, wrapped over the external face of the reactor, surrounds the external face of the reactor been the dielectric surface and connected to a high voltage source by radio frequency (RF).



Figure 29. Photograph of the external electrode of the reactor, a stainless-steel wired mesh.

4.1.2.6 Radio Frequency Power Supply System

The RF power supply used in this project, was previously constructed and tested in the laboratory, as presented in the works of: Soto-Ruvalcaba L. [34], Figueroa-Hernández A.M. [33], Rico-Ruiz J. [37], Arévalo-Torres B., [41].

In Figure 30, an image of the RF power supply that feeds the COAX-DBD FBPR is presented. The power supply consists mainly of 5 modules that supply the high voltage requirement necessary to achieve the ionization of the gases contained in the reactor. This voltage is given in a pulsed form, in such a way that with the alternation of pulses it is possible to obtain a signal in a high-voltage sine shape. The power supply has the following characteristics: it has a radio frequency range to handle a variable frequency between 10 and 100 kHz, produces a sine wave amplitude between 0 and 10KVpp with a power up 3KW, current capacity maximum input up to 15. This source can provide a high voltage and high frequency.

The components of the RF source, as presented in Figure 30, are composed by: a frequency display (1 in Figure 30a), a black knob as a voltage modulator (2 in Figure 30a), an green led indicator for when the output of high voltage is on or off (3 in Figure 30a), a

stick button is the turn on and off output voltage (4 in Figure 30a), a frequency modulator (blue knob, 5 in Figure 30a) and an On/off button (6 in Figure 30a).

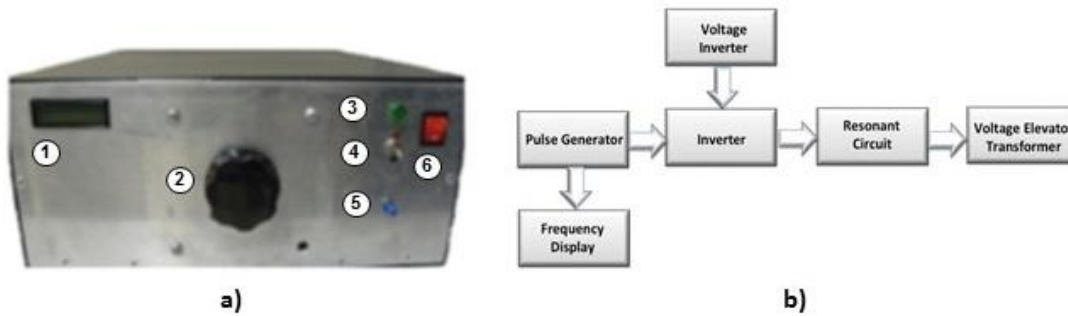


Figure 30. The Radio Frequency used for this project. (a) The source with the labels numbered 1 – 6 presenting the components. (b) Block diagram of operation.

The power supply circuit, Figure 31, allows the input voltage and current to be controlled at a resonance frequency, which is specific to the different gases fed into the reactor. By means of a manual frequency adjustment it is possible to achieve a gain in voltage and promote the resonance of the system for the generation of a luminescent discharge. The pulse module is responsible for generating two trains of pulses (sequence of pulses) alternately, which are conditioned to be introduced to the signal inverter in conjunction with the variable voltage. The power voltage variation generation module is responsible for providing a variable voltage of direct current to introduce it to the signal inverter, which allows obtaining a pulsed voltage that, when introduced to the resonant circuit, generates a pulsed high voltage signal, the latter being the one that is fed to the reactor at an RF frequency in the range of 10-100 kHz. In Figure 31, The electrical diagram of the circuit that provides the power supply to the reactor is shown and the characteristics of the RF source, are presented in Table 9, [33], [34], [41].

RF source Characteristics

Frequency Operation Range	19 – 55 [kHz]
Current	15 [A]
Voltage output	1.04 – 17.2 [kVpp]

Table 9. RF Source used in this work, for its operation.

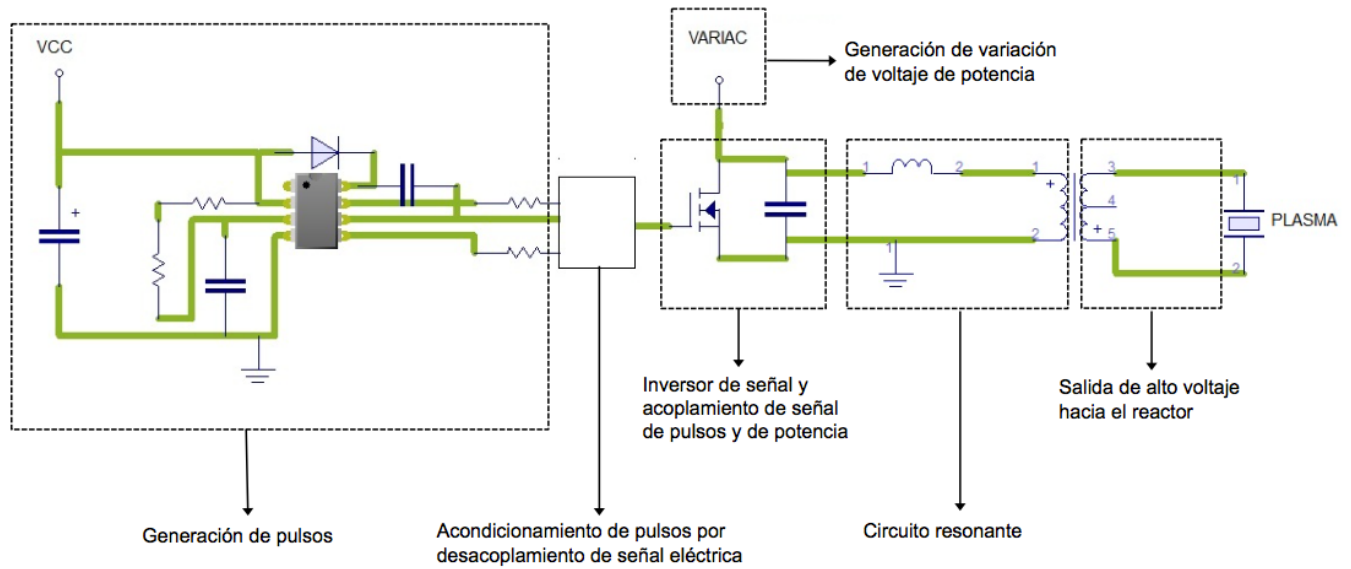


Figure 31. Electric circuit diagram of the power supply for the COAX-DBD FBPR, adapted from [41].

4.1.3 Fluidization System Components

The fluidization system, Figure 32, in the reactor consists by the following components, rotameters, the distributors: plenum, cylindrical distributors, and powder container piece with a conical face (upper face). Also, external vibration is added. As mentioned before, fluidization in fine powders is difficult, the aid of distributors is needed, for achieving the fluidized state, the distributors' description will be presented in the order in which the gas enters the reactor, in an upwards direction.

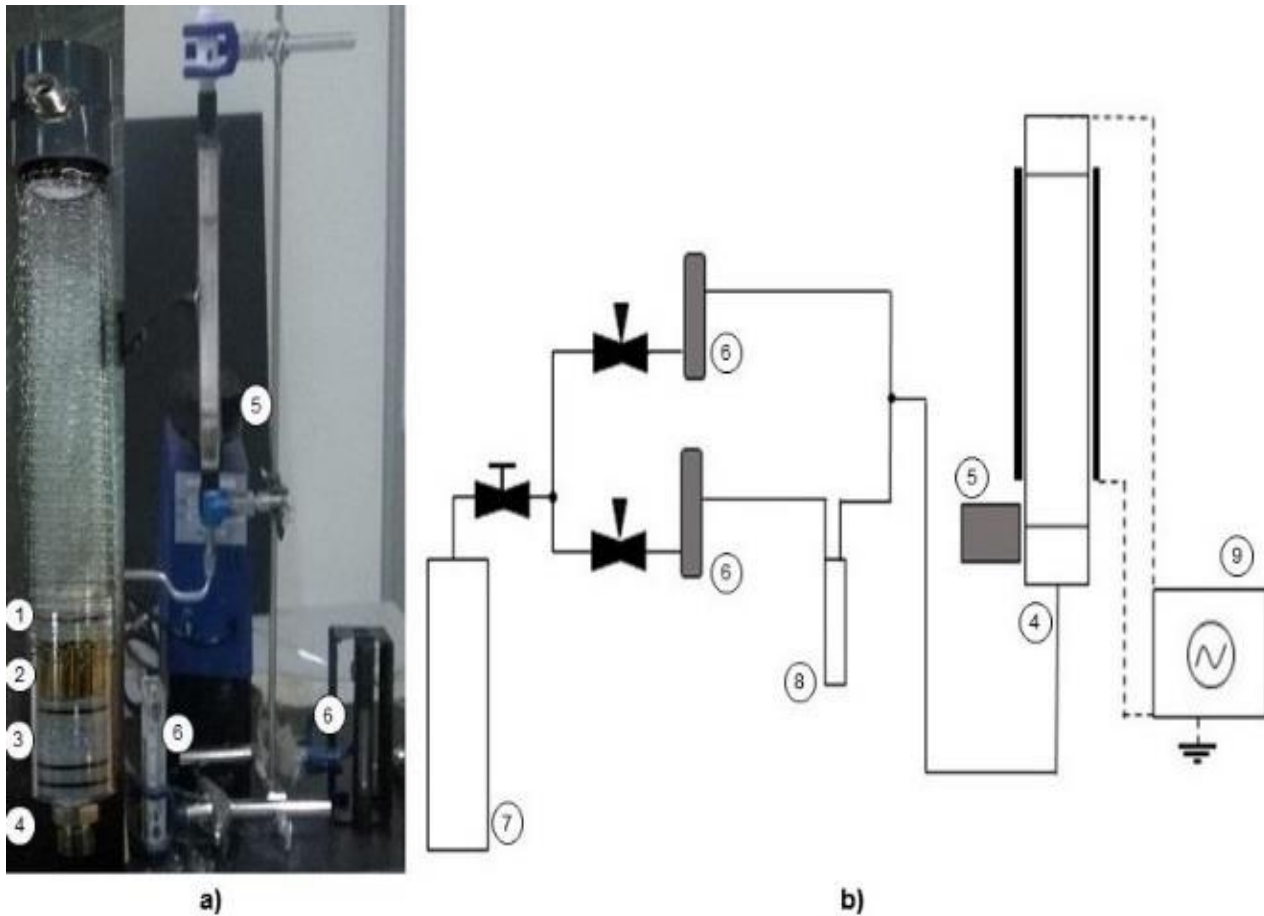


Figure 32. Fluidization system components, (a) powder container 1), distributor 2), 3) plenum, gas input 4), mechanical vibration 5), rotameters 6). (b) Conexion diagram of the fluidization and plasma generation systems, 7) gas container, 8) , 9) RF-source.

4.1.3.1 Rotameters

For reasons of this work, two variable area flowmeters, also known as rotameters, were used Figure 33. Photographs of the rotameters used for this project. a) 2-20 SCFH, B) 0-10 SCFH. They are easy to install with low pressure drop and without electrical connections that also provides a direct reading of the flow rate for a wide range of liquids and gases (Gas rotameters were used). A rotameter consists of a narrow vertical conical transparent tube made of glass or plastic with a float inside that is free to move; as the fluid flows through the narrow tube, the float rises within the tube to a position where the weight of the float, the drag force and the floating force are mutually balanced and the net force acting on the float is zero; the flow rate is determined by simply matching the position of the float against the graduated flow scale on the outside of the narrow tube, with the label 6. One rotameter measure from 3 to 20 SCFH, Figure 33a, and the second measures from 0 to 3 SCFH Figure 33b. This last one is connected to the test tube, in which a monomer is placed.

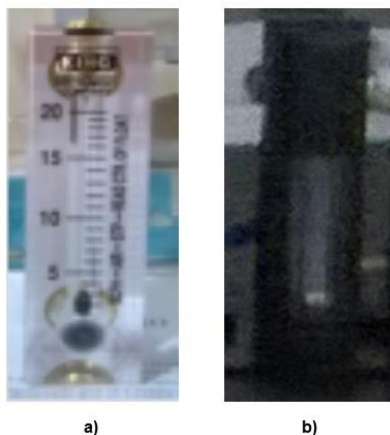


Figure 33. Photographs of the rotameters used for this project. a) 2-20 SCFH, B) 0-10 SCFH.

4.1.3.2 Input gas component

Input gas component was designed in SolidWorks and created from working a nylon 6/6 bar in a milling machine from the laboratory of prototypes of the research center.

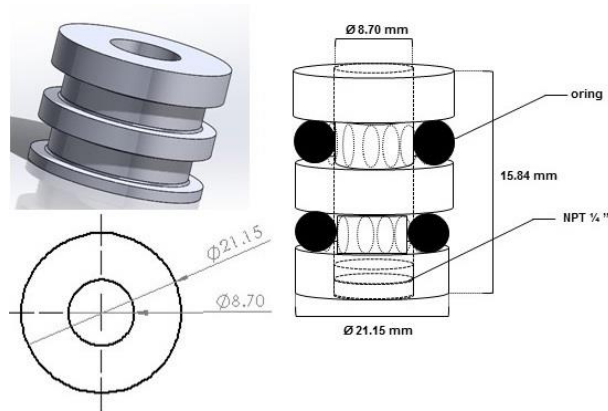


Figure 34. Diagram and measures of the component that joints the upper part of the reactor with the crystal quartz cylinder.

As presented on Figure 34. Diagram and measures of the component that joints the upper part of the reactor with the crystal quartz cylinder., the lower part of the component has a $\frac{1}{4}$ " connector and uses two o-rings for sealing the entrance of the reactor.

4.1.3.3 Plenum

The plenum is the first part of the fluidization process in the reactor. For this project, the plenum consists of: 3mm sodium-calcium glass beads Figure 35.



Figure 35. Photograph of the plenum of the reactor.

4.1.3.4 Distributor: Hollow Hexagonal-prisms

The purpose of the distributors is to provide good gas distribution. For this distributor, as shown on Figure 36a, base was needed following this base, the distributor consists of hollow hexagonal prisms of 10.4 mm^2 of area and 25 mm of length, as shown on Figure 36b.

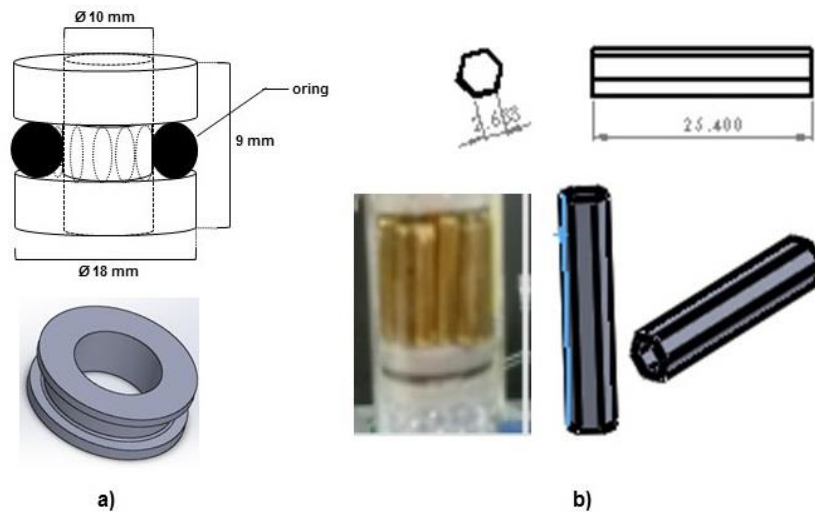


Figure 36. Design and measures of the Component that holds the plenum (a) and the fist distributor

4.1.3.5 Powder Container Component

As mentioned on the previous section, cohesive powders tend to agglomerate, and for this project, the powder container component was designed, as a conical hopper [9], to have an inclination in the upper face, a conical face, Figure 37a. This inclination allows the powder granules to fall again through the channel were the gas flux when entering, Figure 37b. This design is used for powder flowability, allowing funnel flow in the process [9].

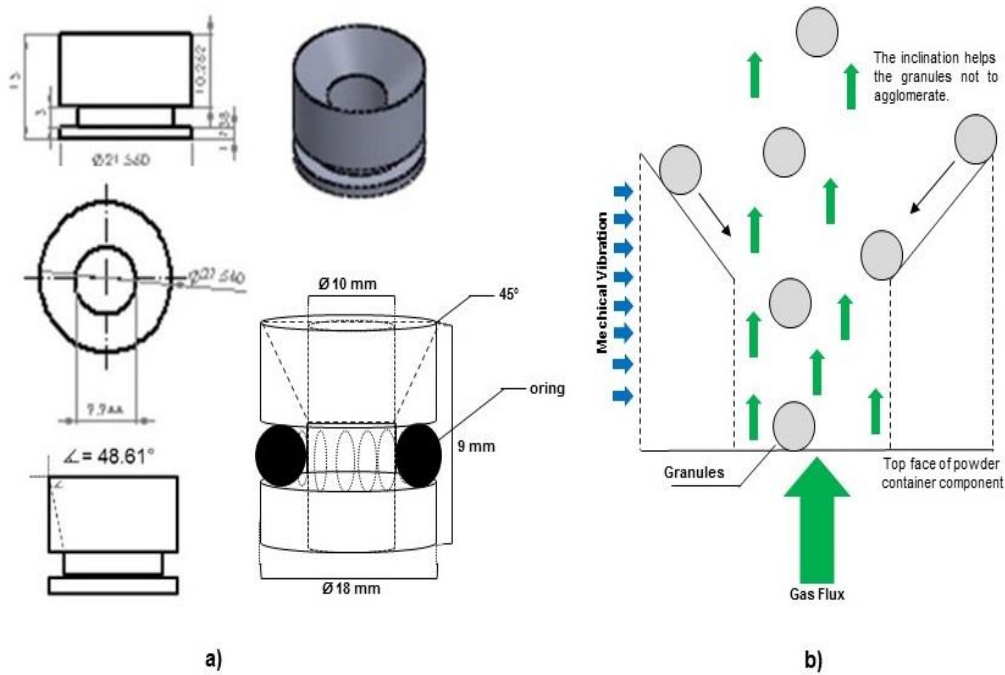


Figure 37. Design and measures of the powder container component (a), and the diagram explaining the operation and advantages of the component (b).

For obtaining an appropriate funnel flow in the component, the wall friction angle of the component has a value of 48.61° , which is less than 50° , the maximum limit for a proper balance between the mass and funnel flow, [9].

Selected Powders

For this work, and to test the developed COAX-DBD reactor, two powders were selected as test powders, one organic, potato starch (PS) and one inorganic, titanium dioxide (TiO₂). Both powders were subjected to atmospheric plasma treatments using different monomers, (Table 10).

The organic powder used in this work was obtained from the National starch (San Juan del Río, Querétaro. México) and is composed of 25% amylose and 75% amylopectin, and it is classified as a type A powder. To evaluate the effect of plasma treatment on the PS properties, calorimetric and rheological tests were performed using a differential scanning calorimetry (DSC)1 Mettler Toledo Calorimeter and an Anton Physica MCR 101 Rheometer, respectively. The titanium dioxide (TiO₂) used for this work, has 0.007M purity and it was obtained from Sigma Aldrich. This material falls in the type C category of the Geldart classification of powders. Since the natural TiO₂ has a very broad particle size distribution, it added complexity to the preliminary test for sedimentation properties, the particle size distribution was narrowed by passing first the powder through a 500 µm sieve, followed by a 5-min separation process of gas flow to blow away very fine particles, using the fluidized column of the COAX-DBD reactor. After this process, size distribution was measured in a CILAS 1064 particle size analyzer.

Plasma surface modification with the COAX-DBD PFBR

The granular material was treated in the small-scale coaxial DBD reactor (COAX-DBD PFBR) designed and built in our laboratory for this purpose and operating it in the experimental loop Figure 38. The operational process of the COAX-DBD, is as follows: it operates as a batch fluidized-bed reactor to allow contact between the atmospheric plasma discharge and the granular material in a fluidized state without allowing any interaction or alteration from the environment to the sample of granular material, [62].

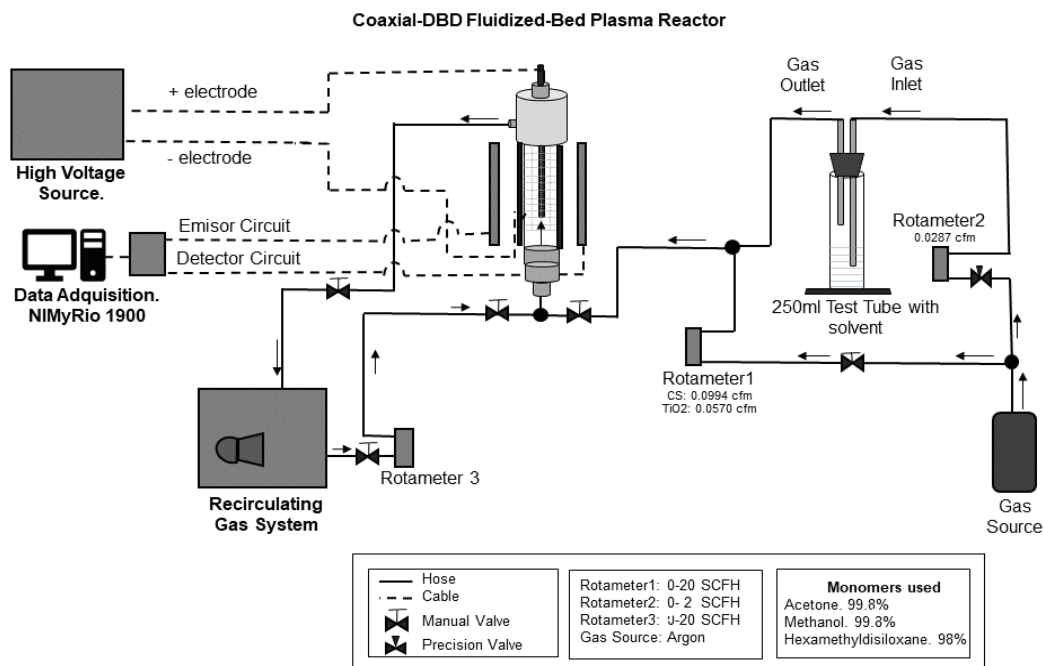


Figure 38. Operation and diagram of connectors of the COAX-DBD Plasma reactor, [62].

The operational process of the developed COAXDBD reactor, is presented as a flux circuit diagram, Figure 38, for a proper analysis. From the gas source, Argon gas is introduced into the flux system. Then the Argon is separated into 2 pads, the first one goes into a test tube with solvent, so it can mix with the Argon gas, then both fluxes combined and enter the reactor. The reactor was designed a COAXDBD configuration, this means, that the reactor consists of two coaxial electrodes separated by a quartz tube that serves both as reactor container and as dielectric barrier (b) between the electrodes, as shown in Figure 39. The internal anode electrode (a'' in Figure 39) is located at the center of the reactor and is fed with an alternating high voltage, while the cathode, constructed with a mesh (a' in Figure 39) around the quartz tube, is always grounded. When gas enters the interelectrode region (c in Figure 39), a filamentary atmospheric discharge is obtained in the space between the central bar electrode and the quartz tube, interacting with the fluidized granular material. Resulting into the surface modification of powders with atmospheric plasma, [62].

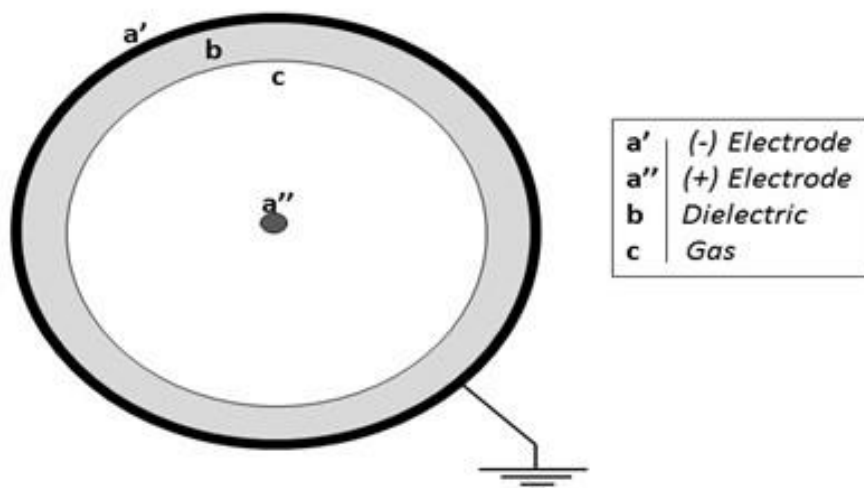


Figure 39. Diagram of the coaxial dielectric barrier discharge configuration, [62].

To obtain current flow in the discharge gap, the intensity of the electric field must be enough to achieve the breakdown of the gas for achieving the plasma state [33], [34], [40], [43]. In the plasma generation system of the reactor, has two main circuits: the power circuit, which includes the RF generator with a resonant circuit [33], [34], [37], and the gas handling circuit, which comprised the reactor and a system for gas delivery and recirculation, [62].

The gas distribution system is divided in two sections: the first one, is the entrance of the gas directly into the reactor, and the second section is for mixing the gas into a solvent, this is by going into a bubbler containing a liquid solvent column and then entering the reactor. The solvents used were Acetone and Hexamethyldisiloxane for both powders and Methanol for the potato starch and Isopropanol for the Titanium Dioxide, [62].

As presented on Table 10. This method on the procedure is necessary to successfully modify the surface with small amounts of organic vapor introduced in the reactor along with the inert gas carrier (argon), since molecular fragments and radicals are formed in the plasma discharge from solvent molecules encourage the surface modification of the granular material. A portion of the carrier gas is diverted to be bubbled through a column of the solvent to be used as the “active ingredient” during the plasma discharge. To

calculate the amount of solvent injected into the plasma reactor, it is assumed that the argon bubbles saturate with solvent vapor at ambient temperature.

The coaxial configuration was chosen for a proper dielectric discharge and to ensure that the treated samples would not interact with the environment, and it is a promising solution for treating powders with an atmospheric pressure plasma when combined with a fluidized-bed, due to the non-contact of the powder sample with the environment and the tester. The powders when fluidized, are constantly exposed to the plasma and the other particles stay in the interior walls of the reactor due to electrostatic forces produced by the friction between the fluidization and the walls. Because of this, a mechanic vibration is needed to reduce the amount of granules in the interior walls. Either way, the powders will fall and fluidized. During the process, the powders are exposed to the plasma. The reactor that consists of a COAXDBD configuration combined with batch fluidization of particles [38], [51], [57], [58] is named here a plasma fluidized-bed reactor (PFBR). The main advantages of this type of reactor are a well-mixed material, good temperature control, and a close contact of solids with the active atmospheric plasma in a fluidized-bed [38], [49], [51], [57], [62].

The experimental procedure presented in this work, can be described as follows: a mass of the sample (selected powder) was loaded in the PFBR powder holder; then, the mixture between the inert gas carrier (argon) with the solvent vapor with argon, was injected into the bottom of the reactor, until reaching the flow rate necessary for an adequate fluidization state of the powder bed, known as the fluidization column of the PFBR. At this point, the RF power was adjusted to start the discharge for 10 min at a voltage level of 12 kVpp and a frequency of 25 kHz; finally, the powders were extracted from the reactor, [62].

The particle loss due to particle drag was 32.04 and 43.82% for the potato starch and titanium dioxide powders, respectively. For the titanium dioxide, the particle separation process prior the treatment was considered to calculate the loss rate.

In Table 10, the operation values for the treatments and the solvent species used in each type of selected powder, are presented. In which, the vapor pressure of the solvent at room

temperature, the percent of flow diverted to the bubbler and the total flow of Ar into the reactor are included in Table 10. Volumetric mass flow is important to determine the velocity, U , used for the powders to achieve fluidization. Pressure is important due to the capability of the reactor to handle different powder sizes and solvent types.

Powder	ID	Solvent	Vapor pressure (kPa)	Flux into bubbler (cm³/s)	Total flux (cm³/s)
	1	<i>Acetone</i>	31.1	0.705	2.77
Potato starch	2	<i>HMDSO</i>	5.35	0.121	2.82
	3	<i>Methanol</i>	17.4	0.395	3.04
	1	<i>Acetone</i>	31.1	0.132	1.22
Titanium dioxide	2	<i>HMDSO</i>	5.35	0.023	1.11
	4	<i>Isopropanol</i>	17.4	0.3	1.39

Table 10. Operation values used for the treatments and the solvent species used in each powder, [62].

Preliminary Optical System

A preliminary prototype for light scattering of fine particles was constructed. The function is to present a preliminary test for fluidization process with and without the presence of the DBD-discharge. The assessment of the prototype will be the main objective for another research project. For purposes of this work, the prototype was only tested.

As shown on Figure 40, the prototype consists of two plates; one with 16 emissors (LEDs) and the other one with 16 receptors (photodetectors). Ordered in a row and in front of each

other. In Figure 40a, the measures and distances between the sensors is presented, Figure 40 b, is a schematic arrangement with the reactor and in Figure 40 c, a photograph of the optical system in operation is presented.

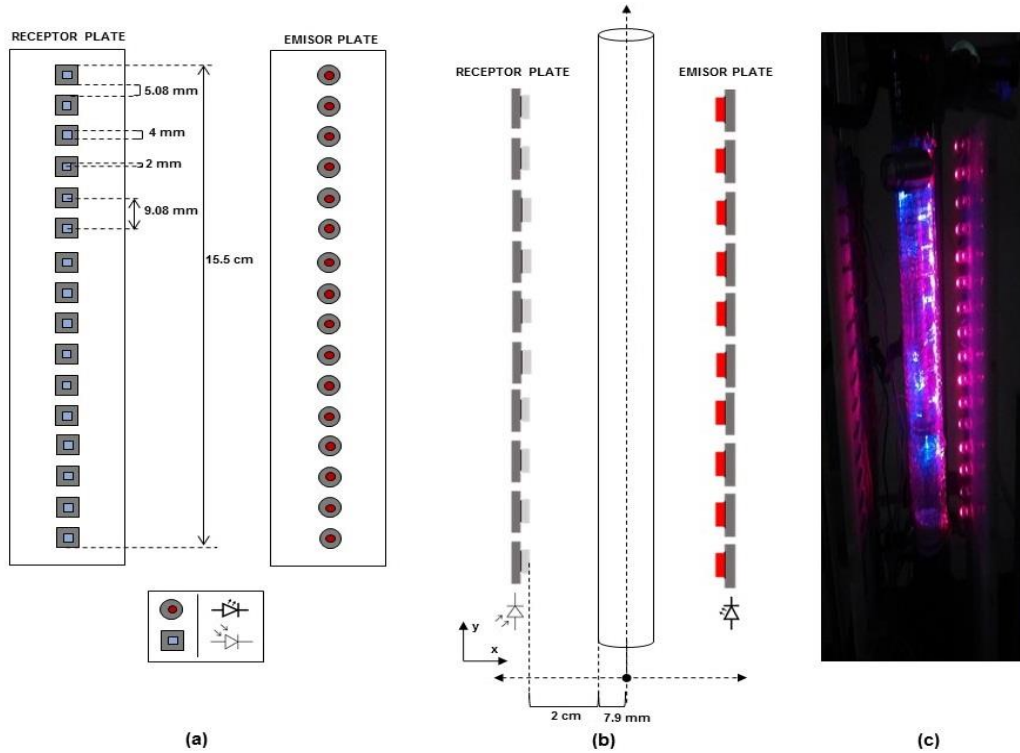


Figure 40. Light scattering for particle characterization prototype. (a) Design, showing 16 photodetectors and 16 emmitters. (b) Distance between the reactor and the plates. (c) The prototype operating in the presence of a discharge.

The arrangement consists of sixteen pairs of one emissor and one receptor, S_n in Figure 40a. And presented in groups of four pairs, Groups 1-4, from top, S_0 , to bottom, S_{15} as shown in Figure 41. Arrangement used in the research work, for the light scattering prototype.

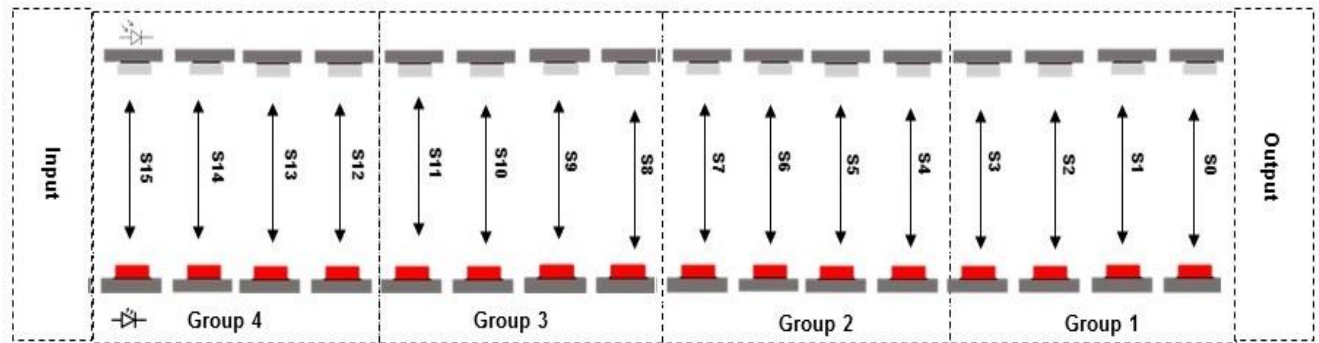


Figure 41. Arrangement used in the research work, for the light scattering prototype.

In Figure 42a is presented a diagram of the measures of the space between the radius of the Quartz glass cylinder (dielectric surface) and the inner electrode. In Figure 42b, the arrangement of the emissor and detector plates are presented.

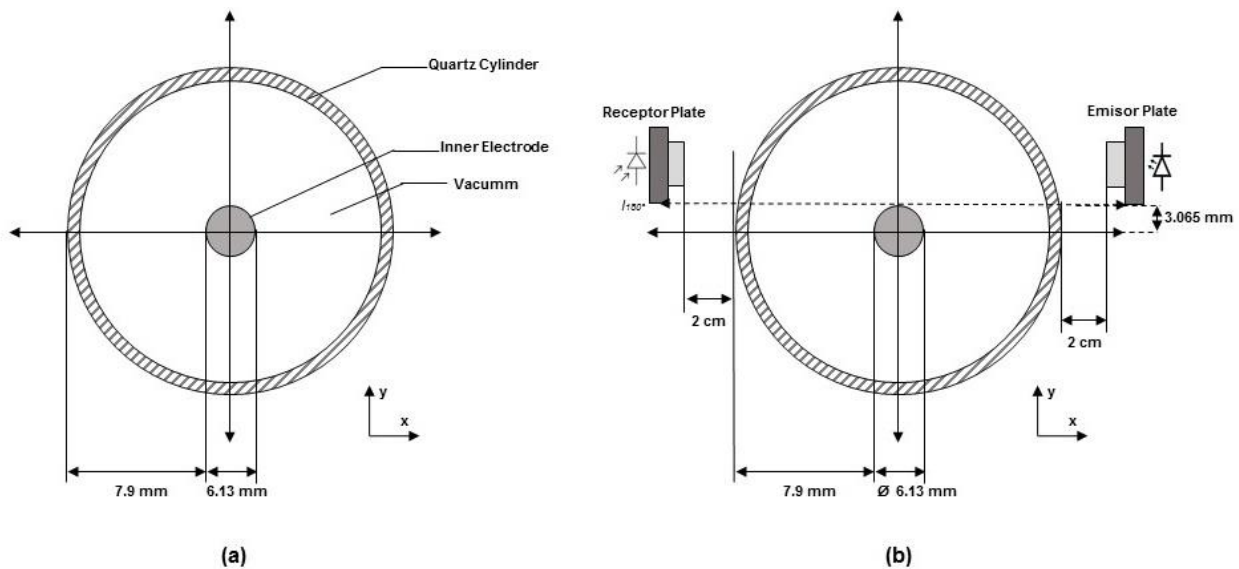


Figure 42. (a) Diagram of the measures of the space between the radius of the Quartz glass cylinder (dielectric surface) and the inner electrode. (b) The arrangement of the emissor and detector plates are presented.

Particle Characterization Techniques

To evaluate and determine the effect of the plasma surface modification on the potato starch properties, calorimetric and rheological tests were performed. The instruments used for these tests were a DSC1 Mettler Toledo calorimeter for the calorimetric test and an Anton Physica MCR 101 rheometer for the rheological test.

The titanium dioxide was submitted to a particle size distribution measurement in a CILAS 1064 particle size analyzer. Before performing the measurement on the sample, the particle size distribution was narrowed passing the powder through a 500 μ m sieve, followed by a 5-min separation process using gas flow to blow away very fine particles. This is because of the original titanium dioxide has a very broad particle size distribution, that added complexity to the preliminary sedimentation measurement performed in this work.

A scanning electron microscopy, Phenompro Generation 5 PhenomWorld, was utilized to determine size, shape and size distribution of the untreated powders, titanium dioxide and potato starch, used in this work, as a complementary experimental technique. Completely dried samples were deposited on a sample holder with electrically conductive carbon double-sided tape. The samples were observed at 5 and 10 KV.

4.1.4 Granulometry

The particle size distribution was measured in triplicate using a granulometer (Cilas 1640, Mar-Coussis, France) based on light scattering. The operational principle of this instrument is to illuminate the region where the particles are suspended with a laser beam, and a photodetector array provides the angular dependence of the scattered light [26]. These scattered patterns can be reproduced into particle size distributions using different models. For potato starch, the average shape of the granules has an approximate spherical shape, the Mie theory was applied as a first approximation. When the granules are not as spherical as titanium dioxide, the results should be interpreted through effective diameters that depend on the details of the geometry of the particles [27].

The CILAS 1064 particle size analyzer was used to determine an average value for d . For an approximately value of ρ_p , using an Ohaus Model Voyager analytical balance, the mass of a compacted powder contained on a 10-ml volumetric flask was measured. Taking in consideration the non-spherical particle shape, the values of the surface volume diameter, d_{sv} , and volume diameter d_v , were calculated using the equations (19) and (20) respectively. The powder physical properties, used for this work, were calculated from equations (21) through (25), as presented in the previous section. These physical properties are the mean particle size d_p , the particle density ρ_p , powder bed voidage ϵ , the minimum fluidization velocity U_{mf} , the minimum bubbling velocity U_{mb} and the maximum non-bubbling bed expansion ratio H_{mb}/H_{mf} , the surface volume diameter, d_{sv} and volume diameter d_v .

4.1.5 Calorimetry

Using a differential scanning calorimeter (Model 822E, Mettler-Toledo) calibrated with indium, the thermal properties of the starch gelatinization process were measured. For this work, the starch gelatinization was calculated by using the following method [30]: 2 mg of dry basis starch sample was weighed in a 40 μ L aluminum pan and 7 μ L of deionized water were added to the powder. The pan was hermetically sealed and allowed to stand for 1 h before analysis. As a reference, an empty aluminum pan was used. The sample was heated from 30 to 110°C at 10 °C/min. The starting gelatinization temperature (T_0), the peak temperature (T_p), the final gelatinization temperature (T_c) and the gelatinization enthalpy change (ΔH) were computed using the calorimeter's built-in software.

4.1.6 Rheometry

The characteristics of the rheometer used for this worked are as follows, an Anton Paar, Physica MCR 101 with two parallel 25 mm diameter circular plates (upper plate-sandblasted), separated by a 1000 μ m gap. And was used by rotational test, to measure

the pasting profile of starch dispersions at 5% solids content. A heating or cooling rate of 5 °C/min and a shear rate of 50 s⁻¹ were used. To avoid water evaporation during the test, the edge of the parallel plates was completely covered with mineral oil. The rheometer was programmed for running time sweeps of the heating cycles from 25 to 90 °C, holding for 5 min, cooling to 25 °C and maintaining for 5 min before applying three measurement cycles. The first cycle up going from 0.01 to 100 s⁻¹ and the second and third cycles going from 100 to 0.01 s⁻¹. Since starch is a non-Newtonian fluid, the shear stress as a function of velocity is assumed to follow the Ostwald-de Waele equation:

$$\tau_{xy} = K \left(\frac{\partial u_x}{\partial y} \right)^n \quad (26)$$

From the rheometer experimental data, performed in triplicate, values for the consistency index K (Pa·sn) and the flow behavior index n (dimensionless) can be obtained. The results from these calculations were used to define the flow behavior [28], [29].

CHAPTER V RESULTS & DISCUSSION

Final reactor design and process description

As mentioned before, part of the results presented and discussed in this section, were presented in a research paper, [62], and it is included in this work in the appendix 6: Research Products section.

The constructed COAX-DBD PFBR, will be described by following the path of the gas flux through the different components of the reactor, starting from the plenum chamber, n through j in Figure 43.

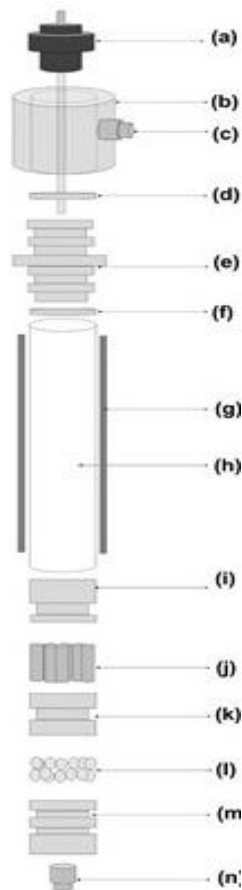


Figure 43. Components of the constructed COAX-DBD PFBR

The purpose of this section is to pre-distribute the gas uniformly before it passes the powder holder component, “l” in Figure 43, [11], [44], [45]. For this work and because of the type of material sample used, a vertical gas entry was selected [45]. Following the flux of the gas, continues the quartz cylinder, the mesh, and the exit of the gas, “h”, “g” and “c” in Figure 43 respectively. The upper part of the reactor is conformed by the inner electrode and its holders, “a”, “d” and “f” in Figure 43, respectively.

Fluidization properties of the powders

Based on the fluidization theory, previously described , (Chapter II, State of the art - section Fluidization), and for purposes of this work, some of the powder properties that are relevant to establish the type of fluidization regime and to determine flow velocity ranges, are summarized and presented on Table 11. These parameters are important for the initial fluidization process, this is to stablish the presence of a fluidize state of the powder. It is important to mention that preliminary fluidization tests are qualitative, the results are obtained only by visual observations [1], [15], [46], [47], that is, measuring the flow of gas entering the reactor and observing the behavior of the powder, and measuring the amount of mass loss from the fluidization column during this preliminary test.

Property	Potato Starch	Titanium Dioxide
dp,(μm)	44.05	3
dv, (μm)	49.64	3.4
dsv, (μm)	38.37	2.61
Ψ, -	0.77	0.77
$\rho\rho$, (kg/m³)	967.44	831.9
ϵ, -	0.1115	0.3112
dp,(μm)	44.05	3
Particle Loss	32.04%	43.82%

Table 11. Physical properties of the powders, [62].

For determining if the fluidization powder behavior was possible, d_p was determined for both powders, to take in consideration the proper parameters so the reactor could be adjusted. Also, for both powders, the properties d_v and d_{sv} were calculated to obtain the ratio d_v/d_{sv} , giving the particle sphericity ψ . As presented in Table 11, both powders have a value of 0.77 for the sphericity, which corresponds to a rectangular parallelepiped shape. According to this information, two concepts are considered in this work for both powders: the ideal sphere shape model to obtain fluidization conditions is discarded, and the calculations were done for the case of non-spherical particles.

For the two powders used in this work, the fluidization properties for the experiments are presented in Table 12. This information was measured as follows: the gas velocity U is determined experimentally by measuring the volumetric flow rate into the reactor and dividing by the cross-sectional area of the powdered bed. The minimum bubbling velocity U_{mb} is the value that determines where bubbles first appear and is determined using Eq. (6). On the other hand, the minimum fluidization velocity, U_{mf} , is the minimum velocity the particles need to break the resting starting position and is calculated using Eq. (7) with the values from Table 11.

Powder	Treatment	U_{mf} (cm/s)	U (cm/s)	U_{mb} (cm/s)	H_{mf}/H_{mb} (cm/s)
Potato Starch	1	5.79×10^{-3}	2.91	0.343	2.4765
	2	3.20×10^{-2}	2.96	0.444	1.9963
	3	1.41×10^{-2}	3.25	0.125	2.2921
TiO ₂	1	3.72×10^{-5}	1.28	0.334	4.5141
	2	1.37×10^{-4}	1.17	0.432	3.5836
	3	2.92×10^{-5}	1.46	0.241	4.4289

Table 12. Fluidization parameters during the experiments, [62].

Preliminary results of the light scattering signals of the fluidization process for TiO₂

A preliminary prototype was built, for monitoring light scattering signals from the powders during the fluidization process and the surface modification with atmospheric plasma, presented in Figure 44. As mentioned in the previous section, the preliminary fluidization state is done with qualitative analysis. The presented preliminary prototype in this work, aims for a proper instrument for determining a fluidization state in the reactor with a quantitative analysis. So, in future treatments, a real time test could be done, during the process, to know if the fluidization state of the treated powder was achieved. By adding this prototype, a fluidization test will be performed during the surface treatment or prior the surface treatment to have a quantitative test that determine the fluidization state of the sample. The future project will be presented in page 113.

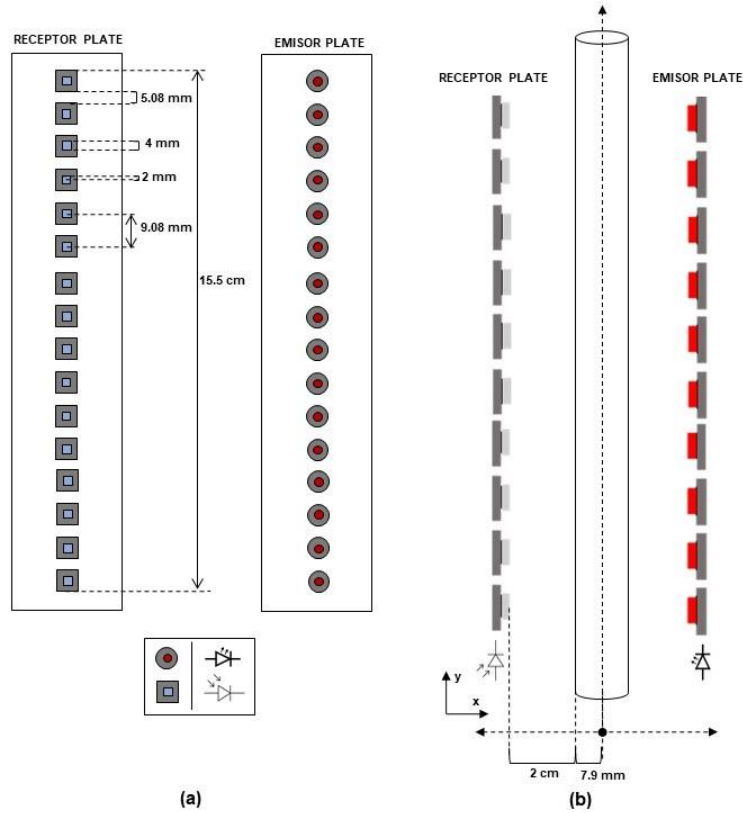
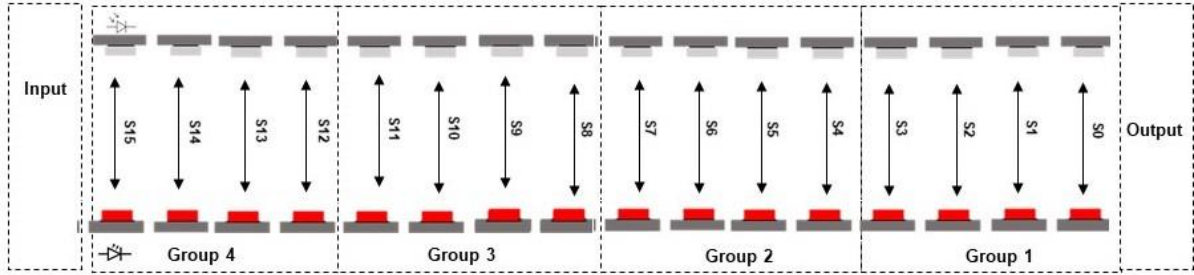


Figure 44. Components diagram of the preliminary prototype for monitoring light scattering signals from the COAX-DBD PFBR. The longitude measurements of the sensors arrays are presented in (a), the distance between the plates and the COAX-DBD PFBR is presented in (b).

As presented in Figure 44, the prototype covers the total longitude of the reactor, Figure 44a, the reactor is placed between the emissor and receptor arrays, Figure 44 (b). The preliminary prototype signal reception starts from the powder container and ends with the output section of the reactor. The prototype was tested in four different situations: flux without powder and plasma presence, for a reference signal (REF_0 in Figure 45b); powder with flux without plasma (PFsP in Figure 45b); plasma without powder for a reference signal in the plasma state (REF_00 in Figure 45b), and powder with flux and plasma (PcP in Figure 45b).



(a)

Sensor	Group	h [cm]	Average				Standard Deviation			
			REF 0	PFsP	REF 00	PcP	REF 0	PFsP	REF 00	PcP
4	2	10.896	0.396	0.175	0.249	0.195	1.403	1.036	0.831	0.54
5		9.988	0.450	0.187	0.486	0.213				
6		9.080	3.203	2.260	1.981	1.295				
7		8.172	0.345	0.203	0.265	0.237				
8	3	7.264	0.635	0.423	0.623	0.883	0.272	0.133	0.071	0.271
9		6.356	0.881	0.562	0.578	0.239				
10		5.448	0.223	0.240	0.458	0.668				
11		4.540	0.604	0.440	0.523	0.676				
12	4	3.632	0.183	0.180	0.233	0.255	0.03	0.792	0.767	0.769
13		2.724	0.174	0.115	0.198	0.163				
14		1.816	0.161	1.751	1.766	1.782				
15		0.908	0.229	0.209	0.268	0.329				

(b)

Figure 45. Average and Standard Deviation values for the Groups 2 through 4. Reference: (REF_0) signal, with flux without powder and plasma Signal, Powder with flux without plasma (PFsP) Reference signal (REF_00), flux with powder and plasma Signal, powder with flux and plasma (PcP)

In Figure 45a the arrangement of the emisors and the detectors is presented. And divided into 4 groups (group1-4). In Figure 45b a table with the average and standard deviation preliminary results obtained from the prototype. In the group 1, from Figure 45a, corresponds to the exit of the gas flux from the reactor, according to the fluidization theory, there should be less granule material and in consequence, the scattered light in this section should be practically the scattered light form the Quartz cylinder. In contrast, in group 4 is placed in the powder holder component in the reactor, so, there should be more granule concentration and the scattered light in this section produced by the granule material. Where the fluidization column is localized, is between groups 3 and 2. According to the direction of the flux, the concentration of the granules is reduced by passing group 3

through group 2. So the scattered light from groups 3 and 2 is different from group 4 where the granules are more separated due to the fluidization state.

The results, of the preliminary prototype for light scattering signals, presented on this work are shown in figures **Error! Reference source not found.** and **Error! Reference source not found.**. These results are taken as an example of how the COAXDBD PFBR will operate to determine the fluidization state during the surface modification process with atmospheric plasma.

In Figure 46, it is shown as an example of the behavior of sensor number 12 from the prototype during a test. This sensor was chosen due to its position, which is the section where the fluidization starts. And the four conditions of the experiment are shown in the graph.

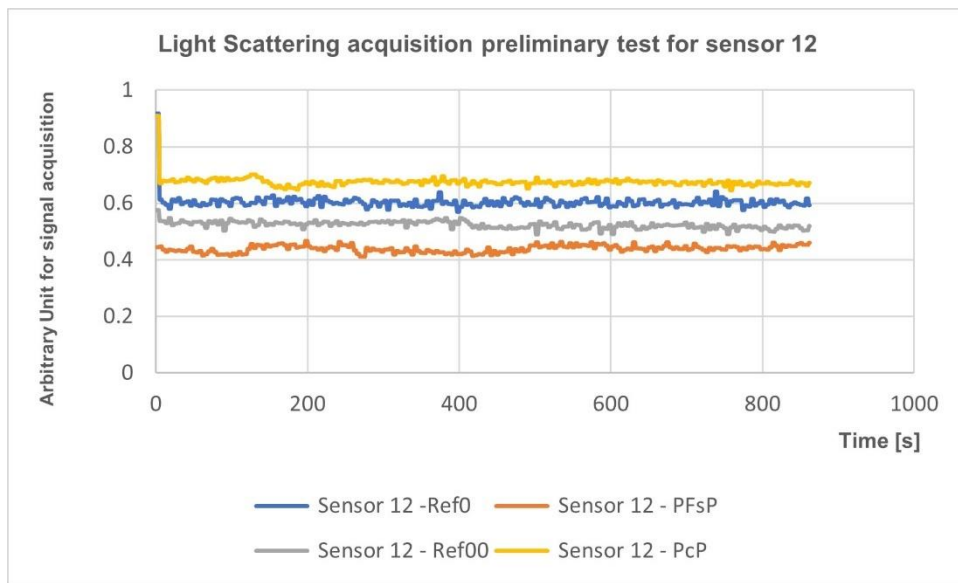


Figure 46. Graph for the behavior of the emitter-receptor plate for sensor 12 for the signal processing of the light scattering during the test. For this figure: Reference: (REF_0) signal, with flux without powder and plasma Signal, Powder with flux without plasma (PFsP) Reference signal (REF_00), flux with powder and plasma Signal, powder with flux and plasma (PcP)

From a treatment process with the COAXDBD PFBR, the light scattering signal prototype was tested. These results were plotted and presented in the graph shown in Figure 47. As mentioned before, this is a prototype and was tested for this research project. These results probe the following: as expected, the data of the scattered light obtained by the prototype, increases as the height of the column also increases, (from section 4 through 2, and then reduces from sections 2 through 1, as presented previously on Figure 45a). And also, the prototype needs to be calibrated to improve and clear the signal processing.

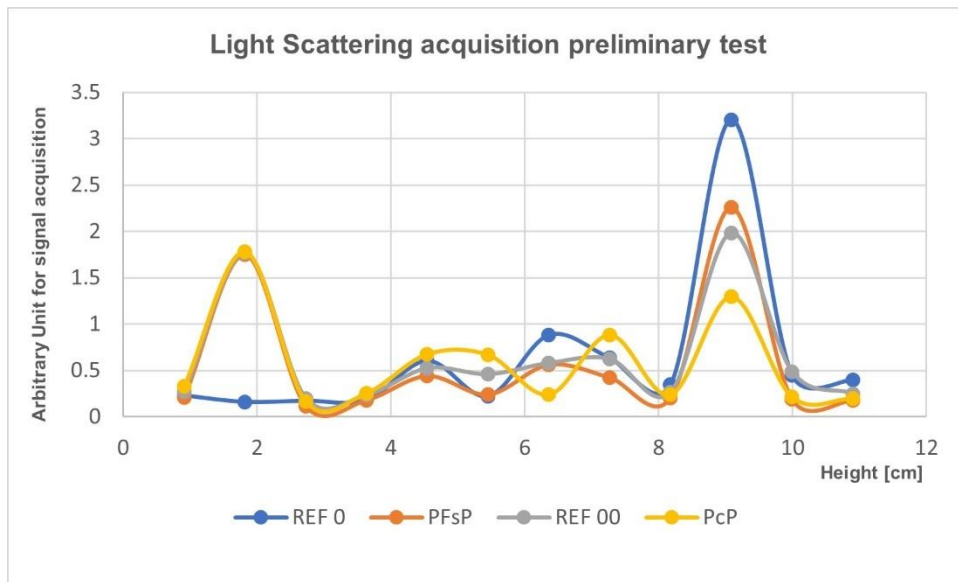


Figure 47. Graph for the preliminary results for the light scattering signal acquisition from the granules during the operation of the COAXDBD PFBR. For this figure: Reference: (REF_0) signal, with flux without powder and plasma Signal, Powder with flux without plasma (PFsP) Reference signal (REF_00), flux with powder and plasma Signal, powder with flux and plasma (PcP)

Preliminary results for the sedimentation properties of the modified TiO₂

For purposes of this work, a qualitative and preliminary test for the sedimentation properties of the treated TiO₂ with atmospheric plasma was performed and is presented in Figure 48. This test, concluded with a qualitative observation and comparison of the interaction between the untreated and treated TiO₂ with pure water. This for testing the operation of the developed COAX-DBD PFBR and as a preliminary test for the procedure of another research work.

The experiment was as follows: treated and untreated TiO₂ was introduced into a graduated glass with pure water and observe the interaction of the mixture. The results were: the sedimentation of the treated TiO₂ powder occurred instantly. While the untreated TiO₂, mixed in the water. The COAX-DBD PFBR, successfully treated the surface of the TiO₂ granules.



Figure 48. Sedimentation test for the treated TiO₂. Untreated TiO₂ in water, left, and treated TiO₂ in water, right.

Granulometry results of the powders

The granulometry measurements of the used powders in this work are presented in this section. Plots for the particle size distribution of the used powders are presented on Figure 49. The results include the untreated and plasma-treated, potato starch (PS), and titanium dioxide (TiO_2). For TiO_2 , the measurement was performed after the separation process, previously explained.

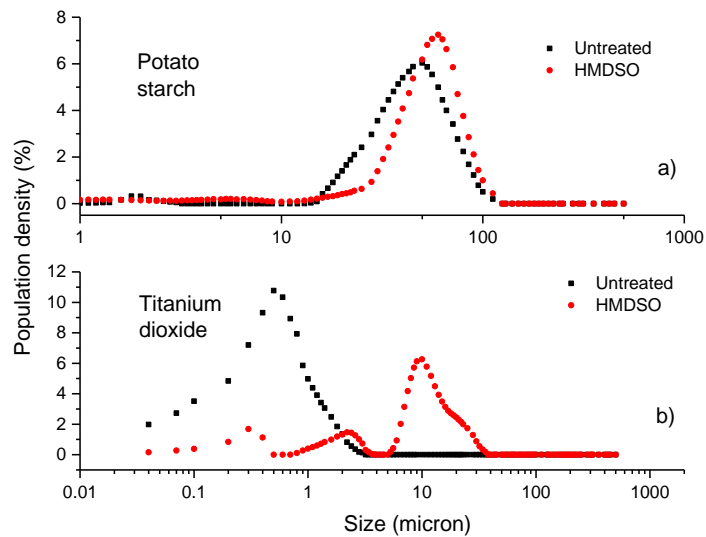


Figure 49. Granulometry results for the Potato Starch (a), and the Titanium Dioxide (b), [62].

For the potato starch, the granulometry results show a small change in size distribution. This, due to particle losses during the process operation of the COAX-DBD PFBR, especially for the small particules [Figure 49(a)]. The particle size for the untreated TiO_2 ; untreated but as previously explained a separation method was used in this work, shows a size distribution peak between 0.5 and 0.6 μm . The TiO_2 granules tend to agglomerate and small agglomerates cannot be broken by physical treatments, such as ultra-sonification, although significantly improves the particles size distribution, [62].

Rheometry and Calorimetry results of the powders

For each plasma treatments in which the Potato Starch (PS) was submitted, the rheological behavior results of the starch were plotted and presented in Figure 50. Where, the Differential Scanning Calorimetry (DSC) values are shown in the inset of the plot image. For the PS treated under the three types of plasma with monomer mixture used in this work (Table 10), differences were found between the untreated and treated PS. All treated granules had a lower viscosity. During this test, this result can be found on the paste formation, in which the starch gelatinization process of the starch is followed. The granules swell by absorbing water and the amylose is leached into the medium allowing the formation of a viscous solution [59], [62]–[64].

In the case of the plasma monomer mixture treatments of: Ar-Acetone and Ar-Methanol, the changes in the viscosity profiles were similar and greater than the case of the plasma monomer mixture of Ar-HMDSO treatment. For the three treatments used in this work, the reduction of viscosity regarding to native starch was significant, [62].

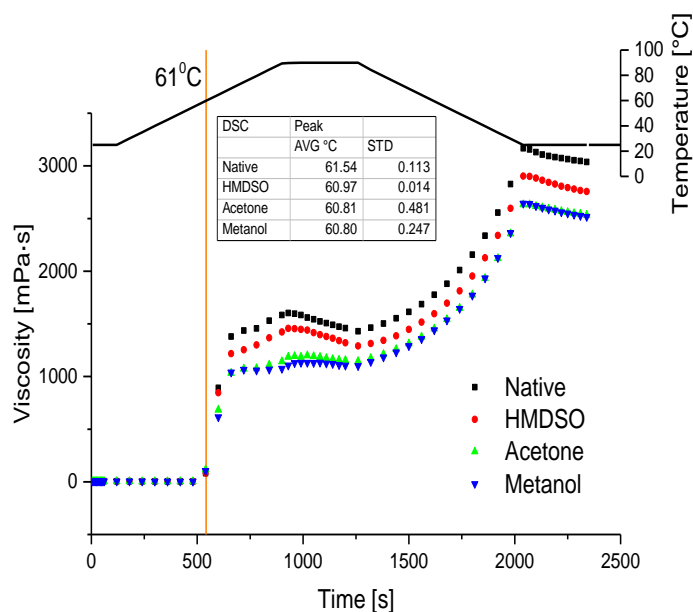


Figure 50. Rheometry results for the potato starch, [62].

The results from thermal analysis of both the untreated and treated PS, are shown in the table inserted in Figure 50. The temperature of gelatinization (T_p) showed a slight decrease as a function of the plasma with monomer mixture treatments, being less for the plasma monomer mixture treatment of Ar-HMDSO, followed by the treatment mixture with Ar-Acetone and finally the treatment mixture of Ar-Methanol. Similar behavior was observed in the viscosity profiles, Figure 50. The slight decrease in the T_p , could be attributed to a depolymerization caused by the incorporation and interaction of plasma species with the starch granule surface, during the monomer-gas mixture breakdown (plasma state), specifically, molecular fragments of the HMDSO molecule, to the starch structure in the three treatments [7], [24], [25], [62], [65].

As mentioned, the decrease in viscosity during the heating of the treated PS, reflects the difficulty of the granules to reach a maximum swelling capacity, as a result in a structural change possibly due to chemical modification on the surface of the granules promoted by surface interaction with the atmospheric plasma monomer mixture, (crosslinking and/or depolymerization). During the cooling stage, both the untreated and treated PS, presented an increase in the viscosity values due to the reorganization of the components (amylose / amylopectin). The leached amylose is relevant in the formation of the paste, as also the remaining granules (amylopectin) [17], [25], [62], [65].

CONCLUSION

The method and results presented in this work, proves that a laboratory scale prototype of a Coaxial-DBD plasma fluidized-bed reactor (COAX-DBD PFBR), for the plasma surface treatment of granular material was designed and constructed and due to its operational process, its capable to modify the surface of organic and inorganic powders, for purposes of this work, Type A and C of the Geldart Scale potato starch and titanium dioxide powders respectively, demonstrated to suffer an alteration after been submitted to the surface modification process with atmospheric plasma by the COAX-DBD PFBR.

The established objectives for this research work were accomplished as follows:

- ✓ First, the fluidization state of the powders: a fluidization column was constructed and tested. This objective concluded for achieving the fluidization state of the powders.
- ✓ Second, gas breakdown and the gas-monomer mixture breakdown (Ar-monomer), with the RF power supply: the electrodes were incorporated into the obtained fluidized column in a Coaxial-DBD configuration. This objective concluded for achieving the plasma state of the gas-monomer mixture breakdown with a Coaxial-DBD configuration.
- ✓ Third, the validation of the operational process of the COAX-DBD PFBR: the surface modification of granular material by achieving the fluidization state of the powders and the plasma state of the mixture of monomer and Argon Gas for each mixture, was achieved.
- ✓ Last, the COAX-DBD PFBR was tested by treating PS and TiO₂ powders. And comparing the properties of the treated and untreated granules. Treated particles suffered alterations in their surface due to the plasma treatment inside the reactor developed to carry out this work. As discussed from the results of the Granulometry, DSC, and Rheometry for the PS granules and the Granulometry, preliminary sedimentation and preliminary Light Scattering study results for the TiO₂ granules.

The results proved that by achieving a fluidization state, a fluidized bed allowed a surface modification resulting in important changes in the behavior of the powders and with no interaction of the sample with the exterior. A fluidization state for fine powders was achieved, TiO₂ (that has cohesive behavior), the reactor showed proper operation. The design of the reactor helped to achieve the required fluidization state and a proper gas breakdown due to its Coaxial-DBD design even if it was a monomer-Argon gas mixture.

Rheometry and DSC results showed a significant alteration on the PS. The modification is promoted by the treatment conditions in which the starch was submitted and an especial route of reaction in the plasma is favored, alteration of structural components of the granule, and potential cross-linking and depolymerization. These changes result in the decrease of the viscosity pattern and a gelatinization taking place at lower temperatures.

The preliminary optical system, implemented as a test for treated TiO₂ samples, working as a preliminary prototype, even with calibration needs, proved that the light scattering from the powders can be used for an early diagnosis to determine if the fluidization state during the plasma treatment process was achieved. This means that instead of using qualitative analysis for measuring the fluidization we can use a quantitative analysis.

The preliminary results from the optical system prototype, show more scattered light from the middle of the reactor than from the upper part. In the middle section of the reactor, the fluidized bed is expected which means the presence of more mass of granules and less mass of granules can be found in the last section of the reactor.

The results of this project, as developed, were presented in different national and international research conferences and workshops, as presented in annex 6.

Future Work

The future work of this project is to improve the operational process and measures of the reactor for industrial purposes. These is by the joint between the corrected optical prototype

and the COAX-DBD PFBR, the surface modification of more Type C powders or any type of powders and to improve the mechanical vibration and measurements of the reactor to avoid agglomeration for more cohesive powders and to increase the amount of treated sample.

The objective of the joint between the Optical System with the COAX-DBD PFBR, is to improve the process of surface modification of powders, to have a non-invasive preliminary diagnostic of the achievement of the fluidization state, in real time, during the plasma surface treatment. Also, the fluidization for cohesive powders can continue by treating more Type C powders, due to its lack of information and industrial potential, specially of starches, such as: corn starch, rice starch, amaranth starch, among others. With an improvement of the mechanical vibration, by attaching a vibrating device on the external wall of the reactor [48]. And by increasing the measures of the reactor, specially the height of the column, the amount of treated powder can be increased. This last is for improving the operational process so the reactor can have industrial applications [8], [47]. For the fluidization column, the lids can be corrected, as the ones used in the DBD reactors for the hydrogen production from methane gas [33] and for the study of ammonia formation in low pressure plasma [41]. The lids designs are presented in: Figure 51.

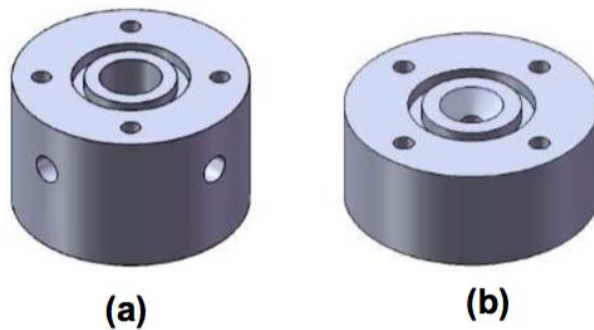


Figure 51: Alternative lids for the DBD reactor. The Superior (a) and inferior (b) lids. The material for these parts can be also nylomaq or nylamid, with $\frac{1}{2}$ " wholes for input and output gases. These designs were taken from [20].

Part of this suggestions have already been designed, as presented in figures 51, Figure 52 and Figure 53. Which present the design of the reactor with the optical system joint with the reactor. The proposed modification for the optical system is as follows: adding a second receptor plate, as is shown in Figure 52.

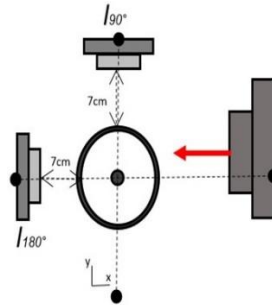


Figure 52. Diagram of the optical prototype with two photodetectors plates.

For this, a special base must be placed for hosting the optical plates. This device must be added without interfering the other additions and systems, such as the mechanical vibration, fluidization and plasma generation systems. The best solution for this is proposed to be inserted in an aluminum structure, the design for this structure is presented in: Figure 53.

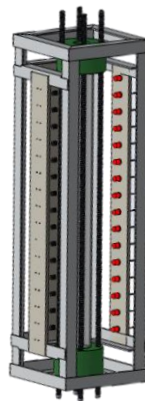


Figure 53. The design model of the joint between the optical prototype and the COAX-DBD Fluidized Plasma reactor

REFERENCES

- [1] E. Rivas, Ortega, *Unit Operations of Particulate solids*. 1987.
- [2] M. Rhodes, *Introduction to Particle Technology: Second Edition*, 2nd ed. John Wiley & Sons, 2008.
- [3] J. M. Valverde Millán, *Fluidization of Fine Powders*, vol. 18. 2013.
- [4] Malvern Instruments Ltd, “A basic guide to particle characterization,” Worcestershire, 2015. [Online]. Available: https://www.cif.iastate.edu/sites/default/files/uploads/Other_Inst/Particle Size/Particle Characterization Guide.pdf.
- [5] D. Rungtiwa, W.; Panakamol, D.; Weerawut, C.; Sawanee, H.; Kesini, L.; Manop, S.; Asira, F.; Somsak, “Modification of Tapioca starch by non-chemical route using jet atmospheric argon plasma,” *Carbohydr. Polym.*, no. 102, pp. 790–798, 2014.
- [6] F. Chang, X. He, X. Fu, Q. Huang, and Y. Qiu, “Preparation and characterization of modified starch granules with high hydrophobicity and flowability.,” *Food Chem.*, vol. 152, pp. 177–83, Jan. 2014, doi: 10.1016/j.foodchem.2013.11.140.
- [7] R. Thirumdas, A. Trimukhe, R. R. Deshmukh, and U. S. Annapure, *Functional and rheological properties of cold plasma treated rice starch*, vol. 157. Elsevier Ltd., 2017.
- [8] W. J., “Measurement techniques in fluidized beds,” *Powder Technol.*, no. 102, pp. 15–36, 1999.
- [9] B. R. A. Prescott J. K., “On Powder Flowability,” *Pharm. Technol.*, vol. 24, no. 10, pp. 60–84, 2000.
- [10] L. Wang, “Fluidization of Fine particles and the effects of additive particles,” 1995.
- [11] K. T. Cocco R., Reddy Karri S. B., “Introduction to fluidization,” *AIChE - CEP Mag.*, no. November, pp. 21–29, 2014.
- [12] R. Xu, “Light scattering: A review of particle characterization applications,” *Particuology*,

vol. 18, pp. 11–21, Feb. 2015, doi: 10.1016/j.partic.2014.05.002.

- [13] R. Xu, *Particle Characterization: Light Scattering Methods*, vol. 13. Springer, 2002.
- [14] A. R. Abrahamsen and D. Geldart, “Behaviour of gas-fluidized beds of fine powders part I. Homogeneous expansion,” *Powder Technol.*, vol. 26, no. 1, pp. 35–46, 1980, doi: 10.1016/0032-5910(80)85005-4.
- [15] D. Geldart, “Types of gas fluidization,” *Powder Technol.*, vol. 7, no. 5, pp. 285–292, 1973, doi: 10.1016/0032-5910(73)80037-3.
- [16] Abrahamsen A. R.; Geldart D., “Behaviour of Gas-Fluidized Beds of Fine Powders Part II. Voidage of the dense phase in bubbling beds,” *Powder Technol.*, no. 26, pp. 47–55, 1980.
- [17] J. A. Medina and J. Salas, “Caracterización morfológica del granulo de almidón nativo: Apariencia, forma, tamaño y su distribución,” *Rev. Ing.*, vol. 27, pp. 56–62, 2008, [Online]. Available: <http://www.scielo.org.co/pdf/ring/n27/n27a7.pdf>.
- [18] O. Paredes-López, L. A. Bello-Pérez, and M. G. López, “Amylopectin: Structural, gelatinisation and retrogradation studies,” *Food Chem.*, vol. 50, no. 4, pp. 411–417, Jan. 1994, doi: 10.1016/0308-8146(94)90215-1.
- [19] J. H. Cho, “RF pulsed plasma surface modification of titanium dioxide nanoparticles for environmental applications,” University of Texas at Arlington, 2005.
- [20] L. Jezerska, J. Hlosta, M. Zidek, J. Zegzulka, J. Necas, and K. M. Kutlakova, “Comparative Study of Titanium Dioxides Rheological Properties,” in *NANOCON 2014*, 2014.
- [21] S. C. Alcázar-Alay and M. A. A. Meireles, “Physicochemical properties, modifications and applications of starches from different botanical sources,” *Food Sci. Technol.*, vol. 35, no. 2, pp. 215–236, 2015, doi: 10.1590/1678-457X.6749.
- [22] F. Zhu, “Plasma modification of starch,” *Food Chem.*, vol. 232, pp. 476–486, 2017, doi: 10.1016/j.foodchem.2017.04.024.
- [23] G. A. Arolkar, M. J. Salgo, V. Kelkar-Mane, and R. R. Deshmukh, “The study of air-plasma treatment on corn starch/poly(e-caprolactone) films,” *Polym. Degrad. Stab.*, vol. 120, pp.

262–272, 2015, doi: 10.1016/j.polymdegradstab.2015.07.016.

- [24] J. A. Medina and J. Salas, “Caracterización morfológica del granulo de almidón nativo: Apariencia, forma, tamaño y su distribución,” *Rev. Ing.*, vol. 27, pp. 56–62, 2008.
- [25] M. G. Casarrubias-castillo, G. Méndez-montevalvo, S. L. Rodríguez-ambriz, C. De Desarrollo, D. P. Bióticos, and P. Nacional, “Diferencias estructurales y reológicas entre almidones de frutas y cereales,” pp. 455–466, 2012.
- [26] S. Khorram, M. Zakerhamidi, and Z. Karimzadeh, “Polarity functions’ characterization and the mechanism of starch modification by DC glow discharge plasma,” *Carbohydr. Polym.*, vol. 127, pp. 72–78, 2015, doi: 10.1016/j.carbpol.2015.03.056.
- [27] A. Tecante and J. L. Doublier, “Steady flow and viscoelastic behavior of crosslinked waxy corn starch- κ -carrageenan pastes and gels,” *Carbohydr. Polym.*, vol. 40, no. 3, pp. 221–231, 1999, doi: 10.1016/S0144-8617(99)00057-0.
- [28] J. F. Steffe, *Rheological Methods in*, vol. 23, no. 2. 1996.
- [29] M. DeSilveira, S.R. ; Schnitzler, E.; Silveira, P. S.; Soltovski, C.;Lazarotto, “Investigation of the photo-oxidation of cassava-starch granules,” *J. Therm Anal Calom*, no. 123, pp. 2129–2137, 2015.
- [30] D. K. Ram, “The Determination of Minimum Bubbling Velocity , Minimum Fluidization Velocity and Fluidization Index of Fine Powders (Hematite) using Gas-Solid Tapered Beds,” *Int. J. Sci. Eng. Res.*, vol. 1, no. 1–3, pp. 287–293, 2013.
- [31] F. Chen, *Introduction to Plasma Physics and Controlled Fusion*. 2016.
- [32] C. S. Wong and R. Mongkolnavin, *Elements of Plasma Technology*. 2016.
- [33] Figueroa Hernández A. M., “Construcción y caracterización de un reactor de plasma de barrera dieléctrica para la producción de hidrógeno a partir de gas metano,” Instituto Politécnico Nacional, 2010.
- [34] Lizbeth Soto Ruvalcaba, “Desarrollo de un sistema para generación de plasma basado en una descarga de barrera dieléctrica coplanar,” Instituto Politécnico Nacional, 2014.

- [35] R. A. Wolf, *Atmospheric pressure plasma for surface modification*. John Wiley & Sons, 2013.
- [36] J. Harry, *Introduction to Plasma Technology Science, Engineering and Applications*. Weinheim: Wiley-VCH Verlag GmbH, 2010.
- [37] J. Y. R. Ruiz, “Evaluación del efecto del tratamiento con plasma frío en los compuestos volátiles de sabor de nuez de pecana (*Carya illinoensis*),” Instituto Politécnico Nacional, 2014.
- [38] J. R. Roth, *Industrial Plasma Engineering: Applications to Nonthermal Plasma Processing*, vol. 2. 2001.
- [39] J. R. Roth, *Industrial Plasma Engineering: Principles*, vol. 1. 2001.
- [40] U. Kogelschatz, “Dielectric-barrier Discharges : Their History, Discharge Physics, and Industrial Applications,” *Plasma Chem. Plasma Process.*, vol. 23, no. 1, pp. 1–46, 2003, doi: 10.1023/A:1022470901385.
- [41] B. T. Arévalo, “Estudio de la formación de amoníaco en plasmas de Baja Temperatura,” Instituto Politécnico Nacional, 2013.
- [42] D. Merche, N. Vandencastele, and F. Reniers, “Atmospheric plasmas for thin film deposition: A critical review,” *Thin Solid Films*, vol. 520, no. 13, pp. 4219–4236, 2012, doi: 10.1016/j.tsf.2012.01.026.
- [43] F. I. H. Pashaie, Bijan, Shirshak K Dhali, “Electrical characteristics of dielectric barrier discharge,” *J. Phys. D Appl. Phys.*, no. 27, pp. 2107–2110, 1994.
- [44] Campos Díaz K. E., “Determinación de la porosidad de un lecho de partículas con biopelícula en fluidización inversa en dos fases (sólido-líquido),” Instituto Politécnico Nacional, 2007.
- [45] B. Abdelgawad, “Design of a Gas-Solid Fluidized Bed Reactor at High Temperature and High Pressure,” Polytechnic School of Montreal, 2013.
- [46] J. M. Valverde Millán, *Fluidization of Fine Powders*, vol. 18. 2013.
- [47] Z. Wang, M. Kwauk, and H. Li, “Fluidization of fine particles,” *Chem. Eng. Sci.*, vol. 53, no.

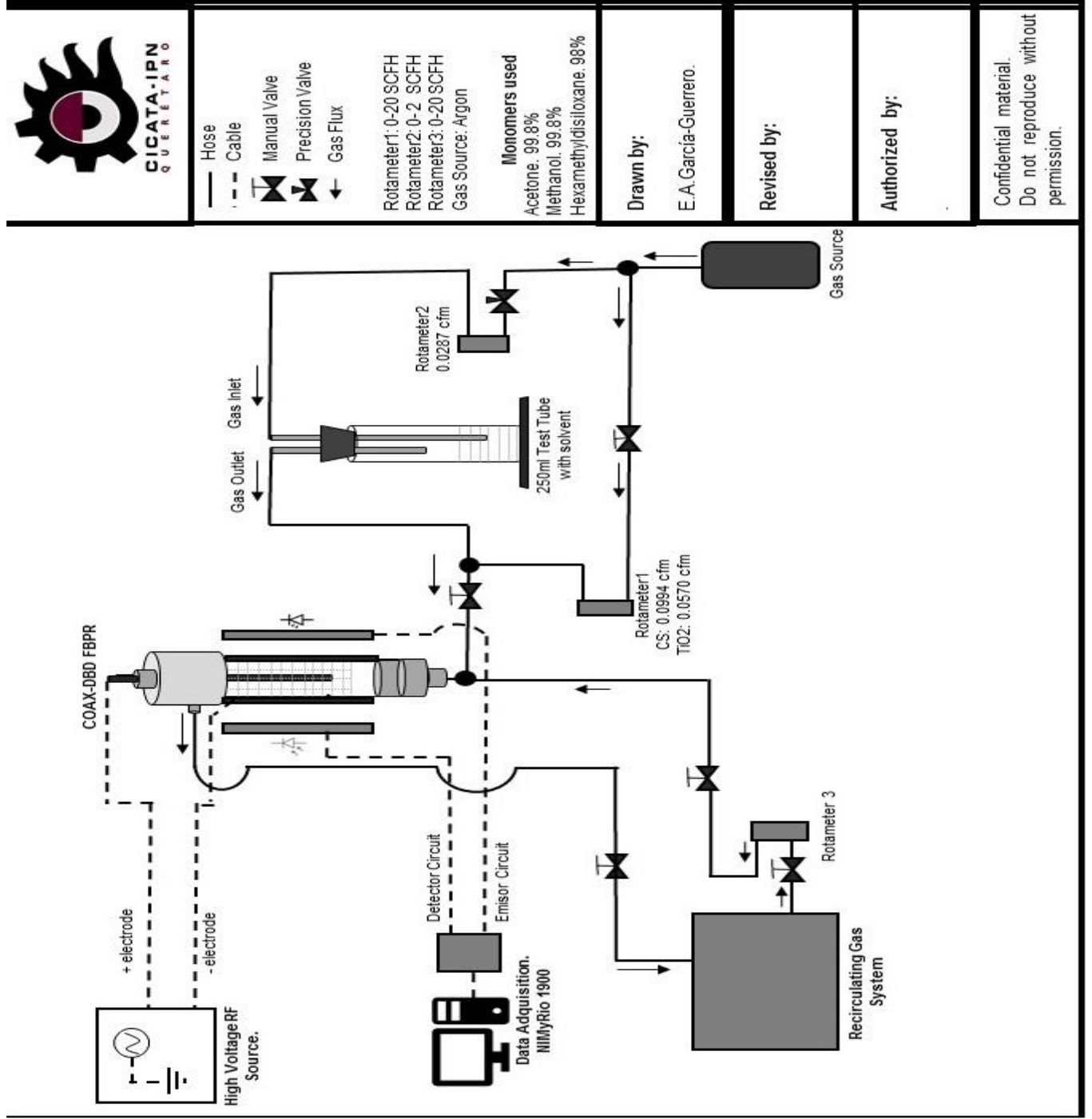
- 3, pp. 377–395, 1998, doi: 10.1016/S0009-2509(97)00280-7.
- [48] R. P. Barletta D., Donsi G., Ferrari G., Poletto M., “The effect of mechanical vibration on gas fluidization of a fine aerable powder,” *Chem. Eng. Res. Des.*, no. 86, pp. 359–369, 2008.
- [49] S. H. Jung, S. H. Park, D. H. Lee, and S. D. Kim, “Surface modification of fine powders by atmospheric pressure plasma in a circulating fluidized bed reactor,” *Ind. Eng. Chem. Res.*, vol. 43, pp. 5483–5488, 2004, doi: 10.1021/ie034216w.
- [50] Y. Chen, J. Yang, R. N. Dave, and R. Pfeffer, “Fluidization of Coated Group C Powders,” *AIChE J.*, vol. 54, no. 1, pp. 104–121, 2008, doi: 10.1002/aic.
- [51] C. R. Wierenga and T. J. Morin, “Characterization of a fluidized-bed plasma reactor,” *AIChE J.*, vol. 35, no. 9, pp. 1555–1558, 1989, doi: 10.1002/aic.690350918.
- [52] A. R. Abrahamsen and D. Geldart, “Behaviour of gas-fluidized beds of fine powders part I. Homogeneous expansion,” *Powder Technol.*, vol. 26, no. 1, pp. 35–46, 1980, doi: 10.1016/0032-5910(80)85005-4.
- [53] M. Nitschke, “Polymer Surfaces and Interfaces,” in *Springer Berlin Heidelberg*, M. Stamm, Ed. Springer Berlin Heidelberg, 2008, p. 203.
- [54] J. Friedrich, “Mechanisms of plasma polymerization - Reviewed from a chemical point of view,” *Plasma Process. Polym.*, vol. 8, no. 9, pp. 783–802, 2011, doi: 10.1002/ppap.201100038.
- [55] M. Thomas and K. L. Mittal, *Atmospheric Pressure Plasma Treatment of Polymers: Relevance to Adhesion*. 2013.
- [56] B. Pashaie, S. K. Dhali, and F. I. Honea, “Electrical characteristics of a coaxial dielectric barrier discharge,” *J. Phys. D. Appl. Phys.*, vol. 27, no. 10, p. 2107, 1994.
- [57] S. H. Jung, S. H. Park, D. H. Lee, and S. D. Kim, “Surface modification of HDPE powders by oxygen plasma in a circulating fluidized bed reactor,” *Polym. Bull.*, vol. 47, no. 2, pp. 199–205, Oct. 2001, doi: 10.1007/s002890170012.
- [58] C. Roth, Z. Künsch, A. Sonnenfeld, and P. Rudolf von Rohr, “Plasma surface modification

of powders for pharmaceutical applications,” *Surf. Coatings Technol.*, vol. 205, no. SUPPL. 2, pp. S597–S600, 2011, doi: 10.1016/j.surfcoat.2010.10.046.


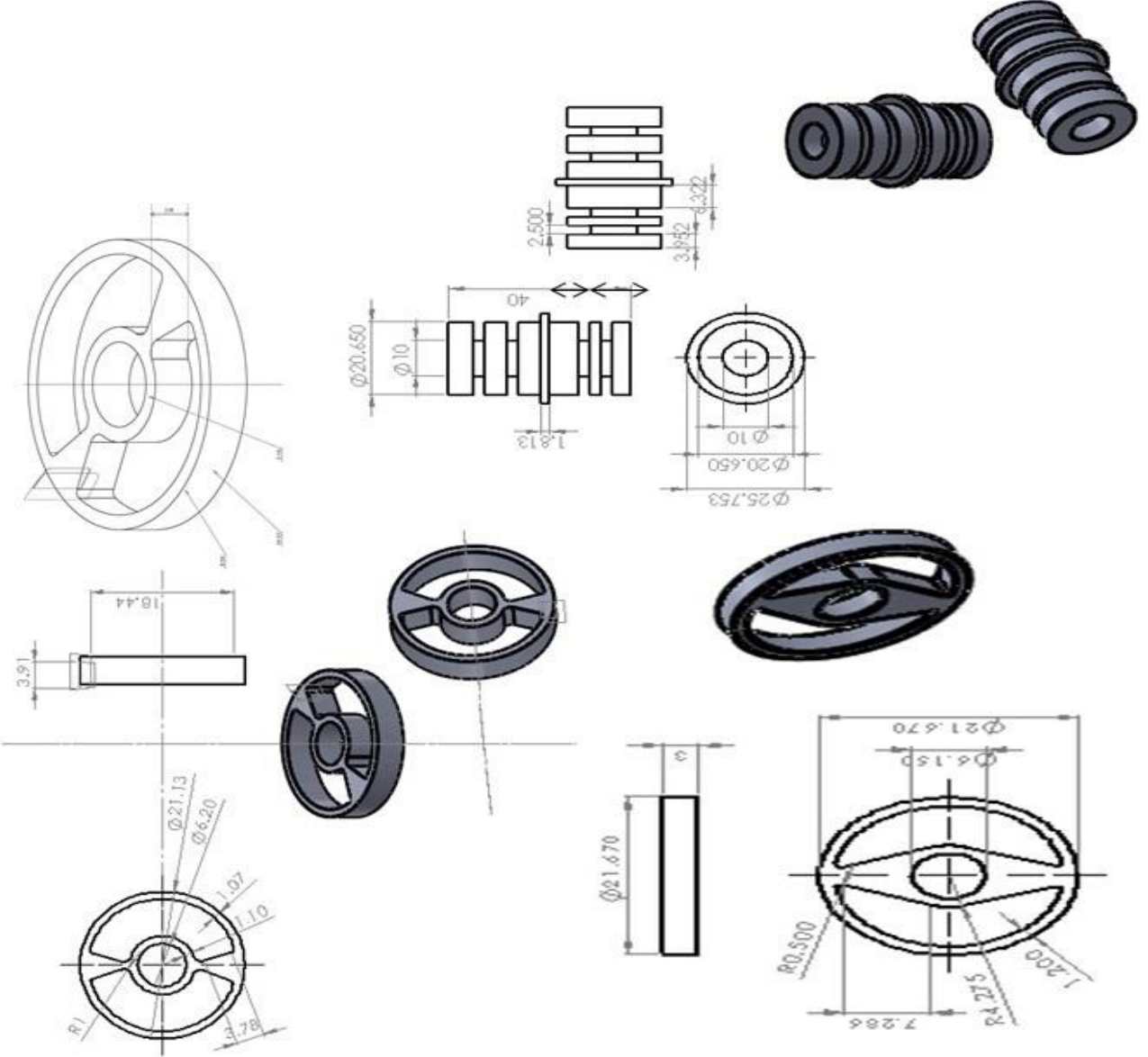
- [59] R. Thirumdas, A. Trimukhe, R. R. Deshmukh, and U. S. Annapure, *Functional and rheological properties of cold plasma treated rice starch*, vol. 157. Elsevier Ltd., 2017.
- [60] S. Swaraj, U. Oran, A. Lippitz, J. F. Friedrich, and W. E. S. Unger, “Aging of plasma-deposited films prepared from organic monomers,” *Plasma Process. Polym.*, vol. 4, no. SUPPL.1, pp. 784–789, 2007, doi: 10.1002/ppap.200731905.
- [61] Parker Hannifin Corporation, “T-Slot Aluminum Framing - Parker Industrial Profile Systems,” Wadsworth, 2016.
- [62] E. A. Garcia-Guerrero *et al.*, “Use of a COAX-DBD Plasma Fluidized-Bed Reactor for Surface Modification of TiO₂ and Potato-Starch Powders,” *IEEE Trans. Plasma Sci.*, 2018, doi: 10.1109/TPS.2018.2824825.
- [63] P. J. Jenkins and A. M. Donald, “Gelatinisation of starch: A combined SAXS/WAXS/DSC and SANS study,” *Carbohydr. Res.*, vol. 308, no. 1–2, pp. 133–147, 1998, doi: 10.1016/S0008-6215(98)00079-2.
- [64] J. Carlstedt, J. Wojtasz, P. Fyhr, and V. Kocherbitov, “Understanding starch gelatinization: The phase diagram approach,” *Carbohydr. Polym.*, vol. 129, pp. 62–69, 2015, doi: 10.1016/j.carbpol.2015.04.045.
- [65] Lin-Jay, “Structural Features of starch granules II,” *Starch Chem. Technol.*, no. Academic 2009, pp. 193–236, 2009.

APPENDICES

APPENDIX 1 : SURFACE MODIFICATION OPERATION DIAGRAM



APPENDIX 2: COMPONENTS OF THE REACTOR

 <p>CICATA-IPN QUERÉTARO</p>	<p>Title: Upper part components of the reactor.</p>	<p>Drawn by: E.A.García-Guerrero.</p>	<p>Revised by:</p>	<p>Authorized by:</p>	<p>Confidential material. Do not reproduce without permission.</p>
					



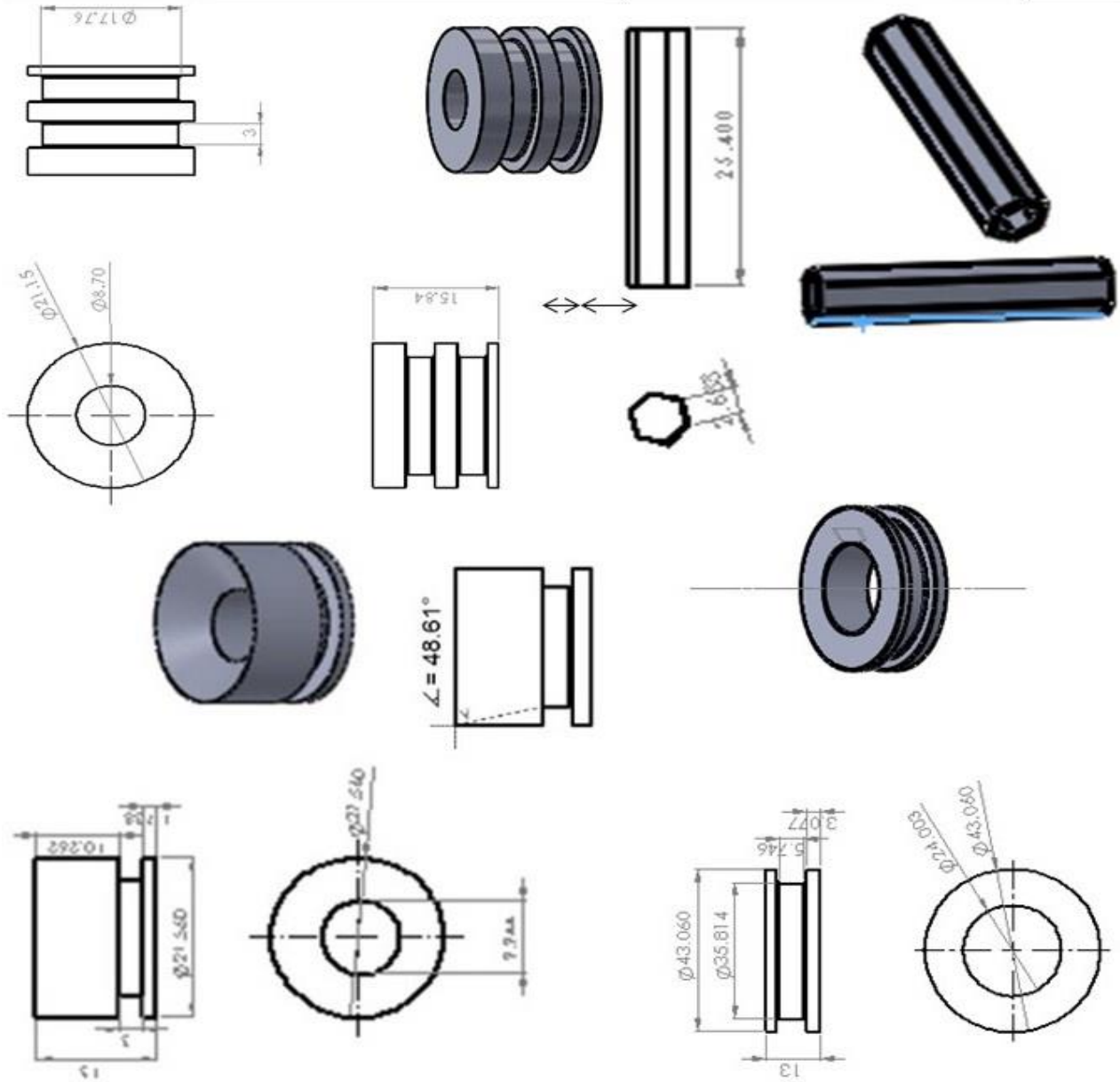
Title:
Fluidization
components.

Drawn by:
E.A.García-Guerrero.

Revised by:

Authorized by:

Confidential material.
Do not reproduce without
permission.



APPENDIX 3: ASSEMBLE OF THE REACTOR MANUAL

For a proper assembly and disassembly of the elements of the reactor, it must be armed as listed in the following schematic images.

Figure 54 shows the reactor armed and with the components labeled, including the upper and lower components. This is very important for a proper assembly and disassembly. The upper part is conformed by the: out-put piece, upper-union piece, the inner electrode and the mesh part of the reactor. The lower part of the reactor is the other half, were the powder container piece, distributor, holder piece, plenum and input piece are located.

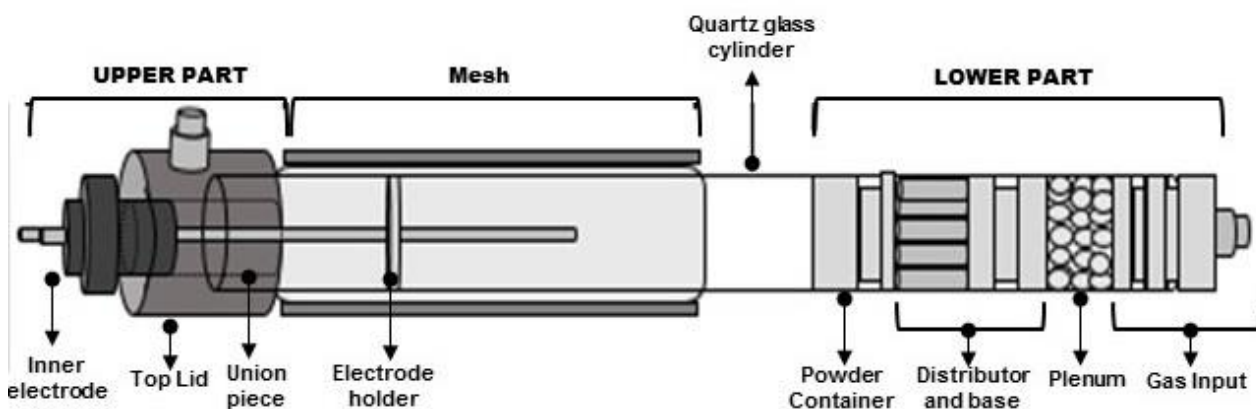


Figure 54. Schematic of the reactor, armed and with all the components labeled.

Taking these in consideration, both parts (lower and upper) must be assembled and disassembled.

For the Assemble of the reactor:

As shown in Figure 55 for the lower part of the reactor and first part of the assemble is introducing the components in the following order: powder container, distributor and base, plenum and finally the gas input piece.

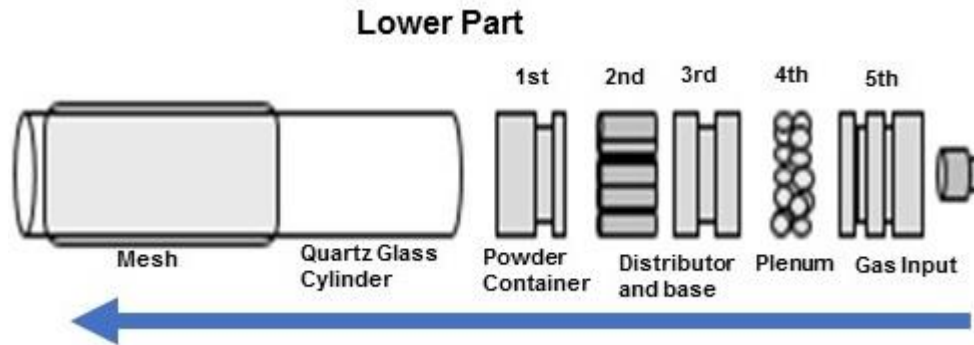


Figure 55. Schematic of the order of the lower components when assembled.

After this, the reactor can be settled in the testing bench. Then the powder must be introduced. For the upper part of the reactor, as shown on Figure 56, the upper part is armed by screwing in the inner electrode into the pvc top lid, then introducing the electrode holder in the opposite side of the inner electrode, then the union piece is introduced into the pvc top lid. Following these, a second electrode holder is introduced into the inner electrode.

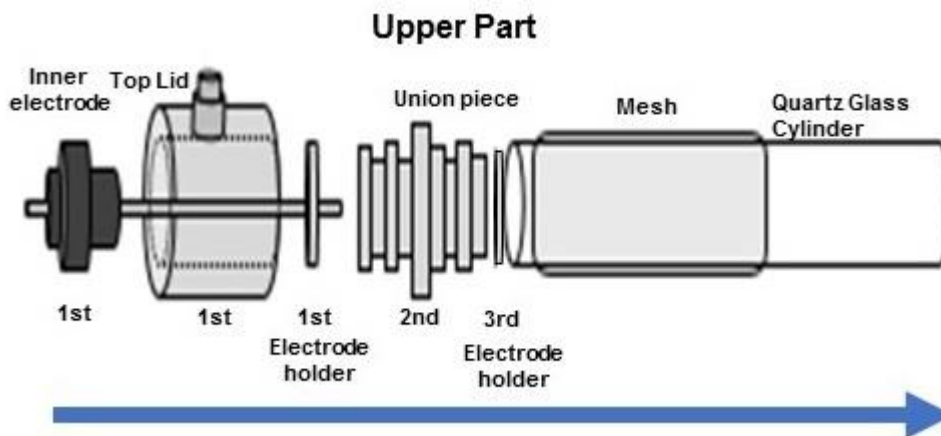


Figure 56. Schematic of the order of the upper components when assembled.

As shown in Figure 56, the assembled upper component (inner electrode, top lid, 2 electrode holders, union piece) is introduced into the quartz glass cylinder.

For the Disassemble of the reactor:

By the other hand, all the elements must be extracted in the opposite way, from the lower to the upper part. First the reactor must be dismantled from the testing bench. The upper part is extracted and then the powder. From this, we obtain the upper part and must be disarmed as shown on Figure 57.

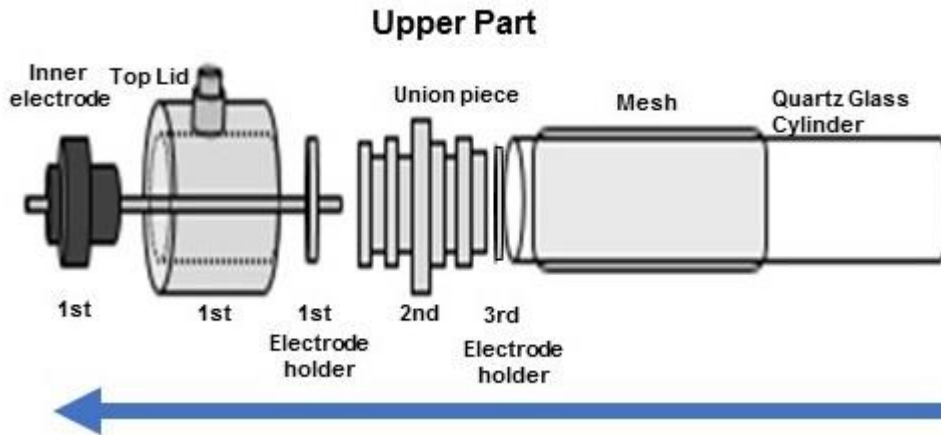


Figure 57. Schematic of the order of the upper components when disassembled.

The lower part must be done after extracting the powder. As shown in Figure 57.

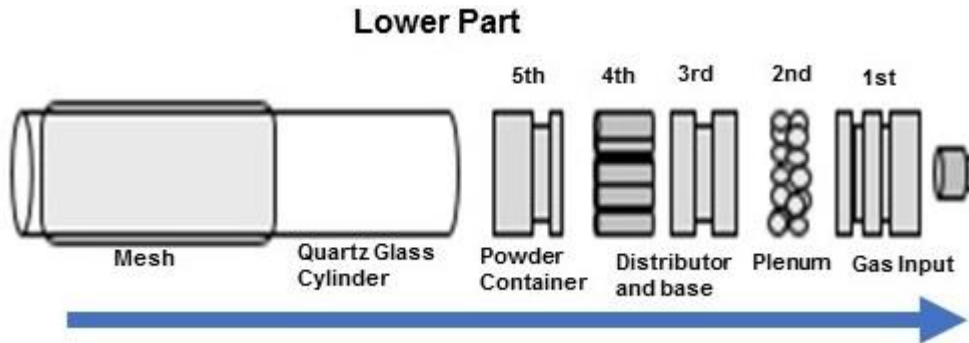


Figure 58. Schematic of the order of the lower components when disassembled.

APPENDIX 4: CLEANING MANUAL

For a proper use, one important aspect for the maintenance of the reactor is the cleaning before and after the treatments.

Materials needed:

- Solvents: alcohol or acetone.
- Commercial soap (used for washing dishes).
- Napkins for optical devices.
- Latex gloves.
- Escobillones

Preliminary cleaning before operating the reactor:

- 1) Wearing the latex gloves, put alcohol or acetone to a napkin.
- 2) Clean the surface of all the components of the reactor, these are the pieces containing the upper part, the lower part and the quartz-glass cylinder; as shown on Appendix 3.
- 3) Assembly the reactor, as shown on Appendix 3.

Cleaning the reactor after treatments.

- 1) Disarm the reactor.
- 2) Wash all the components of the reactor: the test tube, all the pieces containing the upper and lower part and the quartz-glass cylinder.
- 3) Let dry and repeat the preliminary cleaning steps when dry.
- 4) Assemble the reactor, as shown on Appendix 3.

APPENDIX 5: OPERATION MANUAL

The operation of the reactor is not a difficult task but must be handled carefully. The steps include the set-up of the: fluidization and plasma systems.

Fluidization system:

1. All valves from the laboratory should be closed.
2. Connect the rotameters used for this reactor, which are: the 0-2 and the 3-20 [ft³/hr].
3. Connect the air pump to each rotameter and test for any leak.
4. With the air pump set the rotameters for the test, then close the inlets, this will help for the test for having the flux ready any time the inlet valves of each rotameter are open instead of measuring the flux and wasting argon gas.
5. Assemble the lower part of the reactor, as shown on Appendix 3.
6. Prepare the sample.
7. Enter the sample into the reactor and assemble the upper part of the reactor, Appendix 3.
8. Open the inlet valves of the Argon gas tank. Situated in the tank depot of the building.

Plasma System

The red-square button is the turn on and off button, the blue knob and the display, are the frequency indicator and frequency display respectively. The black knob is the voltage regulator and the stick button is the turn on and off output voltage.

1. The RF source should be disconnected before using.
2. Connect the RF source.
3. Turn on the the RF source.
4. Adjust the frequency needed.
5. Turn on the voltage output.
6. Twist the voltage indicator until gas breakup.
7. When finished, twist until zero the voltage indicator, turn off the voltage output and turn of the RF source.

APPENDIX 6: RESEARCH PRODUCTS

SPRING 2016 (A16)

CONFERENCE PARTICIPATION: POSTER

E. A. García-Guerrero, G. López-Echavarría, M. Nieto-Pérez, J. A. Huerta Ruelas, G. Méndez-Montealvo, G. Velázquez-delaCruz. "Surface modification of Starch by a DBD Discharge with the aid of a fluidized bed" POSTER. 43rd IEEE International Conference on Plasma Science. Banff, AB. June 19-23 2016.

FALL 2016 (B16)

CONFERENCE ASSISTANCE & PARTICIPATION: POSTER: *E. A. García-Guerrero, M. Nieto-Pérez, J. A. Huerta Ruelas. "Desarrollo y Caracterización de un Reactor de Plasma de Lecho Fluidizado por Luz Esparcida." POSTER. III Congreso de Ciencia y Tecnología Avanzada. Querétaro, Querétaro. September 28-30 2016.*

CONFERENCE ASSISTANCE & PARTICIPATION: POSTER: *E. A. García-Guerrero, G. López-Echavarría, M. Nieto-Pérez, J. A. Huerta Ruelas, G. Méndez-Montealvo, G. Velázquez-delaCruz. "Surface Modification of Powders Using a Coaxial Dielectric Barrier Discharge." POSTER. LIX Congreso Nacional de Física (National Physics Conference). León, Guanajuato. October 2-7 2016.*

SPRING 2017 (A17)

CONFERENCE ASSISTANCE & PARTICIPATION: POSTER

E. A. García-Guerrero, Michelle Tirado-Guerrero, G. López-Echavarría, M. Nieto-Pérez, J. A. Huerta Ruelas, G. Méndez-Montealvo, G. Velázquez-delaCruz. "Surface Modification of Corn Starch and TiO₂ with a Coaxial DBD Reactor and with the Aid of a Fluidized-Bed." POSTER. 44rd IEEE International Conference on Plasma Science. Atlantic City, NJ. May 21-25 2017.

CONFERENCE ASSISTANCE & PARTICIPATION: POSTER

E. A. G-Guerrero, M. Nieto-Pérez, J. A. Huerta Ruelas. "Development of a Fluidized-Bed Plasma Reactor to Modify Granulated media Monitored with a Laser Light Scattering Signals." POSTER. Latin American Workshop on Plasma Physics 2017, (LAWPP 2017) Cd. De México, México. September 03-07 2017.

FALL 2017 (B17)

Scientific Article: (sended: 11/04/2017, published: 05/08/2018) *E. A. García-Guerrero, Michelle Tirado-Guerrero, G. López-Echavarría, M. Nieto-Pérez, J. A. Huerta Ruelas, G. Méndez-Montealvo, G. Velázquez-delaCruz. "Construction and Assessment of a Coaxial-DBD Plasma Fluidized-Bed Reactor." Transactions on Plasma Sciences. Special Issue LAWPP 2017. Vol:46 Issue: 7 July 2018 pages: 2425-2434
DOI: 10.1109/TPS.2018.2824825
Print ISSN: 0093-3813 Electronic ISSN: 1939-9375*

PROTOTYPE:

*Testing Bench for the Industrial Applications of Atmospheric Plasmas' Laboratory, for the IPN-CICATA Querétaro.
Coaxial-DBD Fluidized-bed Plasma Reactor*

Use of a COAX-DBD Plasma Fluidized-Bed Reactor for Surface Modification of TiO₂ and Potato-Starch Powders

Enrique Augusto García-Guerrero^{ID}, Martín de Jesús Nieto-Pérez^{ID}, *Senior Member, IEEE*,
Gerardo López-Echevarría, Michelle Tirado-Guerrero, Jorge Adalberto Huerta-Ruelas,
Ma. Guadalupe del Carmen Méndez-Montevalvo, and Gonzalo Velázquez

Abstract—The interest of studying the plasma treatment of small particles such as powders or granules has increased over the years. Organic- and inorganic-treated powders have several industrial applications, and their surface modification allows obtaining different desirable properties. A plasma fluidized-bed reactor was constructed and tested to assess the atmospheric plasma surface treatment of powders. Among all type of powders, there is a growing interest in studying the surface treatment of type-C and type-A powders in the Geldart scale. The surface modification of powder in this reactor is achieved when small particles are exposed to a coaxial-dielectric barrier discharge (COAX-DBD). The results include the analysis of two types of powders (organic and inorganic) treated by three atmospheric plasma sources. For the organic powder (potato starch, type A), calorimetry and rheological tests were performed to assess changes in the rheological behavior and thermal properties as a consequence of plasma exposure. For the inorganic powder (titanium dioxide, type C), changes in the settling time before and after plasma treatments were measured using a turbidimeter to detect modifications in the powder surface. The dielectric barrier plasma discharge was generated by the COAX-DBD at 12 kV_{pp} and 25 kHz obtained by a radio frequency power supply. The results show that treatments with plasma reactor modified the properties in both powder types.

Index Terms—Atmospheric plasmas, dielectric barrier discharge (DBD), fluidization, plasma applications, plasma surface modification.

I. INTRODUCTION

PLASMAS have been used as an efficient tool for surface modification in a wide range of materials for many years. In the case of atmospheric plasmas, many of these surface modifications are performed on flat objects [1], [2] or even volumetric, macroscopic objects [3], [4]. One of the most common methods for obtaining atmospheric pressure plasmas is the dielectric barrier discharge (DBD), first reported by Siemens in 1857 for ozone generation [5]. In the nonequilibrium plasma processing, this method is accepted in the

industry for handling large gas volumes [5], [6]. The DBD method is increasing in popularity as a source of nonthermal plasmas at atmospheric pressure. Atmospheric plasmas are a rich source of radicals, excited, and ionized species under affable conditions. However, unlike vacuum operation which easily leads to a stable, uniform nonthermal plasma, it is difficult to obtain a plasma with these attributes at near atmospheric pressure. There are essentially two methods for producing nonthermal plasmas: corona discharge (CD) and DBD. Even though numerous applications rely on CD, this method is not convenient for volume gas-phase plasma processing. The DBD systems have several advantages, such as lower voltage consumption, current limitation to avoid transition to arc, a high-energy coupling of the DBD discharge, and low level of UV radiation emission [6].

Atmospheric plasmas can be used to treat macroscopic surfaces, by depositing thin films and/or altering the chemical composition of the surface. Micrometric surfaces in powders can also be modified using atmospheric plasmas. Reports in the literature have been focused on the treatment of granular material using a combination of plasma discharge and some type of powder fluidization. A circulating fluidized bed, which belongs to a fast fluidization regime, has been reported as a plasma reactor both for low-pressure [7], [8] and atmospheric [9]–[11] plasmas. Fluidized beds provide low-temperature and low-pressure gradients at high gas velocity, and therefore cohesive powders can be dispersed favorably [11]. Plasma treatment of powder surfaces could change the macroscopic behavior in products that utilize these treated powders as ingredient or raw material, such as paints, food products, pharmaceutical products, cement, concrete structures, tires, and many other finished products. In this paper, the results obtained from the surface modification treatment by atmospheric plasma of both organic and inorganic cohesive powders are presented. The powders were treated in a small-scale coaxial (COAX) DBD reactor designed and built in our laboratory for this purpose and operating in the experimental loop shown in Fig. 1.

The COAX-DBD operates as a batch fluidized-bed reactor to allow contact between the atmospheric plasma discharge and the granular material. Fluidization occurs when the solid particles are suspended in a container using a continuously upward flowing fluid (gas in the case of this paper). Solid

Manuscript received November 4, 2017; revised March 5, 2018; accepted April 3, 2018. This work was supported by the Instituto Politécnico Nacional, México under Internal Grant SIP-20170182. The review of this paper was arranged by Senior Editor S. J. Gitomer. (*Corresponding author: Martín de Jesús Nieto-Pérez.*)

The authors are with CICATA-IPN Querétaro, Instituto Politécnico Nacional, Santiago de Querétaro 76090, México (e-mail: m.nieto@ieec.org).

Color versions of one or more of the figures in this paper are available online at <http://ieeexplore.ieee.org>.

Digital Object Identifier 10.1109/TPS.2018.2824825

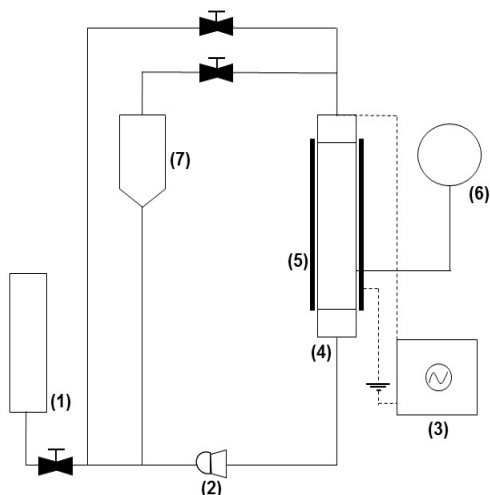


Fig. 1. Reactor setup. 1—Gas source. 2—Centrifugal blower. 3—RF power supply. 4—Fluidized-bed reactor. 5—High-voltage electrode. 6—Particle dispenser. 7—Cyclone.

powder particles are suspended through the fluid [12]. The attainment of these fluidization conditions is closely related to the intrinsic properties of the particles being fluidized including density, shape, size distribution, and surface characteristics [13]. Depending on these properties and the density difference between the particles and the fluid, the powders will fluidize differently, and the behavior falls into one of the four groups in the Geldart classification: A, B, C, or D [14]. Type-A powders have particles ranging from 30 to 125 μm and particle densities of about 1.5 kg/m^3 ; particles in this group tend to fluidize easily. Type-B powders have particles sizes ranging from 150 to 1000 μm and also tend to fluidize easily [14]. Because of their ease of fluidization, there is a lot of research and application for these two types of powders.

Type-C powders are also known as fine powders or cohesive powders; the particles that compose these powders are small and show noticeable cohesion and adhesion among themselves and with any surrounding surface [13]. Type-D group of powders includes those containing large and very dense particles; the gas flow requirement for fluidization of these powders is very large, and solid mixing is relatively poor [14].

Starch is a polysaccharide stored in plants and other biological sources in different forms. Like any other organic material, starch has a high biodegradability potential [7]. There is a growing interest in developing and studying modified starches for many industrial applications as they could be used as a biodegradable alternative to synthetic polymers [15]. Starch consists of two polymers of different structure: amylose and amylopectin. The relative amount of each polymer and the physical organization in the granule structure give specific physicochemical and functional properties to the starch [16]. The gelatinization process, which involves heating the starch granules in the presence of water, generates molecular disorganization which is highly sensitive to starch composition. The gelatinization process causes irreversible changes in starch properties such as swelling, granular disruption, crystal melting, loss of birefringence, and amylose leaching [16], [17]. For the development and production of starch-based materials,

TABLE I
OPERATION PARAMETERS DURING PLASMA TREATMENT OF POWDERS

Powder	ID	Solvent	Vapor pressure (kPa)	Flux into bubbler (cm^3/s)	Total flux (cm^3/s)
Potato starch	1	Acetone	31.1	0.705	2.77
	2	HMDSO	5.35	0.121	2.82
	3	Methanol	17.4	0.395	3.04
Titanium dioxide	1	Acetone	31.1	0.132	1.22
	2	HMDSO	5.35	0.023	1.11
	4	Isopropanol	17.4	0.3	1.39

the plasma treatment for surface modification is a promising route for creating specific purpose starches [7].

Titanium dioxide is a nontoxic and environmentally satisfactory granular material, with vast industrial applications, ranging from pigments to environmental purposes [18]. There is a growing interest in treating this powder due to its important applications such as conversion of toxic wastes to benign materials via photocatalytic oxidation or reduction reactions [19]. There is a lack of information regarding the effect of atmospheric plasma treatment on the properties of this powder. For purposes of this paper, the effect of the plasma treatment on the settling dynamics of titanium dioxide powder suspended in water was selected as the property to be studied by turbidimetry.

In this paper, two powders, one type-A organic [potato starch (PS)] and one type-C inorganic (titanium dioxide), were subjected to plasma treatments using different solvents (Table I), and the behavior of properties closely associated with the surface modification was tested. For the starch, gelatinization and rheological properties were assessed, while for the titanium dioxide, the behavior of the powder in water suspension was evaluated. In both cases, the modification of powder surface due to plasma exposure was evident given the results of the experimental tests performed on the powders after plasma treatment.

II. MATERIALS AND METHODS

A. Test Powders

PS and titanium dioxide were selected as the test powders in this paper. PS is composed of 25% amylose and 75% amylopectin, and it is classified as a type-A powder. The powder used in this paper was obtained from National Starch, (San Juan del Río, Querétaro, México). To evaluate the effect of plasma treatment on the PS properties, calorimetric and rheological tests were performed using a differential scanning calorimetry (DSC)1 Mettler Toledo Calorimeter and an Anton Physica MCR 101 Rheometer, respectively.

The selected inorganic powder to test the developed COAX-DBD reactor was titanium dioxide (TiO_2) with 0.007-M purity, and it was obtained from Sigma Aldrich. This material falls in the type-C category of the Geldart classification of powders. Since original titanium dioxide has a very broad particle size distribution that adds complexity to the sedimentation measurements, the particle size distribution was narrowed passing the powder through a 500- μm

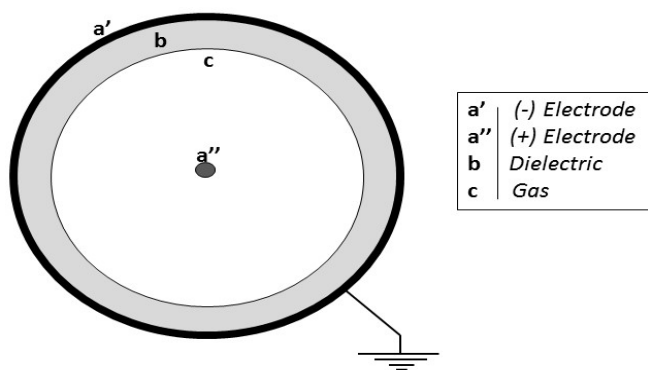


Fig. 2. DBD configuration used for the reactor, COAX-DBD.

sieve, followed by a 5-min separation process using gas flow to blow away very fine particles. After this process, size distribution was measured in a CILAS 1064 particle size analyzer.

B. COAX-DBD Reactor

The key tool in this paper is the COAX-DBD reactor operating in a circuit, as depicted in Fig. 1. The reactor consists of two coaxial electrodes separated by a quartz tube that serves both as reactor container and as dielectric barrier (b) between the electrodes, as shown in Fig. 2. The internal anode electrode (a'') is located at the center of the reactor and is fed with an alternating high voltage, while the cathode, constructed with a mesh (a') around the quartz tube, is always grounded. When gas is present in the interelectrode region (c), a filamentary atmospheric discharge is obtained in the space between the central bar electrode and the quartz tube. To obtain current flow in the discharge gap, the electric field intensity must be enough to breakdown the gas and achieve the plasma state [5], [6]. The reactor has two main circuits: the power circuit, which includes the radio frequency (RF) generator with a resonant circuit [20], and the gas handling circuit, which comprised the reactor and a system for gas delivery and recirculation.

The gas delivery system is divided into two parts: the first part consists on the entrance of the gas directly into the reactor, and a second part goes into a bubbler containing a liquid solvent column before entering the reactor. This is necessary to modify the surface with small amounts of organic vapor introduced in the reactor along with the inert gas carrier (argon), since molecular fragments and radicals formed in the plasma discharge from solvent molecules influence the powder surface modification. A portion of the carrier gas is diverted to be bubbled through a column of the solvent to be used as the “active ingredient” in the plasma discharge. To calculate the amount of solvent injected into the plasma reactor, it is assumed that the argon bubbles saturate with solvent vapor at ambient temperature.

The coaxial configuration described is a promising solution for treating powders with an atmospheric pressure plasma when combined with a fluidized bed. The reactor that consists of a COAX-DBD configuration combined with batch fluidization of particles [10], [11], [21] is named here a plasma

fluidized-bed reactor (PFBR). The main advantages of this type of reactor are a well-mixed material, good temperature control, and a close contact of solids with the active atmospheric plasma in a fluidized bed [21].

The general experimental procedure in this paper was as follows: a mass of powder was loaded in the PFBR powder holder; then, the mixture of argon and the solvent vapor was injected into the bottom of the reactor, until reaching the flow rate necessary for an adequate fluidization of the powder bed. At this point, the RF power was adjusted to start the discharge for 10 min at a voltage level of 12 kV_{pp} and a frequency of 25 kHz; finally, the powders were retrieved from the reactor. The particle losses due to particle drag were 32.04% and 43.82% for the PS and titanium dioxide powders, respectively. For the titanium dioxide, the particle separation process prior the treatment was considered to calculate the loss rate. Table I shows the operation values used for the treatments and the solvent species used in each powder. The vapor pressure of the solvent at room temperature, the percent of flow diverted to the bubbler, and the total flow of Ar into the reactor are included in Table I. Volumetric mass flow is important in order to determine the velocity U used for the powders to achieve fluidization. Pressure is important due to the capability of the reactor to handle different powder sizes and solvent types.

C. Fluidization

The particle size in type-C powders is typically lower than 30 μm , and they are very difficult to fluidize [14]. To achieve the fluidization state in this type of powder, the use of distributors, baffles, microjets, mechanical vibration, etc., is required [12], [14]. There are two methods for improving the fluidization of type-C powders; one is the application of an external force, such as vibration, magnetic field, and acoustic field, and the other involves the modification of intrinsic properties of the particles [22] or mixing with other particles with different sizes or shapes [13], [23].

According to the fluidization theory developed by Abrahamson and Geldart [24], the relevant powder physical properties for this work are: the mean particle size d_p , the particle density ρ_p , powder bed voidage ϵ , the minimum fluidization velocity U_{mf} , the minimum bubbling velocity U_{mb} , and the maximum nonbubbling bed expansion ratio H_{mb}/H_{mf} .

To determine an average value for d , a CILAS 1064 particle size analyzer was used. To approximate ρ_p , the mass of compacted powder contained on a 10-mL volumetric flask was measured using an Ohaus Model Voyager Analytical Balance. To account for nonspherical particle shape, the values of the surface volume diameter d_{sv} and volume diameter d_v were calculated with the following equations:

$$d_{sv} = 0.871d_p \quad (1)$$

$$d_v = 1.127d_p. \quad (2)$$

The sphericity of the powders was calculated with the following equation:

$$\psi = \frac{d_{sv}}{d_v}. \quad (3)$$

The bed voidage was calculated with the following equation:

$$\epsilon = 1 - \frac{W}{\rho_p V} \quad (4)$$

where W is the total powder bed mass and V is the powder bed volume of the powder. The minimum bubbling velocity is given by the following equation:

$$U_{mb} = 2.07 \exp(0.71F) \frac{d_p \rho_g^{0.06}}{\mu^{0.347}} \quad (5)$$

where F represents the powder fraction with a size much lower than d_p , and it is obtained from the size distribution measurements in the particle size analyzer. Equation (5) is very useful for obtaining values of U_{mb} when using carrier gases other than air.

The maximum nonbubbling bed expansion ratio H_{mb}/H_{mf} was calculated with the following equation:

$$\frac{H_{mb}}{H_{mf}} = \frac{5.50 \exp(0.158F) \rho_g^{0.028} \mu^{0.115}}{d_p^{0.176} g^{0.205} (\rho_p - \rho_g)^{0.205}} \quad (6)$$

The minimum fluidization velocity was calculated using the following equation, for particles with $d_p < 100 \mu\text{m}$ [25]:

$$U_{mf} = \frac{(\rho_p - \rho_g)^{0.934} g^{0.934} d_p^{1.8}}{1100 \mu^{0.87} \rho_g^{0.066}} \quad (7)$$

where ρ_g is the carrier gas density evaluated at the operating conditions, g is the gravity acceleration, and μ is the gas viscosity.

D. Particle Shape and Size Distribution Measurements

Two complementary experimental techniques were utilized to determine size, shape, and size distribution of the powders used in this paper: scanning electron microscopy and a light-scattering-based technique.

The titanium dioxide and PS untreated powders were analyzed using a scanning electron microscope (Phenom Pro Generation 5, PhenomWorld). Completely dried samples were deposited in a sample holder with electrically conductive carbon double-sided tape. Samples were observed at 5 and 10 kV.

Particle size distribution was measured in triplicate using a granulometer (CILAS 1640, Marcoussis, France) based on the light scattering. A laser beam illuminates the region where the particles are suspended, and a photodetector array provides the angular dependence of the scattered light [26]. The scattered patterns can be transformed into particle size distributions using different models. Since for PS, most granules have an approximate spherical shape, the Mie theory was applied as a first approximation. When the particles are not as spherical as titanium dioxide, the results should be interpreted through effective diameters that depend on the details of the geometry of the particles [27].

E. Gelatinization and Rheology Tests on Starch Powders

The pasting profile of starch dispersions at 5% solid content was measured by rotational test using a rheometer (Anton Paar Physica MCR 101) with two parallel 25-mm diameter circular

plates (upper plate—sandblasted), separated by a 1000- μm gap. A heating or cooling rate of 5 $^\circ\text{C}/\text{min}$ and a shear rate of 50 s^{-1} were used. The edge of the parallel plates was completely covered with mineral oil to avoid water evaporation during the test. The rheometer was programmed for running time sweeps of the heating cycles from 25 $^\circ\text{C}$ to 90 $^\circ\text{C}$, holding for 5 min, cooling to 25 $^\circ\text{C}$, and maintaining for 5 min before applying three measurement cycles. The first cycle up going from 0.01 to 100 s^{-1} , and the second and third cycles going from 100 to 0.01 s^{-1} . Since starch is a non-Newtonian fluid, the shear stress as a function of velocity is assumed to follow the Ostwald-de Waele equation:

$$\tau_{xy} = K \left(\frac{\partial u_x}{\partial y} \right)^n \quad (8)$$

From the rheometer experimental data, performed in triplicate, values for the consistency index K ($\text{Pa} \cdot \text{s}^n$) and the flow behavior index n (dimensionless) can be obtained. The results from these calculations were used to define the flow behavior [28], [29].

The thermal properties of starch gelatinization were measured using a differential scanning calorimeter (Model 822E, Mettler Toledo) calibrated with indium. Starch gelatinization was evaluated using the following method [30]: 2 mg of starch sample (dry basis) was weighed in a 40- μL aluminum pan and 7 μL of deionized water were added to the powder. The pan was hermetically sealed and allowed to stand for 1 h before analysis. An empty aluminum pan was used as a reference. The sample was heated from 30 $^\circ\text{C}$ to 110 $^\circ\text{C}$ at 10 $^\circ\text{C}/\text{min}$. The starting gelatinization temperature (T_0), the peak temperature (T_p), the final gelatinization temperature (T_c), and the gelatinization enthalpy change (ΔH) were computed using the calorimeter's built-in software.

F. Sedimentation Dynamics Tests on Titanium Dioxide Powders

The effect of the plasma treatment on the sedimentation properties of titanium dioxide suspended in water was observed using a turbidimeter based on the light-scattering signals. This technique, when used for the particle size analysis, has some advantages over other optical experimental techniques; it is fast, easy to implement, noninvasive, and in real time. A method to determine the particle size distribution from two turbidimetry measurements has been reported in [31]; in that work, two light-scattering parameters are combined: the turbidimetry ratio and the rate at which turbidimetry changes with wavelength. The turbidity of a suspension of particles τ measures the reduction of the transmitted beam intensity due to scattering [31].

The optical array shown in Fig. 3 was used to quantify the scattered light by a liquid sample held in a square quartz cuvette. The source of probing light is a semiconductor red laser beam, modulated at 1 kHz.

The detector array consists of four sensors: one used to measure the reference beam and three located around a rectangular sample container (quartz cuvette). The sensors around the sample were arranged as follows: one sensor was placed to measure the transmitted light across the cuvette (I_{0° in Fig. 3).

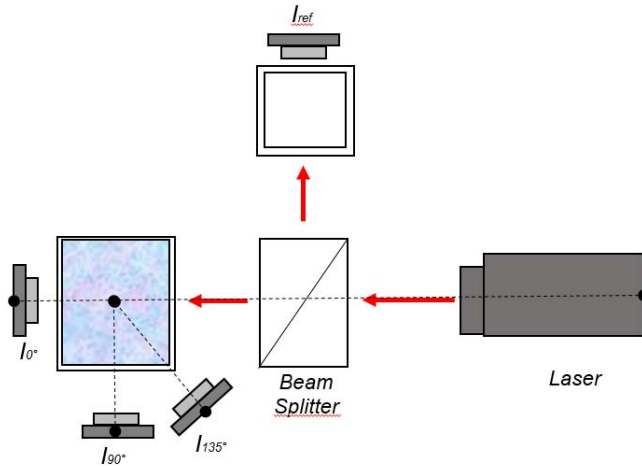


Fig. 3. Optical arrangement used for the turbidimetry tests performed to titanium dioxide powders.

TABLE II
PHYSICAL PROPERTIES OF THE POWDERS

Property	Potato starch	Titanium dioxide
d_p (μm)	44.05	3
d_v (μm)	49.64	3.4
d_{sv} (μm)	38.37	2.61
ψ , -	0.77	0.77
ρ_p (kg/m^3)	967.44	831.9
ϵ , -	0.1115	0.3112

A second sensor was located at 90° from the beam pathway to measure right-angle scattered light coming from the cuvette (I_{90° in Fig. 3), which significantly decreases the signal-to-noise ratio [32]. Finally, a third sensor detected the backscattered light in the sample (I_{135° in Fig. 3), which is a small signal when the turbidity of the sample is low enough. The reference sensor (I_{ref} in Fig. 3) monitored an identical cuvette containing pure solvent, and its signal was used to normalize the obtained data and eliminate any fluctuations associated with laser variation intensity. The signals from the four detectors were processed using an SRS850 lock-in amplifier, and signals were acquired with a National Instruments data acquisition device. The complete experimental setup was operated using LabVIEW software.

III. RESULTS AND DISCUSSION

A. Determination of Fluidization Conditions

Based on the fluidization theory described in Section II, some of the powder properties relevant to establish the type of fluidization regime and determine flow velocity ranges are summarized in Table II. These parameters are important for the initial fluidization process, as mentioned previously. It is important to consider that preliminary fluidization tests are obtained only by visual observation [12], [13], that is, measuring the flow of gas entering the reactor and observing the behavior of the powder.

TABLE III
FLUIDIZATION PARAMETERS DURING THE EXPERIMENTS FROM TABLE I

Powder	Treatment	U_{mf} (cm/s)	U (cm/s)	U_{mb} (cm/s)	H_{mf}/H_{mb}
Potato starch	1	5.79×10^{-3}	2.91	0.343	2.4765
	2	3.20×10^{-2}	2.96	0.444	1.9963
	3	1.41×10^{-2}	3.25	0.125	2.2921
TiO_2	1	3.72×10^{-5}	1.28	0.334	4.5141
	2	1.37×10^{-4}	1.17	0.432	3.5836
	4	2.92×10^{-5}	1.46	0.241	4.4289

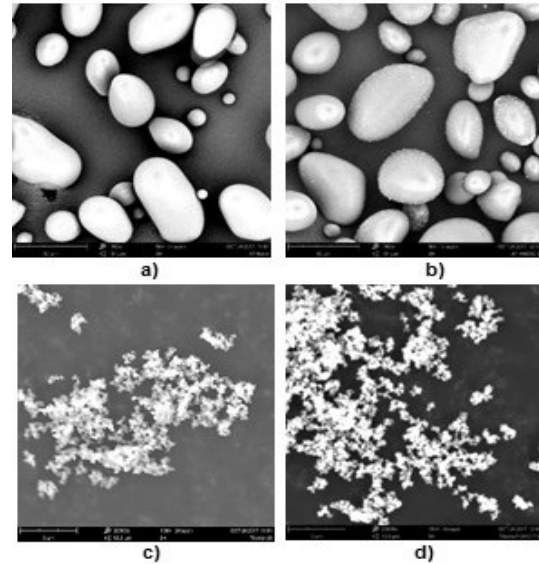


Fig. 4. SEM images for (a) untreated PS, 1500 \times , (b) HMDSO plasma-treated PS, 1500 \times , (c) untreated titanium dioxide ultrasonicated, 15000 \times , and (d) HMDSO plasma-treated and ultrasonicated titanium dioxide, 15000 \times .

The importance of d_p relies on determining if the fluidization powder behavior is possible. With this information, the proper parameters can be adjusted in the reactor. Properties d_v and d_{sv} were calculated for the two powders to obtain the ratio d_v/d_{sv} , giving the particle sphericity ψ . As shown in Table II, both powders have a value of 0.77 for the sphericity, which corresponds to a rectangular parallelepiped shape. With this information, the ideal sphere shape model to obtain fluidization conditions is discarded. Taking this in consideration, the calculations performed here were done for the case of nonspherical particles.

In Table III, the fluidization properties are presented for the two powders used in the experiments. The gas velocity U is determined experimentally by measuring the volumetric flow rate into the reactor and dividing by the cross-sectional area of the powdered bed. The minimum bubbling velocity U_{mb} is the value that determines where bubbles first appear and is determined using (6). On the other hand, the minimum fluidization velocity U_{mf} is the minimum velocity the particles need to break the resting starting position and is calculated using (7) with the values from Table II.

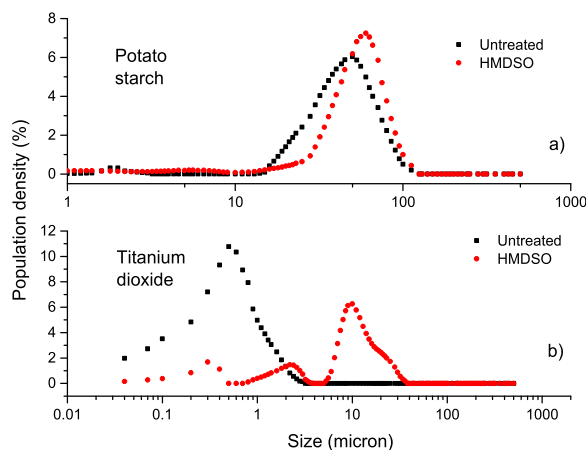


Fig. 5. Granulometry results for (a) untreated and HMDSO plasma-treated PS and (b) untreated and HMDSO plasma-treated titanium dioxide (TiO_2) powders.

B. SEM and Size Distribution Characterization

Images from SEM were taken to observe the changes in PS granules, and titanium dioxide particles after plasma treatment 2, as shown in Table I, using Hexamethyldisiloxane (HMDSO) as the solvent and are presented in Fig. 4. Untreated PS granules [Fig. 4(a)] showed two granule sizes: small with circular shape and big with oval shape in the SEM images [33]. In treated granules [Fig. 4(b)], the formation of deposits on the granule surface can be appreciated in the micrographs, which show up as small speckles in the surface. Such deposits are probably due to the interaction of the granules with the Ar/HMDSO plasma. The high-temperature electrons in the plasma have the capability to break bonds in the molecule, generating free radicals; these radicals will hit or stick to any available surface in an effort to lower their energy, leading to surface mechanical damage or polymerization processes that may form films or deposits in the surface of the granules [34], [35].

For the titanium dioxide, being a cohesive powder, particle size is fundamental to analyze the fluidization and sedimentation behavior. Fig. 4(c) shows a sample of titanium dioxide powder before treated by plasma that still contains agglomerates of very fine particles after ultrasonication process to break up them. This process is required before the sample treatment in the fluidized-bed reactor, as mention in Section II-A, and also for measurements in the turbidimetry array [36]. After ultrasonication, the titanium dioxide sample was treated in the PFBR. An image of a treated powder sample is shown in Fig. 4(d) after ultrasonic process. The image scale shows that particles have diameters on the order of micrometer.

In the case of granulometry measurements, plots of particle size distributions for the untreated and plasma-treated PS and titanium dioxide powders are shown in Fig. 5.

In the case of PS, a slight change in size distribution due to particle losses during PFBR process was observed, specially the small ones [Fig. 5(a)]. The particle size for untreated titanium dioxide shows a size distribution peak between

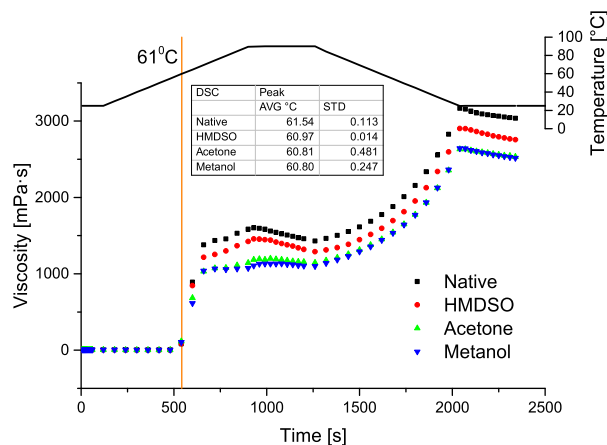


Fig. 6. Rheometry tests for the untreated PS and PS exposed to Ar-methanol, Ar-HMDSO, and Ar-acetone plasmas.

0.5 and 0.6 μm , and it is consistent with the SEM images in Fig. 4(c). This means that although the ultrasonication improves significantly the particles size distribution, some small agglomerates cannot be broken by physical treatments such as ultrasonication.

However, this agglomeration increased by the PFBR [Fig. 5(b)], and the granule size around an average of $d_p = 3 \mu\text{m}$ should be considered in the fluidization models. Also, the particle shape should be adjusted as a porous particle instead of a spherical particle since it is a heterogeneous agglomerate of nanometric particles observed in Figs. 4(d) and 5(b).

C. Effect of Plasma Treatments on the DSC and Rheology Behavior of Potato Starch

Fig. 6 shows the rheological behavior of PS for each plasma treatment. DSC values are shown in the inset. On the paste formation test, in which the starch gelatinization process is followed, the granules swell by absorbing water, and the amylose is leached into the medium allowing the formation of a viscous solution [37], [38]. For starches treated under the three types of plasma (Table I), differences were found between untreated and treated starches. All treated granules had lower viscosity. In the case of the plasma treatments of Ar-acetone and Ar-methanol, the changes in the viscosity profile were similar and greater than the case of Ar-HMDSO treatment. For all treatments, the reduction of viscosity respect to the native starch was significant. The decrease in viscosity during the heating of treated starches reflects the difficulty of the granules to reach a maximum swelling capacity, resulting in a structural change possibly due to mechanical or chemical modification promoted by plasma (cross-linking and/or depolymerization). During the cooling stage, both the untreated starch and the treated starches showed an increase in the viscosity values due to the reorganization of the components (amylose/amylopectin). The leached amylose plays an important role in the formation of paste, as also do the remaining granules (amylopectin) [17].

The results from the thermal analysis of both the untreated and treated starches are shown in the table inserted in Fig. 6.

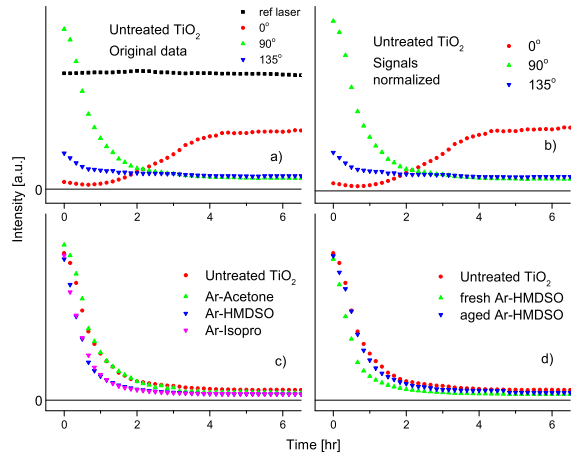


Fig. 7. TiO_2 suspensions' turbidimeter measurements. (a) Raw data from reference, 0° , 90° , and 135° detector signals. (b) Signals normalized to the reference detector. (c) Comparison between 90° detector signals for untreated (TiO_2) powder and treated with Ar-isopropanol, Ar-acetone, and Ar-HMDSO plasmas. (d) Comparison between the behaviors of untreated TiO_2 powder, freshly treated with Ar-HMDSO plasmas and aged (40 days) Ar-HMDSO plasma treated.

The temperature of gelatinization (T_p) showed a slight decrease as a function of the plasma treatments, being less for the plasma treatment of Ar-HMDSO, followed by treatment with Ar-acetone and finally the treatment of Ar-methanol. Similar behavior was observed in the viscosity profiles (Fig. 6). The slight decrease in the gelatinization temperature could be attributed to a depolymerization caused by the incorporation of plasma species, in particular molecular fragments of the HMDSO molecule, to the starch structure in the three treatments [39].

D. Effect of Plasma Treatments on the Sedimentation Dynamics of Titanium Dioxide–Water Suspensions

To evaluate the effect of plasma surface treatment on the settling behavior of the powder suspended in water, turbidimetry measurements were performed to characterize the evolution of the sedimentation process. In Fig. 7(a), raw data taken from the light sensors at 0° , 90° , and 135° (Fig. 3) around the sample as a function of time are presented for suspensions made with untreated titanium dioxide powder. The black line represents the reference sample cell that contains the pure solvent. To avoid the effect of possible laser intensity fluctuations, data were normalized point by point using this reference signal. The normalized data are shown in Fig. 7(b).

Comparing data from all sensors, the sensor measuring scattered light at 90° produced the most stable signal, so it was used to analyze the effect of plasma treatment on each powder sample. Fig. 7(c) presents a comparison between the treated and untreated titanium dioxide sedimentation behavior. As time increases, the normalized scattered light decreases approaching to a constant value as $t \rightarrow \infty$; instead, the scattered light intensity approaches a constant value. This behavior is because the sample contains very small particles (Fig. 5), which are stable enough to be suspended in the media for very long times ($t \rightarrow \infty$). The constant turbidity value when $t \rightarrow \infty$ could be estimated based on the granulometry data of

TABLE IV
FITTING PARAMETERS FOR THE EXPONENTIAL DECAY OF SCATTERED LIGHT SIGNAL INTENSITY DURING TITANIUM DIOXIDE POWDER SETTLING

Parameter	Untreated	Ar-Acetone	Ar-Isoprop.	Ar-HMDSO
I_0	0.659	0.720	0.677	0.647
I_∞	0.031	0.032	0.028	0.027
w_1	0.08	0.08	0.08	0.08
w_2	0.32	0.32	0.32	0.32
w_3	0.37	0.37	0.37	0.37
w_4	0.23	0.23	0.23	0.23
β_1	1.260	1.008	1.706	1.747
β_2	1.248	1.006	1.706	1.748
β_3	1.249	1.006	1.706	1.747
β_4	1.248	1.007	1.706	1.747

each treatment, and in this paper, it is designated as I_∞ for the sedimentation analysis of the powder samples. As shown in Fig. 7(c), the plasma treatments (Table I) with HMDSO and isopropanol slightly increased the time constant in the exponential decay behavior observed in the scattering signal. To quantify this effect in the settling behavior, an exponential decay model was proposed and adjusted to the experimental data to compare the model parameter values resulting from each treated sample. The model is given by the following equation:

$$I(t) = I_\infty + (I_0 - I_\infty) \sum_{i=1}^4 w_i e^{-\beta_i t}. \quad (9)$$

Equation (9) represents a model where the overall decay in the 90° scattered light signal is produced by the superposition of four exponential decays, each with a weight w_i . By using this model, the effect of a broad particle size distribution can be taken into account, since particles with different sizes will settle at different speeds and the parameter β_i will be different for each particle population in the sample. If the particle size distribution function for the powder is available, the particles can be separated into size ranges and the values of each w_i (probability of finding a particle in the size range i) can be obtained for the four defined size ranges. The parameter I_0 is the signal intensity at the beginning of the experiment, and I_∞ was defined previously as the residual scattering intensity due to colloid formation. A nonlinear fitting tool was used to estimate the values of the free parameters β_i .

For titanium dioxide powder used in these experiments, and considering the granulometric information from Fig. 5, the four particle size ranges defined were: from 40 to 100 nm, from 101 to 500 nm, from 501 to 1000 nm, and larger than 1000 nm. The values for the model parameters for each of the curves in Fig. 7(c) are presented in Table IV. The only free parameters are the exponential decay time constants β_i . From Table IV, two important observations can be made: the first is that the four values of β_i are the same for each treatment, indicating that the decay is adequately described by a single exponential; hence, a small particle size effect exists for the size ranges defined for this analysis.

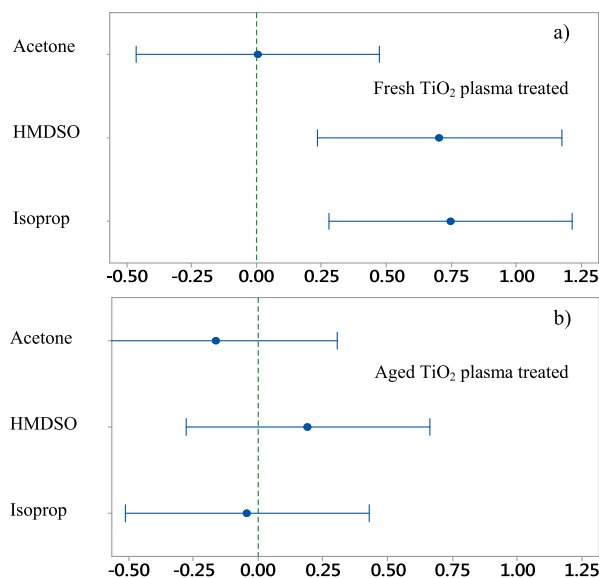


Fig. 8. Confidence interval Dunnett's multiple comparison graphics. (a) Fresh TiO_2 plasma treated with three solvents acetone, HMDSO, and isopropanol. (b) Aged TiO_2 plasma (40 days). The dotted line represents the untreated titanium dioxide coefficient. For the samples and aged (40 days) TiO_2 plasma-treated samples.

The second observation is that different treatments give different values of β_i , something that was already hinted by the curves in Fig. 7(c). To verify that the differences in the value of this parameter are due to the treatment, the exponential coefficients of treated and untreated samples were compared using a Dunnett test and the results are shown in Fig. 8. From Fig. 8(a), the titanium dioxide treated with Ar-acetone plasma (labeled A) is not statistically different from the untreated samples (confidence interval includes the zero mark). In contrast, the coefficients of samples treated with Ar-HMDSO (H) and Ar-isopropanol (I) plasmas indicate a statistically significant difference; since their values for time constant are larger, the particle sedimentation rate is faster, confirming the trend observed in Fig. 7(c).

To assess the effect of the environmental condition on the treated powders, titanium dioxide samples treated with the three types of plasmas were exposed to the environment during 40 days at room lab conditions [40]–[42]. To quantify a change in the settling rate between the freshly treated and aged plasma-treated particles, the model in (9) was used to obtain the β coefficients for the aged samples. Fig. 7(d) shows a comparison between the settling behaviors for fresh and aged plasma-treated particles with Ar-HMDSO. Qualitatively, the aged samples modified their settling rate when compared to the samples with a fresh treatment, and in this case, all the coefficients tend to match the untreated titanium dioxide behavior. This means that the sedimentation rate is the same for all the samples (untreated and treated after 40 days exposure to environment), something that was also revealed by the Dunnett test shown in Fig. 8. If an interval does not contain zero, the corresponding mean is significantly different from the untreated TiO_2 . This behavior could support the hypothesis that the plasma particle surface modification is not permanent and can be degraded or modified by simple

exposure to ambient air, implying that in order to preserve the effect of plasma, the titanium dioxide particles should be suspended in the target media immediately after treatment, before degradation occurs. Future experiments will be made to explore the coating degradation rate under standard conditions.

IV. CONCLUSION

A PFBR was constructed, and its capability to modify the surface of organic and inorganic powders was demonstrated with PS and titanium dioxide powders. Treated particles suffered alterations in their surface due to the plasma treatment inside the reactor developed to carry out this work. The results proved that a fluidized bed allowed achieving a surface modification, resulting in important changes in the behavior of the powders. Even for fine powders such as titanium dioxide, the reactor showed proper operation. The design of the reactor helped to achieve the required fluidization state.

SEM images showed visual modification in the starch granules due to the plasma exposure. Rheometry and DSC results showed a significant alteration in the PS. The deposits on the surface of granules are an indicator of the modification capability of the plasma treatment. The modification is promoted by the treatment conditions in which an especial route of reaction in the plasma is favored, promoting the formation of deposits on the surface, alteration of structural components of the granule, and potential cross-linking and depolymerization. These changes result in the decrease of the viscosity pattern and a gelatinization taking place at lower temperatures.

Turbidimetry measurements on titanium dioxide indicate that it took at most 5 h for the particles to settle when suspended in water and a residual turbidity appeared in water due to the presence of very fine particles forming a stable colloid. Particle sedimentation curves could be separated in two groups: untreated powder and Ar-acetone plasma treatment had similar settling behavior, while particles treated with Ar-HMDSO and Ar-isopropanol plasmas sedimented faster. There was no significant effect of particle size distribution, since larger particles were removed prior to treatment and the sedimentation kinetics could be described by a single exponential decay in the scattered light signal over time. After prolonged exposure to the environment, the plasma modification effect was lost, and the particles recovered their original settling behavior. This effect will be further explored in detail for future work.

ACKNOWLEDGMENT

The authors would like to thank the M. A. H. Martínez for his technical assistance in the optical arrangement for turbidimetry tests.

REFERENCES

- [1] D. Merche, N. Vandecasteele, and F. Reniers, "Atmospheric plasmas for thin film deposition: A critical review," *Thin Solid Films*, vol. 520, no. 13, pp. 4219–4236, 2012.
- [2] M. Nitschke, *Polymer Surfaces and Interfaces*. Berlin, Germany: Springer-Verlag, 2008.
- [3] R. A. Wolf, *Atmospheric Pressure Plasma for Surface Modification*. Hoboken, NJ, USA, Wiley, 2013.

- [4] J. Y. Rico-Ruíz, "Evaluación del efecto del tratamiento con plasma frío en los compuestos volátiles de sabor de nuez pecana (*Carya illinoensis*)," M.S. thesis, Inst. Politécnico Nacional, Mexico City, Mexico, 2014.
- [5] U. Kogelschatz, "Dielectric-barrier discharges: Their history, discharge physics, and industrial applications," *Plasma Chem. Plasma Process.*, vol. 23, no. 1, pp. 1–46, 2003.
- [6] B. Pashaie, S. K. Dhali, and F. I. Honea, "Electrical characteristics of a coaxial dielectric barrier discharge," *J. Phys. D, Appl. Phys.*, vol. 27, no. 10, p. 2107, 1994.
- [7] S. Khorrarn, M. S. Zakerhamidi, and Z. Karimzadeh, "Polarity functions' characterization and the mechanism of starch modification by DC glow discharge plasma," *Carbohydrate Polym.*, vol. 127, pp. 72–78, Aug. 2015.
- [8] F. Zhu, "Plasma modification of starch," *Food Chem.*, vol. 232, pp. 476–486, Oct. 2017.
- [9] S. H. Jung, S. H. Park, D. H. Lee, and S. D. Kim, "Surface modification of HDPE powders by oxygen plasma in a circulating fluidized bed reactor," *Polym. Bull.*, vol. 47, no. 2, pp. 199–205, Oct. 2001.
- [10] C. Roth, Z. Künsch, A. Sonnenfeld, and P. R. von Rohr, "Plasma surface modification of powders for pharmaceutical applications," *Surf. Coat. Technol.*, vol. 205, pp. S597–S600, Jul. 2011.
- [11] S. H. Jung, S. M. Park, S. H. Park, and S. D. Kim, "Surface modification of fine powders by atmospheric pressure plasma in a circulating fluidized bed reactor," *Ind. Eng. Chem. Res.*, vol. 43, no. 18, pp. 5483–5488, 2004.
- [12] J. M. V. Millán, *Fluidization of Fine Powders*, vol. 18. Amsterdam, The Netherlands: Springer, 2013.
- [13] Z. Wang, M. Kwauk, and H. Li, "Fluidization of fine particles," *Chem. Eng. Sci.*, vol. 53, no. 3, pp. 377–395, 1998.
- [14] D. Geldart, "Types of gas fluidization," *Powder Technol.*, vol. 7, no. 5, pp. 285–292, 1973.
- [15] G. A. Arolkar, M. J. Salgo, V. Kelkar-Mane, and R. R. Deshmukh, "The study of air-plasma treatment on corn starch/poly(ϵ -caprolactone) films," *Polym. Degradation Stability*, vol. 120, pp. 262–272, Oct. 2015.
- [16] J. A. Medina and J. C. Salas, "Caracterización morfológica del granulo de almidón nativo: Apariencia, forma, tamaño y su distribución," *Revista Ingeniería*, vol. 27, pp. 56–62, May 2008.
- [17] M. G. Casarrubias-castillo, G. Méndez-montealvo, S. L. Rodríguez-ambriz, M. M. Sánchez-Rivera, and L. A. Bello-Pérez, "Diferencias estructurales y reológicas entre almidones de frutas y cereales," *Agrociencia*, vol. 46, no. 5, pp. 455–466, 2012.
- [18] L. Jezerska, J. Hlosta, M. Zidek, J. Zegzulka, J. Necas, and K. M. Kutlakova, "Comparative study of titanium dioxide's rheological properties," in *Proc. NANOCON*, 2014, pp. 1–6.
- [19] J. H. Cho, "RF pulsed plasma surface modification of titanium dioxide nanoparticles for environmental applications," Ph.D. dissertation, Univ. Texas, Austin, TX, USA, 2005.
- [20] L. S. Ruvalcaba, "Desarrollo de un sistema para generación de plasma basado en una descarga de barrera dieléctrica coplanar," M.S. thesis, Instituto Politécnico Nacional, Mexico City, Mexico, 2014, p. 91.
- [21] C. R. Wierenga and T. J. Morin, "Characterization of a fluidized-bed plasma reactor," *AIChE J.*, vol. 35, no. 9, pp. 1555–1558, 1989.
- [22] Y. Chen, J. Yang, R. N. Dave, and R. Pfeffer, "Fluidization of coated group C powders," *AIChE J.*, vol. 54, no. 1, pp. 104–121, 2008.
- [23] Z. L. Wang, "Fluidization of fine particles and the effects of additive particles," Ph.D. dissertation, Inst. Chem. Metallurgy, Acad. Sinica, Beijing, China, 1995.
- [24] A. R. Abrahamsen and D. Geldart, "Behaviour of gas-fluidized beds of fine powders part I. Homogeneous expansion," *Powder Technol.*, vol. 26, no. 1, pp. 35–46, 1980.
- [25] D. K. Ram, "The determination of minimum bubbling velocity, minimum fluidization velocity and fluidization index of fine powders (Hematite) using gas-solid tapered beds," *Int. J. Sci. Res.*, vol. 2, no. 2, pp. 287–293, 2013.
- [26] C. F. Bohren and D. R. Huffman, Eds., *Absorption and Scattering of Light by Small Particles*. Weinheim, Germany: Wiley, 1998.
- [27] O. Paredes-López, L. A. Bello-Pérez, and M. G. López, "Amylopectin: Structural, gelatinisation and retrogradation studies," *Food Chem.*, vol. 50, no. 4, pp. 411–417, Jan. 1994.
- [28] A. Tecante and J. L. Doublier, "Steady flow and viscoelastic behavior of crosslinked waxy corn starch-k-carrageenan pastes and gels," *Carbohydrate Polym.*, vol. 40, no. 3, pp. 221–231, 1999.
- [29] J. F. Steffe, *Rheological Methods in Food Process Engineering*. Detroit, MI, USA: Freeman, 1996.
- [30] A. Herrera-Gómez, M. Canónico-Franco, and G. Ramos, "Aggregate formation and segregation of maize starch granules cooked at reduced moisture conditions," *Starch/Stärke*, vol. 57, no. 7, pp. 301–309, 2005.
- [31] D. H. Melik and H. S. Fogler, "Turbidimetric determination of particle size distributions of colloidal systems," *J. Colloid Interface Sci.*, vol. 92, no. 1, pp. 161–180, 1983.
- [32] A. F. B. Omar and M. Z. B. Matjafri, "Turbidimeter design and analysis: A review on optical fiber sensors for the measurement of water turbidity," *Sensors*, vol. 9, no. 10, pp. 8311–8335, 2009.
- [33] J. Jay-Lin, "Structural features of starch granules II," in *Starch Chemistry and Technology*. Burlington, MA, USA: Academic, 2009, pp. 193–236.
- [34] J. Friedrich, "Mechanisms of plasma polymerization—Reviewed from a chemical point of view," *Plasma Process. Polym.*, vol. 8, no. 9, pp. 783–802, 2011.
- [35] H. Kobayashi, A. T. Bell, and M. Shen, "Plasma polymerization of saturated and unsaturated hydrocarbons," *Macromolecules*, vol. 7, no. 3, pp. 277–283, 1974.
- [36] Y. Zhao, M. Wang, Y. Liu, and H. Cui, "Redispersity/solubility of nanopowder in solvents," *Recent Patents Nanotechnol.*, vol. 8, pp. 18–30, Jan. 2014.
- [37] P. J. Jenkins and A. M. Donald, "Gelatinisation of starch: A combined SAXS/WAXS/DSC and SANS study," *Carbohydrate Res.*, vol. 308, nos. 1–2, pp. 133–147, 1998.
- [38] J. Carlstedt, J. Wojtasz, P. Fyhr, and V. Kocherbitov, "Understanding starch gelatinization: The phase diagram approach," *Carbohydrate Polym.*, vol. 129, pp. 62–69, Sep. 2015.
- [39] R. Thirumdas, A. Trimukhe, R. R. Deshmukh, and U. S. Annature, "Functional and rheological properties of cold plasma treated rice starch," *Carbohydrate Polym.*, vol. 157, pp. 1723–1731, Feb. 2017.
- [40] S. Swaraj, U. Oran, A. Lippitz, J. F. Friedrich, and W. E. S. Unger, "Aging of plasma-deposited films prepared from organic monomers," *Plasma Process. Polym.*, vol. 4, pp. 784–789, Apr. 2007.
- [41] M. Drabik, J. Kousal, C. Celma, P. Rupper, H. Biederman, and D. Hegemann, "Influence of deposition conditions on structure and aging of C:H:O plasma polymer films prepared from acetone/CO₂ mixtures," *Plasma Process. Polym.*, vol. 11, no. 5, pp. 496–508, 2014.
- [42] T. M. El-Agez, D. M. Wieliczka, C. Moffitt, and S. A. Taya, "Aging of oxygen-treated trimethylsilane plasma-polymerized films using spectroscopic ellipsometry," *J. Atom. Mol. Opt. Phys.*, vol. 2011, Aug. 2011, Art. no. 295304, doi: 10.1155/2011/295304.



Enrique Augusto García-Guerrero received the B.Sc. degree in physics engineering from the Universidad Autónoma de San Luis Potosí, San Luis Potosí, México, in 2017. He is currently pursuing the M.Sc. degree in advance technology with CICATA-IPN Querétaro, Instituto Politécnico Nacional, Santiago de Querétaro, México.

He is currently a Research Assistant with CICATA-IPN Querétaro, Instituto Politécnico Nacional. His current research interests include atmospheric plasma coating applications and plasma technology.

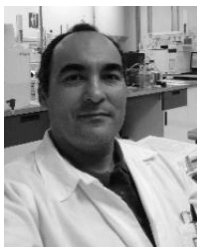


Martín de Jesús Nieto-Pérez (M'04–SM'14) received the B.S. degree in chemical engineering from Universidad Autónoma Metropolitana, Ciudad de México, México, in 1997, and the M.S. and Ph.D. degrees in nuclear engineering from the University of Illinois at Urbana-Champaign, Champaign, IL, USA, in 2001 and 2004, respectively.

He was a Fulbright Scholar for the master's degrees from 1998 to 2000. He was a Post-Doctoral Associate with the Argonne National Laboratory, U.S. Department of Energy, Lemont, IL, USA, from

2004 to 2006. Since 2008, he has been a tenured Professor with the Centro de Investigación en Ciencia Aplicada y Tecnología Avanzada Unidad Querétaro, Instituto Politécnico Nacional, Santiago de Querétaro, México. He has been a member of the Mexican National Researchers System (SNI) since 2007. He has authored over 30 publications in recognized technical journals and has participated in multiple technical meetings and workshops related to nuclear energy and applied plasma physics both in México and abroad.

Dr. Nieto-Pérez was a recipient of the 2010 Research Excellence at IPN Award, in the Young Researcher Category.



Gerardo López-Echevarría received the B.Sc. degree in food chemistry and the M.Sc. degree in food technology from the Universidad Autónoma de Querétaro, Santiago de Querétaro, México, in 1994 and 2004, respectively. He is currently pursuing the Ph.D. degree in advance technology with the CICATA-IPN Querétaro, Instituto Politécnico Nacional, Santiago de Querétaro.

He is currently a Research Assistant with CICATA-IPN Querétaro, Instituto Politécnico Nacional. His current research interests include the study of the modification by nonconventional alternative methods in starch matrices, the characterization of fermentation systems, and functional properties of foods using myofibrillar protein.



Michelle Tirado-Guerrero received the B.Sc. degree in biotechnology engineering from the Universidad Politécnica de Puebla, Puebla, México, in 2013. She is currently pursuing the M.Sc. degree in advance technology with CICATA-IPN Querétaro, Instituto Politécnico Nacional, Santiago de Querétaro, México.

She is a Research Assistant with CICATA-IPN Querétaro, Instituto Politécnico Nacional. Her current research interests include waste water treatment, plasma surface modification, plasma coating for biological applications, and fluidization in plasma reactors.



Jorge Adalberto Huerta-Ruelas received the B.Sc. degree in theoretical physics, the M.Sc. degree in physics, and the Ph.D. degree in electrical engineering from the Universidad Autónoma de San Luis Potosí, San Luis Potosí, México.

He is a full-time Researcher and the Dean with CICATA-IPN Querétaro, Instituto Politécnico Nacional, Santiago de Querétaro, México, where he was the Director from 2010 to 2013. His current research interests include the development of optical measurement instruments; these include the instrumentation, opto-mechanical design, and programming; for research applications and industrial control processes.



Ma. Guadalupe del Carmen Méndez-Montealvo received the B.Sc. degree in food engineering from the Universidad Autónoma de San Luis Potosí, San Luis Potosí, México, and the M.Sc. and Ph.D. degrees in food science from the Universidad Autónoma de Querétaro, Santiago de Querétaro, México.

She is a Professor with CICATA-IPN Querétaro, Instituto Politécnico Nacional, Santiago de Querétaro. She was a Post-Doctoral Researcher with the University of Arkansas, Fayetteville, AR, USA. Her current research interests include starch structure and functionality and its effect on starch modification for food and other applications.



Gonzalo Velázquez received the B.Sc. degree in marine food engineering from the Instituto Tecnológico del Mar, Mazatlán, México, the M.Sc. degree in food engineering from the Universidad Autónoma de Durango, Durango, México, and the Ph.D. degree in food science from the Universidad Autónoma de Querétaro, Santiago de Querétaro, México.

He is a Research Professor with CICATA-IPN Querétaro, Instituto Politécnico Nacional, Santiago de Querétaro. His current research interests include food science and technology, high pressure processing, alternative packaging materials, and the characterization of water interaction with hydrophilic materials.